Implementation of a hole spin qubit in Ge hut wires and dispersive spin sensing

by

Josip Kukučka

June, 2020

A thesis presented to the
Graduate School
of the
Institute of Science and Technology Austria, Klosterneuburg, Austria
in partial fulfillment of the requirements
for the degree of
Doctor of Philosophy



The thesis of [Josip Kukučka], titled *[Implementation of a hole spin qubit in Ge hut wires and dispersive spin sensing]*, is approved by:

Supervisor: Georgios Katsaros, IST Austria, Klosterneuburg, Austria

Signature: _____

Committee Member: Johannes Fink, IST Austria, Klosterneuburg, Austria

Signature: _____

Committee Member: Ferdinand Kuemmeth, Niels Bohr Institute, Copenhagen, Denmark

Signature: _____

Defense Chair: Gaia Novarino, IST Austria, Klosterneuburg, Austria

Signature: _____

signed page is on file

© by Josip Kukučka, June, 2020
All Rights Reserved

IST Austria Thesis, ISSN: 2663-337X

I hereby declare that this thesis is my own work and that it does not contain other people's work without this being so stated; this thesis does not contain my previous work without this being stated, and the bibliography contains all the literature that I used in writing the dissertation.
I declare that this is a true copy of my thesis, including any final revisions, as approved by my thesis committee, and that this thesis has not been submitted for a higher degree to any other university or institution.
I certify that any republication of materials presented in this thesis has been approved by the relevant publishers and co-authors.

Signature: _____

Josip Kukučka
June, 2020
signed page is on file

Abstract

Quantum computation enables the execution of algorithms that have exponential complexity. This might open the path towards the synthesis of new materials or medical drugs, optimization of transport or financial strategies etc., intractable on even the fastest classical computers. A quantum computer consists of interconnected two level quantum systems, called qubits, that satisfy DiVincezo's criteria. Worldwide, there are ongoing efforts to find the qubit architecture which will unite quantum error correction compatible single and two qubit fidelities, long distance qubit to qubit coupling and scalability. Superconducting qubits have gone the furthest in this race, demonstrating an algorithm running on 53 coupled qubits, but still the fidelities are not even close to those required for realizing a single logical qubit. Semiconductor qubits offer extremely good characteristics, but they are currently investigated across different platforms. Uniting those good characteristics into a single platform might be a big step towards the quantum computer realization.

Here we describe the implementation of a hole spin qubit hosted in a Ge hut wire double quantum dot. The high and tunable spin-orbit coupling together with a heavy hole state character is expected to allow fast spin manipulation and long coherence times. Furthermore large lever arms, for hut wire devices, should allow good coupling to superconducting resonators enabling efficient long distance spin to spin coupling and a sensitive gate reflectometry spin readout. The developed cryogenic setup (printed circuit board sample holders, filtering, high-frequency wiring) enabled us to perform low temperature spin dynamics experiments. Indeed, we measured the fastest single spin qubit Rabi frequencies reported so far, reaching 140 MHz, while the dephasing

times of 130 ns oppose the long decoherence predictions. In order to further investigate this, a double quantum dot gate was connected directly to a lumped element resonator which enabled gate reflectometry readout. The vanishing inter-dot transition signal, for increasing external magnetic field, revealed the spin nature of the measured quantity.

Acknowledgments

My PhD journey involved three different institutions. Firstly, I had eight months warm up at the Institute of Semiconductor and Solid State Physics at JKU Linz, then a three months research visit to the Qdev lab at the Niels Bohr Institute in Copenhagen and finally four years at the main institution, IST Austria. The person without whom this journey would not be possible is my supervisor and a friend Giorgos Katsaros. Thanks for a great support and guidance, patience, positive attitude and being a great group leader. I admire his ability to be deeply involved in so many different projects in parallel. He is also a source of a good atmosphere and friendliness in the group. A lot of students would be very happy to have such a supervisor, so I had a big privilege. Btw, if you ever have a chance to visit one of his Greek dinner events, do not miss it. The amount of food is always just perfect :) . In Linz, I also had a great help of Raimund Kirchschlager with the initial printed circuit board designs. Sussane Schwind, thanks for helping out with a lot of documentation and your efforts to teach us some German. Thanks to Elli and Alisha, for being good colleges and contributing to the nice atmosphere in the group. Thanks to Hannes and Carina for the game nights during which they turned their living room into a high level cocktail bar and also for teaching me how to make some cocktails.

The research visit to the Qdev lab in Copenhagen was very important in many ways. I have directly learned about spin qubit experiments, from Filip and Frederico, was exposed to information rich meetings of the ”Spin qubit” team, got a hands-on experience on a lab setup including the dilution fridge wiring and the experimental instrumentation. This proved to be especially beneficial, since, later on at IST, we needed to setup the

lab from scratch. Thanks to Ferdinand Kuemmeth as the Spin Qubit team leader and Charles Marcus, the head of the lab, who agreed on my visit there. Btw, thanks to Ferdinand for being my thesis committee member. Thanks to Christian as well, for his friendliness and help with the ALD machine. Maria Batista, thanks for finding me a shelter there. I cannot finish this not to mention Deividas Sabonis, a PhD student from the ”Majorana” team in Qdev lab, who I got along really well. Apart from the mentioned ones, there were many other people I interacted with at Qdev and hereby I want to say thanks to them for their warmth, helpful tips and useful advices.

During the starting months, after we switched to IST, Giorgos and me were the only members of the Nanoelectronics group here. Students of my cohort and some of their friends like Michelle Cloos, accepted me very nicely, even if I did not participate in the IST graduate school coursework with them. They helped to turn the IST into family environment for me.

Slowly our group was expanding and nowadays we typically count more then ten people. Lada, Hannes, Daniel, Jason, Marco, Kushagra, Matthias, Andrea, Luka, Max, Marin, Josh, Marian, Alessandro, Robin, Chaitrali, Sandesh, Praveen, Konrad, Alberto, Frederico, Stavroula, Oliver and Jaime. Some of them left, some are still here and the later ones just arrived. Naturally, with some I spend more and with others less time, but I am really glad that I had the opportunity to meet all of you! Hej Lado, by begin my office neighbour throughout all the time at IST, you were literally my closest person. Here I would also like to mention Konrad, Lada’s boyfriend. Even if I do not see him often, whenever I meet him it feels like we are friends for a long time. Hannes, thanks for making such a nice double quantum dot device, which yielded the most important part of this thesis. Daniel, thanks for sharing DAZN and SKY accounts with me. Marco you should come to play football more often, look at Marian :) . Matthias, I believe that your creatively critical style, made my presentations a bit better. Andrea, it is nice to see you being always positive, hope you will keep it. Daniel and Luka add a particular element of humor in the group, each in his own way, I would say. Nice to have you.

Apart from my group, I would like to devote a few lines for our experimental physics comrades, from the Lab West second floor. In the first place this is the group of Johannes Fink. Later on, also the group of Andrew Higginbotham. Thanks for work-related and non-work-related moments, sharing ideas in common group meetings, having common events and for being coffee and beer friends. Thanks to Johaness Fink for being my IST internal committee member.

It would be hard to imagine the time spent at IST without my friend Alfredo Rueda. Back then in 2016, when he came to IST (for the first time, hehehe), from the first weeks we somehow matched really well. He had, and still has, this ”let's go” attitude which gave me an activation I needed.

Shabir and Ensi, thank you for your company in hikes, dinners, coffees and generally for having a nice time.

Our work here would not be possible without the IST scientific support teams. Thomas, Peter, Thomas, Daniel, Abdul and Todor, thank you for supporting us with your electronic and mechanical knowledge and amazing skills. We are very privileged to have you here. Additional greetings to Peter and Thomas A. Peter, I will remember your semester opening parties :) . Equally important are our Nanofabrication Facility friends. Salvo, Juan, Lubuna, Philipp, Ivan and Arkadiusz thanks for running the cleanroom and being friendly. Greetings to super positive guy Ivan!

Furthermore, I would like to thank our A2Ps Maria, Stephanie and Sandra for their not only administrative help, both in professional and private terms, but for being always friendly.

Thanks to everybody whose contribution in Think&Drink talks, BBQs and similar events (also retreats), then activities like different sport sections, dance classes, movie nights and so on, helped in making IST a lively place, for a remote destination.

Hereby, I would also like to greet the IST football crew. I was a part of it since I joined IST. When the things were not working in the lab, often the thought of playing football

today would cheer me up. Thanks for the exciting time.

The spin dynamics experiments started to work after incorporating some inputs we got from Romain Maurand, Edward Laird, Menno Veldhorst and Arne Laucht. So thanks to you as well.

During my time spent here I also needed to live somewhere. Greater portion of that time I was not alone. My first flatmate was Peter then Mia and Luka, then for a short time Lenka, Georg, Sasha and Kristóf and finally Lukasz. Thank you all for sharing your living space with me!

I guess, like many other people, I could write a complete thesis about the role of my parents. People around me are changing but they are constant, with their support. And this support was crucial when it was the hardest. Greetings to my brothers and the sister!

About the Author

I finished the bachelor and master program, in electrical engineering and information technology, at the Faculty of Electrical Engineering and Computing, in Zagreb. After that, I joined the group of my supervisor at the Institute of Semiconductor and Solid State Physics, at the Johannes Kepler University, in Linz. After eight months in Linz, I spent three months at the Center for Quantum Devices, at the Niels Bohr Institute in Copenhagen, where I learned mainly about the low temperature instrumentation and spin qubit experiments. Subsequently, our group moved to the Institute of Science and Technology Austria, in Klosterneuburg, where I got enrolled in the second phase of my PhD. Here we set up the new laboratory for the low temperature transport experiments. My work was particularly focused on developing the setup for sensing the state of a hole spin qubit, confined in Ge hut wires, with the radio frequency reflectometry technique.

List of Publications

1. Heavy-Hole States in Germanium Hut Wires
   Hannes Watzinger, Christoph Kloeffel, Lada Vukušić, Marta D. Rossell, Violetta Sessi, Josip Kukučka, Raimund Kirchschlager, Elisabeth Lausecker, Alisha Truhlar, Martin Glaser, Armando Rastelli, Andreas Fuhrer, Daniel Loss, Georgios Katsaros
   Nano Letters **16**,6879-6885 (2016)

2. Fast Hole Tunneling Times in Germanium Hut Wires Probed by Single-Shot Reflectometry
   Lada Vukušić, Josip Kukučka, Hannes Watzinger and Georgios Katsaros
   Nano Letters **17**,5706-5710 (2017)

3. Single-shot readout of hole spins in Ge
   Lada Vukušić, Josip Kukučka, Hannes Watzinger, Joshua M. Milem, Friedrich Schäffler and Georgios Katsaros
   Nano Letters **18**,5706-5710 (2018)

4. A germanium hole spin qubit
   Hannes Watzinger, Josip Kukučka, Lada Vukušić, Fei Gao, Ting Wang, Friedrich Schäffler, Jian-Jun Zhang and Georgios Katsaros
   Nature Communications **9**,3902 (2018)

5. Site-Controlled Uniform Ge/Si Hut Wires with Electrically Tunable Spin–Orbit Coupling
   Fei Gao, Jian-Huan Wang, Hannes Watzinger, Hao Hu, Marko J. Rančić, Jie-

Yin Zhang, Ting Wang, Yuan Yao, Gui-Lei Wang, Josip Kukučka, Lada Vukušić, Christoph Kloeffel, Daniel Loss, Feng Liu, Georgios Katsaros, Jian-Jun Zhang
Advanced Materials 1906523 (2020)

Table of Contents

Abstract **vi**

Acknowledgments **viii**

About the Author **xii**

List of Publications **xiii**

List of Tables **xvii**

List of Figures **xviii**

List of Abbreviations **xxi**

1 Introduction **1**

2 Theory **6**

2.1 Bloch sphere representation 7

2.2 Rotating frame approximation 8

2.3 Spin dynamics 11

2.4 Single quantum dot 15

2.5 Double quantum dot 19

2.6 Loss-DiVincenzo qubit in a DQD 26

3 Material and fabrication **40**

3.1 Growth 41

3.2 Band structure 42
3.3 Hut wires and double quantum dots 43

4 Setup **52**
4.1 Dilution refrigerator 57
4.2 Reflectometry 63
4.3 Printed circuit boards 71

5 Qubit **88**
5.1 The qubit setup 89
5.2 The qubit hosting DQD stability diagram 91
5.3 Spin manipulation experiments 92

6 Gate based charge and spin sensing **102**
6.1 Gate reflectometry working principle 105
6.2 Experimental results 110

7 Conclusions **121**

Bibliography **125**

A Appendix 1 **137**
A.1 PCB elements 137
A.2 Python code 147

List of Tables

3.1 Parameters of samples, measurements of which are reported in this thesis 51

A.1 Values of PCB components mounted on PCBs discussed in this thesis . 146

List of Figures

2.1 Ilustration of the Bloch sphere 8
2.2 Illustration of the spin state rotation around the x-axis, in the RWA approximation 13
2.3 Sketch of a contacted single quantum dot 15
2.4 QD electrochemical potential ladder and Coulomb peaks 17
2.5 Zeeman splitting of hole spin states and temperature broadening of μ_S and μ_D 18
2.6 Sketch of a double quantum dot 19
2.7 Schematic of the double quantum dot electrochemical potentials 21
2.8 Sketch of the charge stability diagram of a hole DQD 22
2.9 DQD energy levels relevant for the experiments performed in this thesis 25
2.10 Rabi experiment schematic 28
2.11 Ilustration of ideal Rabi oscilation traces 30
2.12 Two-axis spin rotation 32
2.13 Plot showing the probability of the state at the time point t_4 being up ($P\,|\uparrow\rangle$) versus ϕ_p of the second burst, simulated in Python (QuTiP) . . . 33
2.14 Illustration of the Ramsey experiment 37
2.15 Ramsey experiment with dephasing. 38
2.16 Ilustration of Rabi oscilation traces with a power law decay 39

3.1 HW growth 42
3.2 Illustration of the valence band alignment and a DQD in a Ge HW 44
3.3 SEM images illustrating the Ge HW DQD fabrication steps 46

3.4 Illustration of the HW cross section after different fabrication steps . . . 47
3.5 SEM images of etched Ge HW DQD samples 48
3.6 Tunable DQD tunnel coupling on the ”MJ_5_S33” sample 49

4.1 Image of the full setup used in the majority of the experiments described in this thesis 54
4.2 Schematic of the full setup used in the majority of the experiments described in this thesis 55
4.3 Image showing the interior of the fridge with the probe inserted 57
4.4 The probe with the attenuator configuration 60
4.5 Low-pass filter configuration 62
4.6 Schematic of the reflectometry in the probe 64
4.7 Amplitude of the reflection coefficient and its change versus the impedance 65
4.8 Schematic of the exemplary amplifier chain 65
4.9 DC PCB named ”Shrek” 73
4.10 HF PCB named ”Iron Man”, PCB number 2 78
4.11 Iron Man PCB layout and layer stackup 79
4.12 HF PCB named ”Iron Kid”, PCB number 2 83
4.13 Iron Kid PCB layout and layer stackup 84
4.14 Comparison of the fast gate transmission and the crosstalk between Iron Man and Iron Kid 86
4.15 Room temperature measurement of the reflectometry reflection coefficient S_{11} on Iron Kid, number 5 and Iron Man, number 2 87

5.1 Setup for the qubit experiment 90
5.2 The stability diagram of a qubit hosting DQD 92
5.3 Continuous EDSR spin spectroscopy 94
5.4 Pulsed EDSR spin spectroscopy 95
5.5 Coherent spin oscillations around a single axis 96
5.6 Two-axis qubit manipulation 98

5.7 Ramsey experiment 100

6.1 Adapted schematic of a DQD with the reflectometry circuit connected to G1 105
6.2 SEM image and gate reflectometry data from the sample ”S228_111” . . 113
6.3 Magnetic field dependence of the inter-dot phase response 114
6.4 Gate reflectometry data from the sample ”MJ_5_S33” 118

A.1 Optical microscope image of a square coil 139
A.2 RC filter schematic 141
A.3 Simulation of the single (blue) and the double stage (orange) RC filters . 142
A.4 Plot showing the measured normalized amplitude versus the frequency response of the single stage RC filter 142
A.5 Bias tee schematic 144
A.6 Confirmation of the proper bias tee functionality 145

List of Abbreviations

ALD Atomic layer deposition

AWG Arbitrary waveform generator

CB Coulomb blockade

CP Coulomb peak

D Drain

DAC Digital to analog converter

DC Direct current

DQD Double quantum dot

EDSR Electric dipole spin resonance

FWHM Full width at half maximum

G Gate

HF High frequency

HFA Hydrofluoric acid

HW Hut wire

LF Low frequency

LT Low temperature

MC Mixing chamber

MW Microwave

PCB Printed circuit board

PM Pulse modulation

PSB Pauli spin blockade

QD Quantum dot

RF Radio frequency

RT Room temperature

RWA Rotating wave approximation

S Source

SEM Scanning electron microscope

SMD Surface mounted device

SMP Sub-miniature push-on

SNR Signal to noise ratio

UHFLI Ultra high-frequency lock in amplifier

VSG Vector signal generator

1 Introduction

There is a class of important problems, the best known algorithms running on currently fastest classical computers are not able to solve within a reasonable time frame, because of their exponential complexity. Examples of those problems are synthesis of medical drugs or purpose oriented new materials, optimization of large transport grids or financial strategies, machine learning enabled diagnostics and prediction methods etc. Meanwhile, Moore's law described speed increase and cost reducing miniaturization of field effect transistors, the classical processors are made of, is expected to hit the wall soon. Technical difficulties appearing for a few nm wide transistor channels are hard to overcome. On the other hand, electron transport through structures with sizes comparable to the electron wavefunction, has enabled the observation of quantum effects. Cooling down to temperatures near the absolute zero, allowed the localization, observation and manipulation of isolated quantum states. A very interesting property of such a system, from the information point of view, is the quantum superposition. The quantum superposition tells that a quantum system, having two possible states, can occupy these two states simultaneously. In other words, it is said to be in a superposition of the two basis states. Assembling many of such two level quantum systems, in an interconnected grid, would constitute a quantum computer, with its basic two level unit called a qubit. Similar to a bit in a classical computer, the basis state of a qubit can be represented as binary 0 or 1. So, how does the quantum computer solve the above mentioned problems faster than the classical one? If one freezes the computation happening on a classical 64-bit processor and observes the binary code on its

bus, this code would be one out of 2^{64} possible combinations of 64 binary digits. In fact, this would also happen in the case of 64 coupled qubits. An observation would return just one realization out of the 2^{64} possibilities. However, a crucial advantage of a quantum computer is that, before that observation, the performed calculation can use all of 2^{64} combinations in parallel, while on the classical one, no matter if we observe it or not, it is always in one out of 2^{64} possible combinations. To get a better feeling of the quantum property that provides the mentioned speedup, let's consider the following example. Say we have two dogs and they have to stay within the courtyard because they might attack our neighbor's cat otherwise. One day, at work, we completely forget if the courtyard door have been left open or not. While running home, for us, both outcomes, dogs out or dogs in, have the same probability and we might think that the dogs are in some kind of superposition. But, the dogs are physically in one of these two states all the time. It is our not knowing which makes this two outcomes equally possible. If the dogs, on the other hand, would behave as quantum objects, they would physically not exist in any of this states but in their superposition, until we come and eventually determine whether we let the dogs out or not. In that very moment they would stop to exist in the superposition and appear just inside the courtyard or, unfortunately, outside. Such an intrinsic property of a quantum system, i.e. quantum superposition, facilitates an exponential increase of the computational power and the information storage space with the number of qubits in the quantum computer. This enabled Shor [Shor, 1994] to come up with the algorithm for calculating prime factors of an integer number in a polynomial time, a problem which is considered intractable for large integers on a classical computer.

Those ideas and concepts sound very promising, but, how can one create a quantum computer, as a matter of fact, how can one even create a single qubit? A qubit can be created by encoding information into any two level quantum system that satisfies the DiVincenzo's qubit criteria [DiVincenzo, 2000]. Those criteria include the necessity for a scalable physical system with well characterized qubits, the possibility for qubit initialization, an universal set of the qubit gates (including single and two qubit gates),

long coherence times in respect to the qubit gate time, and qubit-specific measurement capability.

In the above discussion, the quantum computer is assumed to be assembled out of logical qubits which behave perfectly, meaning that they are completely error free. In reality qubits are very prone to wrong initialization, wrong readout and faulty manipulation (faulty gates). For example, a wrong readout could occur if the integration time, for achieving a good signal to noise ratio (SNR), is on the order of the relaxation time. The faulty manipulation can happen because of a short coherence time in comparison to the manipulation time. All the three, initialization, manipulation and readout are characterized by the corresponding fidelities, which are measured as the ratio of correct outcomes divided with the total number of attempts. In case the physical qubits have fidelity higher than the threshold value of 99$\%$, by performing the quantum error correction protocol, on a number of them, the logical qubit can be recovered [Fowler *et al.*, 2012]. The better the physical qubit fidelity, the lower the number of required physical qubits for the realization of a single logical qubit (~ 3600 for a 99.9$\%$ fidelity).

In order to satisfy the above criteria people have tried to implement qubits in two level quantum systems such as the polarization state of a photon [O'Brien *et al.*, 2009], two an-harmonic levels in a superconducting circuit [Barends *et al.*, 2014], hyperfine states of trapped ions [Brown *et al.*, 2011], nuclear spins in a diamond [Waldherr *et al.*, 2014] and charge and spin states in semiconductor quantum dots (QDs) [Hayashi *et al.*, 2003; Loss and DiVincenzo, 1998; Kane, 1998]. Superconducting qubits went the furthest in demonstrating a quantum algorithm execution [Arute *et al.*, 2019], but a single logical qubit is still a hurdle set very high, for any platform. On the other hand, similar manipulation fidelities [Yoneda *et al.*, 2017], much longer relaxation times [Muhonen *et al.*, 2014], very sensitive and fast readout [Schaal *et al.*, 2020; Zheng *et al.*, 2019; Keith *et al.*, 2019] were observed in different realizations of spin qubits confined in solid-state semiconductors QDs. Additionally, the small footprint and the possiblity of using already highly developed semiconductor nanofabrication techniques, renders the spin

qubits as promising candidates for addressing the fundamental scalability requirement. But, the exact semiconductor platform that will unite all these good characteristics is yet to be found, especially in terms of high fidelity two qubit gates [Nowack *et al.*, 2011] and long distance spin to spin coupling [Borjans *et al.*, 2020] which seems to be the main obstacle.

First experimental realizations of semiconductor spin qubits were demonstrated in double quantum dots (DQD) created by electrostatic depletion of an electron gas below the electron beam patterned gate electrodes in GaAs heterostructures [Petta *et al.*, 2005; Koppens *et al.*, 2006]. Despite a very large boost of the coherence time by the nuclear spin polarization techniques [Bluhm *et al.*, 2010] and nuclear notch filtering methods [Malinowski *et al.*, 2017], the nuclear noise induced decoherence pushed a large part of the community towards electron spins in Si. Si naturally comes with a lower amount of isotopes carrying a non-zero nuclear spin and it can be additionally purified. As a result, extremely long coherence times [Muhonen *et al.*, 2014] and high qubit manipulation fidelities [Muhonen *et al.*, 2014; Yoneda *et al.*, 2017] were measured. Also, two qubit gates, based on the short range exchange coupling were shown [Veldhorst *et al.*, 2015; Zajac *et al.*, 2018; Watson *et al.*, 2018]. Furthermore, great results on a distant spin to spin interaction ($> 4\,mm$) [Borjans *et al.*, 2020] suggest that long distance qubit gates are within reach for electron spins in Si, dressed with an artificial spin orbit coupling. Using the intrinsic spin orbit coupling of holes, on the other hand, avoids the necessity for additional micro-magnets for the artificial spin-orbit coupling generation, simplifying thus the qubit device fabrication. Such enabled fast and fully electrical spin manipulation of a hole spin qubit in Si [Maurand *et al.*, 2016], but the dephasing time $T_2^* \approx 60\,ns$ was short as well. Ge, on the other hand, offers even stronger and tunable spin orbit coupling [Hao *et al.*, 2010; Kloeffel *et al.*, 2017], while still offering a reduced amount of spin carying nuclei and allows isotopical purification, as well. A preserved CMOS foundry compatibilty combined with an easier confinement caused by lower effective masses, give an additional vote to Ge as a scalability friendly material. Initial studies performed on holes in Ge/Si core/shell nanowires [Lu *et al.*, 2005;

Brauns *et al.*, 2016] revealed relatively long relaxation time of $T_1 = 0.6\,ms$ [Hu *et al.*, 2012] and the dephasing times of $T_2^* = 180\,ns$ [Higginbotham *et al.*, 2014]. Furthermore, the experiments on gate defined DQDs in two dimensional hole gasses hosted in a Ge/SiGe heterostructure, uncovered the great potential of holes in Ge by demonstrating a two qubit gate executed in 75 ns and a single qubit fidelity of 99.3$\%$ [Hendrickx *et al.*, 2020].

The qubit described in this thesis is based on hole spins confined in DQDs hosted in Ge hut wires (HWs) [Zhang *et al.*, 2012; Watzinger *et al.*, 2014]. HWs are created by means of strain relaxation, built up in Ge monolayers, epitaxialy grown on Si. They are fully strained and have a triangular cross section with a base width of 20 nm and a height of 2 nm. The strong confinement and strain lifts light hole-heavy hole degeneracy with the heavy hole being the ground state [Watzinger *et al.*, 2016] of the system. Such should allow long spin dephasing times [Fischer *et al.*, 2008] and together with a strong and tunable spin-orbit coupling [Gao *et al.*, 2020] should result in large coherence to manipulation time ratios. Indeed, the experiments revealed the fastest (to date) Rabi frequencies for a single spin qubit, reaching 140 MHz [Watzinger *et al.*, 2018]. But, the Ramsey experiment revealed a lower than expected dephasing time of 130 ns, similar (within an order of magnitude) to other hole spin dehasing times reported so far [Higginbotham *et al.*, 2014; Maurand *et al.*, 2016; Hutin *et al.*, 2018; Hendrickx *et al.*, 2020] and the dephasing of an electron spin in a natural Si [Pla *et al.*, 2012]. First step towards an examination of the dephasing time deteriorating noise sources is a fast readout. Here comes another advantage of HW devices, namely a high gate to dot coupling factor, which is expected to increase the readout sensitivity of the gate reflectometry readout technique.

2 Theory

2.1 Bloch sphere representation

A description of the basic principles needed to understand the spin qubit experiments, described in this thesis, is given below:

A state $|\Psi\rangle$ of a two level quantum system can be represented as a superposition $|\Psi\rangle = \alpha\,|0\rangle + \beta\,|1\rangle$ of its basis state vectors $|0\rangle$ and $|1\rangle$, where α and β are complex numbers. The total probability of a quantum system, to be in one of the states, is 1, meaning $|\alpha|^2 + |\beta|^2 = 1$. Regarding the phase of these two complex numbers, only the relative phase between them has a physical meaning. These two facts, about the total probability and the phase, allow the state representation as a vector $|\Psi\rangle = cos\frac{\Theta}{2}\,|0\rangle + sin\frac{\Theta}{2}e^{i\phi}\,|1\rangle$, with only two variables Θ and ϕ, at the so called Bloch sphere, where $0 \leq \Theta \leq \pi$ and $0 \leq \phi \leq 2\pi$.

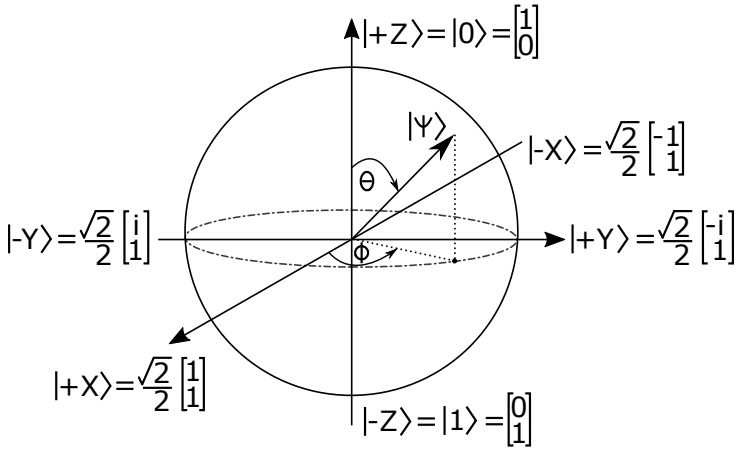


Figure 2.1: **Illustration of the Bloch sphere.** The quantum state $|\Psi\rangle$ is represented by a unit vector, going from the center to the surface of the sphere. Its direction is determined by the angles Θ and ϕ which carry the information about the quantum state. Six characteristic states are shown, with $|0\rangle$ and $|1\rangle$ being the basis states.

2.2 Rotating frame approximation

Let's suppose that the the two level quantum system is a spin-1/2 particle. Since the spin is a magnetic dipole, after application of the magnetic field B, the Hamiltonian of such a system looks like [Levitt, 2001]:

$$H = -\vec{\mu}\vec{B} \tag{2.1}$$

with $\vec{\mu}$ being the spin magnetic moment $\vec{\mu} = \frac{eg}{2m}\vec{S}$. Here, e is the elementary charge, m the particle mass, g is the g-factor along the magnetic field direction and $\vec{S} = \frac{\hbar}{2}\vec{\sigma}$ is the spin vector. Furthermore $\hbar$ is the reduced Planck constant and $\vec{\sigma}$ stands for the Pauli matrices σ_x, σ_y and σ_z.

$$\sigma_X = \begin{bmatrix} 0 & 1 \\ 1 & 0 \end{bmatrix}, \sigma_Y = \begin{bmatrix} 0 & -i \\ i & 0 \end{bmatrix}, \sigma_Z = \begin{bmatrix} 1 & 0 \\ 0 & -1 \end{bmatrix} \tag{2.2}$$

The Hamiltonian can be then written as:

$$H = \frac{1}{2} g \mu_B \vec{\sigma} \vec{B} \tag{2.3}$$

where $\mu_B = \frac{e\hbar}{2m}$ is the Bohr magneton.

Solving the Schrödinger equation:

$$i\hbar \frac{d}{dt} |\Psi(t)\rangle = H |\Psi(t)\rangle \tag{2.4}$$

and assuming a magnetic field along the z direction $\vec{B} = B_z \vec{z}$ one can see that the system has energies:

$$E_{\pm} = \pm \frac{1}{2} g \mu_B B_z \tag{2.5}$$

and evolves in time according to:

$$|\Psi(t)\rangle = e^{-i\frac{H}{\hbar}t} |\Psi(0)\rangle = e^{-i\frac{\omega_z}{2}\sigma_z t} |\Psi(0)\rangle \tag{2.6}$$

where $\omega_z = \frac{g\mu_B B_z}{\hbar}$ stands for the Larmor frequency.

The term $e^{-i\frac{\omega_z}{2}\sigma_z t}$ introduces a relative phase evolution $\phi = \frac{\omega_z}{2} t$ between the spin up $|\uparrow\rangle = |0\rangle$ and the spin down $|\downarrow\rangle = |1\rangle$ components in the state $|\Psi\rangle$, corresponding to the $|\Psi\rangle$ rotation around the z-axis in Figure 2.1, with frequency ω_z.

The Equation 2.6 can be written in the following form:

$$|\Psi(t)\rangle = R_z(\frac{\omega_z}{2} t) |\Psi(0)\rangle \tag{2.7}$$

where $R_z = e^{-i\frac{\omega_z}{2}\sigma_z t}$ is the rotation operator around the z-axis.

In general, the rotation operator around a single axis is $R(b) = e^{-i\frac{b}{2}\sigma}$. Since σ is a Pauli matrix σ_x, σ_y or σ_z, the following applies:

$$R(b) = e^{-i\frac{b}{2}\sigma} = I cos(\frac{b}{2}) - i\sigma sin(\frac{b}{2}) \tag{2.8}$$

and therefore:

$$R_x(b) = \begin{bmatrix} cos(\frac{b}{2}) & -isin(\frac{b}{2}) \\ -isin(\frac{b}{2}) & cos(\frac{b}{2}) \end{bmatrix} \tag{2.9}$$

$$R_y(b) = \begin{bmatrix} cos(\frac{b}{2}) & -sin(\frac{b}{2}) \\ sin(\frac{b}{2}) & cos(\frac{b}{2}) \end{bmatrix} \tag{2.10}$$

$$R_z(b) = \begin{bmatrix} cos(\frac{b}{2}) - isin(\frac{b}{2}) & 0 \\ 0 & isin(\frac{b}{2}) - cos(\frac{b}{2}) \end{bmatrix} \tag{2.11}$$

Following the techniques from the nuclear magnetic resonance, the spin state can be rotated from $|1\rangle$ to $|0\rangle$ by applying an oscillatory magnetic field, in a perpendicular direction to the static one and with a frequency equal to the Larmor frequency. For understanding the state evolution, it is handy to work in the rotating frame. In the rotating frame the Bloch sphere rotates with the reference frequency ω_{REF} causing a spin, exposed to a static B_z field, to appear static in the case of $\omega_z = \omega_{REF}$:

$$|\Psi_{rot}(t)\rangle = |\Psi_{rot}(0)\rangle = |\Psi(0)\rangle \tag{2.12}$$

where $|\Psi_{rot}(t)\rangle$ is the spin state as seen from the rotating frame.

In general, we want to find the transformation:

$$|\Psi_{rot}(t)\rangle = R_z(-c)\,|\Psi(t)\rangle\,. \tag{2.13}$$

where $c = \frac{\omega_{REF}t}{2}$. Since $R_z(c)$ is a unitary operator, the following is valid:

$$|\Psi(t)\rangle = R_z(c)\,|\Psi_{rot}(t)\rangle\,. \tag{2.14}$$

Next, one needs to find the Hamiltonian in the rotating frame (H_{rot}). By substituting Equation 2.14 in the Schrödinger equation in the laboratory frame 2.4, one gets:

$$i\hbar\frac{d[R_z(c)\,|\Psi_{rot}(t)\rangle]}{dt} = HR_z(c)\,|\Psi_{rot}(t)\rangle \tag{2.15}$$

Now, by following the derivations from the book [Levitt, 2001]:

$$i\hbar\frac{d\left|\Psi_{rot}(t)\right\rangle}{dt} = \left[R_z(-c)HR_z(c) - \hbar\frac{\omega_{REF}}{2}\sigma_z\right]\left|\Psi_{rot}(t)\right\rangle. \tag{2.16}$$

Thus, H_{rot} can be expressed as a function of the already known H (Equation 2.3):

$$H_{rot} = R_Z(-c)HR_Z(c) - \hbar\frac{\omega_{REF}}{2}\sigma_z \tag{2.17}$$

2.3 Spin dynamics

To drive qubit rotations, from $|\downarrow\rangle$ to $|\uparrow\rangle$, a magnetic field burst (wave of a limited duration) should be applied along an axis orthogonal to the z-axis, with the burst frequency ω_{REF} equal to the Larmor frequency ω_z. Let's consider the case for a burst applied along the x-axis:

$$\vec{B}_x(t) = B_{burst}cos(\omega_{REF}t + \phi_p)\vec{x} \tag{2.18}$$

The burst amplitude B_{burst} is non zero only during the burst and ϕ_p is the initial phase of the burst.

Furthermore, $\vec{B}_x(t)$ can be decomposed to the resonant and the non-resonant term:

$$\vec{B}_x(t) = \vec{B}_x^{res}(t) + \vec{B}_x^{non-res}(t) \tag{2.19}$$

$$\vec{B}_x^{res}(t) = \frac{1}{2}B_{burst}[cos(\omega_{REF}t + \phi_p)\vec{x} + sin(\omega_{REF}t + \phi_p)\vec{y}] \tag{2.20}$$

$$\vec{B}_x^{non-res}(t) = \frac{1}{2}B_{burst}[cos(\omega_{REF}t + \phi_p)\vec{x} - sin(\omega_{REF}t + \phi_p)\vec{y}] \tag{2.21}$$

The $\vec{B}_x^{non-res}(t)$ term rotates in the opposite sense to the Larmor frequency and has almost no influence, therefore $\vec{B}_x(t) \approx \vec{B}_x^{res}(t)$.

Thus the total magnetic field looks like:

$$\vec{B} = B_z\vec{z} + \frac{1}{2}B_{burst}[cos(\omega_{REF}t + \phi_p)\vec{x} + sin(\omega_{REF}t + \phi_p)\vec{y}] \tag{2.22}$$

By substituting $\vec{B}$ in Equation 2.3, the total Hamiltonian in the laboratory frame looks like:

$$H = \frac{1}{2}g\mu_B[B_z\sigma_z + \frac{1}{2}B_{burst}[cos(\omega_{REF}t + \phi_p)\sigma_x + sin(\omega_{REF}t + \phi_p)\sigma_y]] \tag{2.23}$$

$$H = \frac{\hbar\omega_z\sigma_z}{2} + \frac{\hbar\omega_1}{2}[cos(\omega_{REF}t + \phi_p)\sigma_x + sin(\omega_{REF}t + \phi_p)\sigma_y] \tag{2.24}$$

where $\omega_z = \frac{g\mu_B B_z}{\hbar}$ and $\omega_1 = \frac{g\mu_B B_{burst}}{2\hbar}$.

Due to the approximation of the total magnetic field with the resonant one, the rotating frame is from now on called the rotating wave approximation (RWA). By substituting Equation 2.24 into Equation 2.17, the Hamiltonian in the RWA reads as:

$$H_{rot} = \frac{1}{2}\hbar(\omega_z - \omega_{REF})\sigma_z + \frac{\hbar\omega_1}{2}(cos\phi_p\sigma_x + sin\phi_p\sigma_y) \tag{2.25}$$

So, the magnetic field burst, with the burst frequency ω_{REF} equal to ω_z rotates the spin around an axis in the x-y plane defined by the burst phase ϕ_p. In case $\omega_{REF} \neq \omega_z$ a z-component in the rotation axis appears as well.

To give a concrete example, let's assume that the frequency of the burst matches the Larmor frequency $\omega_z = \omega_{REF}$, the phase $\phi_p = 0$, and the time of the burst is τ. Then the Hamiltonian in Equation 2.25, during the time τ, reduces to:

$$H_{rot} = \frac{\hbar\omega_1}{2}\sigma_x \tag{2.26}$$

and the state evolves as:

$$|\Psi_{rot}(t)\rangle = e^{-i\frac{\omega_1}{2}\sigma_x t}\,|\Psi_{rot}(0)\rangle = R_x(\omega_1 t)\,|\Psi_{rot}(0)\rangle \tag{2.27}$$

After the burst is finished ($t > \tau$) $B_{burst} = 0$ and consequently $H = 0$ meaning that the state is static for $t > \tau$.

For a burst duration adjusted such that $b = \omega_1\tau = \frac{\pi}{2}$, the rotation operator $R_x(b)$ reads as:

$$R_x(\frac{\pi}{2}) = \begin{bmatrix} \frac{\sqrt{2}}{2} & -i\frac{\sqrt{2}}{2} \\ -i\frac{\sqrt{2}}{2} & \frac{\sqrt{2}}{2} \end{bmatrix} \tag{2.28}$$

If the initial state is $|\Psi_{rot}(0)\rangle = |0\rangle = \begin{bmatrix} 1 \\ 0 \end{bmatrix}$, after the burst, the final state will be:

$$|\Psi_{rot}(t > \tau)\rangle = R_x(\frac{\pi}{2})\,|0\rangle = \begin{bmatrix} \frac{\sqrt{2}}{2} & -i\frac{\sqrt{2}}{2} \\ -i\frac{\sqrt{2}}{2} & \frac{\sqrt{2}}{2} \end{bmatrix} \begin{bmatrix} 1 \\ 0 \end{bmatrix} = \begin{bmatrix} \frac{\sqrt{2}}{2} \\ -i\frac{\sqrt{2}}{2} \end{bmatrix} = \frac{\sqrt{2}}{2} \begin{bmatrix} i \\ 1 \end{bmatrix} = |-Y\rangle \tag{2.29}$$

So, by applying the $R_x(\frac{\pi}{2})$ burst the state got rotated by an angle of $\Theta = \frac{\pi}{2}$ around the x-axis, as shown on Figure 2.2. In other words a $(\frac{\pi}{2})_x$ pulse was applied.

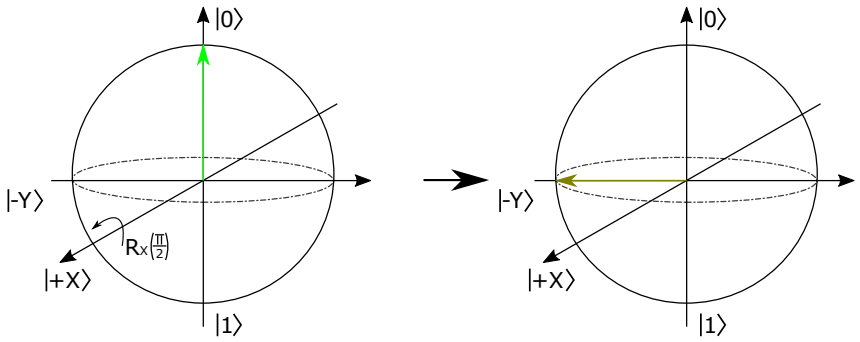


Figure 2.2: **Illustration of the spin state rotation around the x-axis, in the RWA approximation.** An applied $R_x(\frac{\pi}{2})$ rotation, rotates the initial spin state $|\Psi_{rot}(0)\rangle = |0\rangle$ to the final spin state $|\Psi_{rot}(\tau)\rangle = |-Y\rangle$, according to the right hand rule.

2.3.1 Electric dipole spin resonance (EDSR) driven spin rotation

The spin rotating oscillatory magnetic fields can be generated by oscillatory currents passing through a stripline next to a qubit device [Koppens *et al.*, 2006]. But, such fields are hard to restrict only to a space region of a spin confining QD, prohibiting thus the spin addressability in systems involving multiple QDs. An alternative solution is to use slanted magnetic fields, generated by a properly shaped micromagnet. A different static magnetic field, experienced by spins in adjacent QDs, allows the spin addressability in that case. Additionally, due to the micromagnet generated magnetic field gradient, the microwave (MW) electric field induced shaking of a spin carrying charge particle, translates into an oscillatory magnetic field which rotates the spin state from $|\downarrow\rangle$ to $|\uparrow\rangle$ when the frequency of the electric field f_{MW} matches the Larmor frequency [Pioro-Ladrière *et al.*, 2008]. In order to avoid the fabrication of micromagnets, the intrinsic spin orbit coupling can be exploited as a mechanism which couples the charge motion and the spin. An effective oscillatory magnetic field can be generated as a consequence of a charge wavefunction displacement in a system with sizeable spin orbit interaction. This field, in the presence of a static magnetic field can induce spin rotations via the so called EDSR mechanism. The amplitude of the effective magnetic field, which determines the rotation frequency ω_1 (Equation 2.25), is proportional to the spin orbit interaction strength and the wavefunction displacement. The displacement is further proportional to the amplitude of the oscillatory electric field, at the charge particle position. In particular, for holes in Ge wires, which is the system used for the experiments in this thesis, there are different types of spin orbit interaction mechanisms [Kloeffel *et al.*, 2017] which summed up determine the effective magnetic field value.

2.4 Single quantum dot

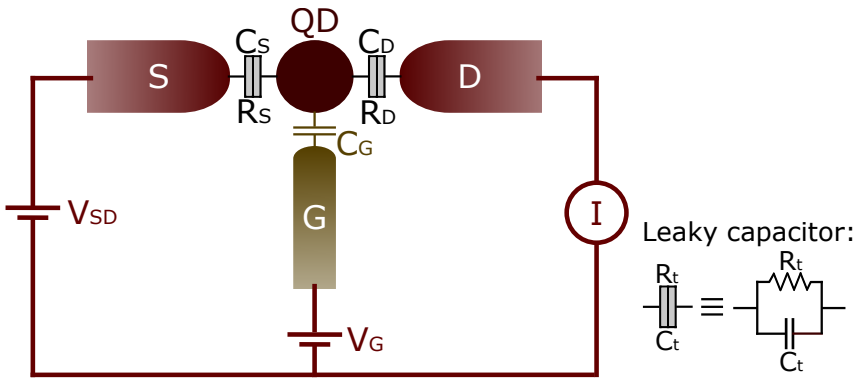


Figure 2.3: **Sketch of a contacted single quantum dot.** The QD is represented with the filled circle. The source (S) and drain (D) metal electrodes, called leads, are electrostatically and tunnel coupled to the QD via leaky capacitors. A leaky capacitor consists of the capacitance C_t and the tunneling resistance R_t. It is called "leaky" because a charge can tunnel through it. The width of the tunnel barrier defines the tunnel resistance as $R_t \sim \frac{1}{\Gamma_t}$, where Γ_t is the tunnel rate. The subscript t is exchanged with S and D for the source and the drain, respectively. The gate electrode (G) is only electrostatically coupled to the QD via the capacitance C_G. V_{SD} is the voltage applied between the source and the drain (because the amperometer (I) represents a short) and V_G sets the potential of the gate electrode in respect to S and D.

Because of the Coulomb interaction, particles with the same charge sign repel each other. Here we focus on positively charged holes. If a hole is trapped in a very small box, a relatively high energy, called charging energy E_C would be required to add another hole in the box, allowing thus control of the box's charge state. Such a box is called a QD. Furthermore, if the dimensions of that box approach the size of the hole wavelength, bound states are formed, causing orbital level quantization, with the level splitting ΔE. Such a QD could allow control and readout of the hole state with a carefully designed setup. For this, the QD is typically contacted with two tunnel and one capacitively coupled metal electrodes, as can be seen in Figure 2.3. Applying voltages to these electrodes shifts the respective electrochemical potentials. The electrochemical potential of a QD ($\mu(N)$) is the energy needed to add the N-th hole to it:

$\mu(N) = U(N) - U(N-1)$, where $U(N)$ is the total energy of a QD filled with N holes. Two different electrochemical potential configurations with a small V_{SD} applied between the source and the drain, can be seen in Figure 2.4. For a hole, it is energetically favourable to tunnel from a lower to a higher electrochemical potential. Therefore in Figure 2.4b, the QD is filled with N-1 holes and there is no current transport or in other words, the dot is in Coulomb blockade (CB). In Figure 2.4a, hole transport through the QD is allowed trough μ_N. The current transport can be measured by a sensitive amperometer. By sweeping the gate voltage, every time the electrochemical potential is inside the bias window $eV_{SD} = \mu_S - \mu_D$ there is a peak in the current, resulting in a series of Coulomb peaks (CPs) (consult Figure 2.4c). From here the addition energy can be extracted as $E_{add} = \mu(N+1) - \mu(N) = E_C + \Delta E$. Since the same orbital level can be occupied with two antiparalel spins, ΔE can be zero. So, filled orbitals result in zero total spin and therefore an oddly occupied dot, with many holes inside, can be approximated with a dot occupied just with one hole.

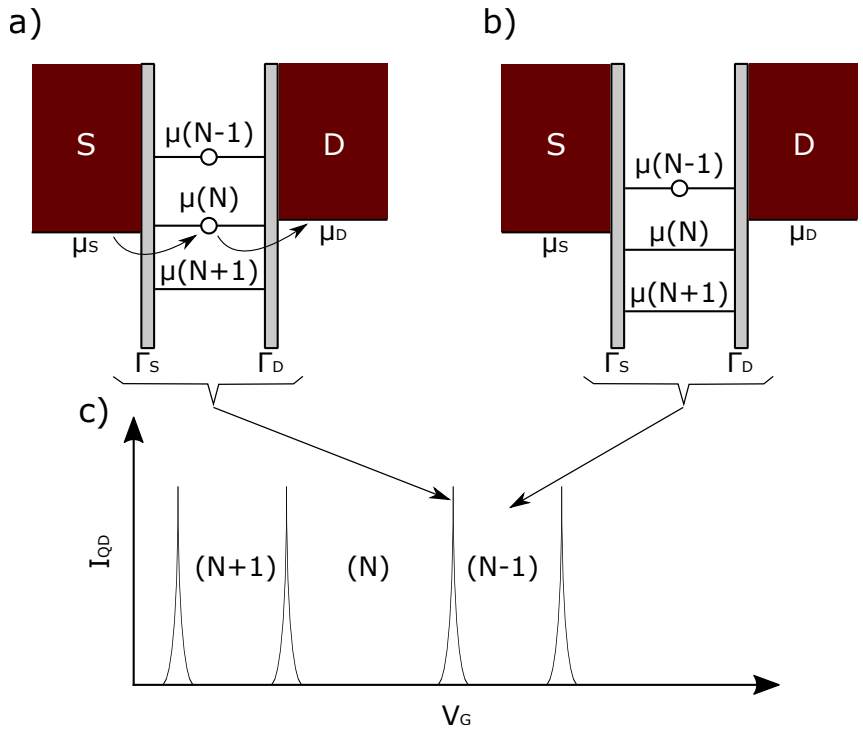


Figure 2.4: **QD electrochemical potential ladder and Coulomb peaks.** Zero temperature is assumed here, resulting in a sharp Fermi distribution. **a** When $\mu(S) < \mu(N) < \mu(D)$ current transport is allowed, which results in a current peak, the so-called Coulomb peak. **b** For more positive gate voltage and when $\mu(N) < \mu(S), \mu(D)$ the QD is in Coulomb blockade resulting in no current. Since $\mu(N-1)$, is above μ_S and μ_D, the dot is occupied with N-1 holes. **c** The gate-voltage sweep sequentially drives the dot electrochemical potentials through the bias window, resulting in a series of CPs. Going in a positive V_G direction, after each CP the number of holes localized in the QD reduces by one.

Now, let's assume that the dot is tuned to an odd occupation number of holes. Upon application of an external magnetic field, the spin degeneracy is lifted as can be seen in Figure 2.5. The spin states are then splitted by the Zeeman energy E_Z, introduced above.

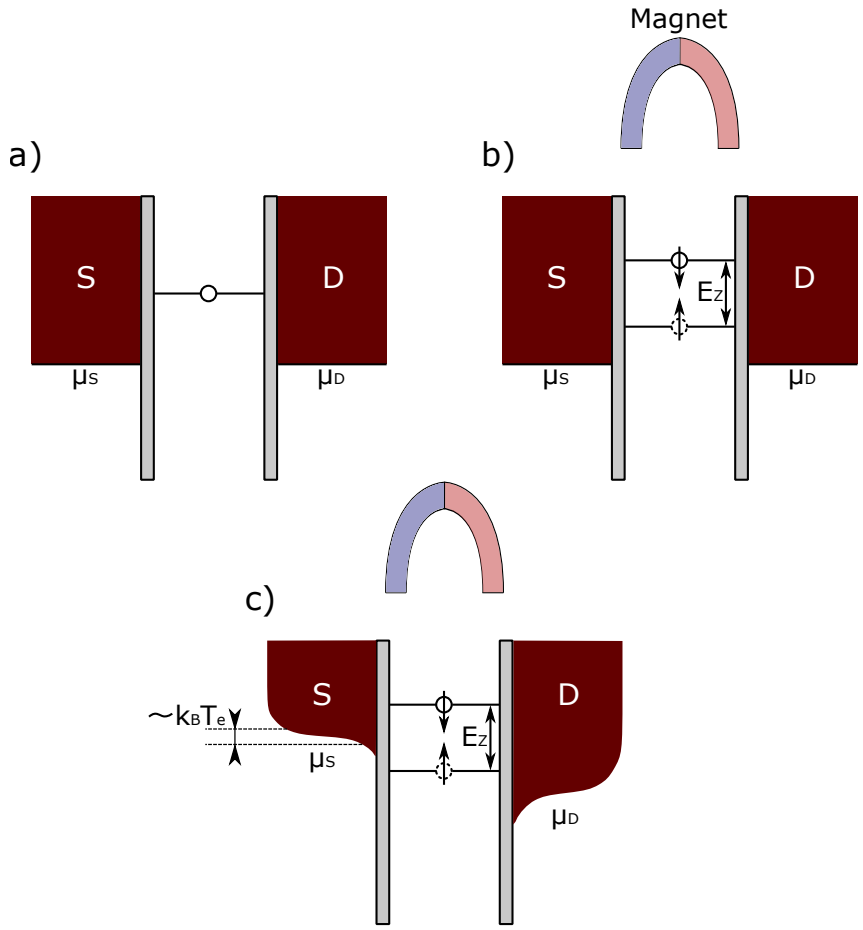


Figure 2.5: **Zeeman splitting of hole spin states and temperature broadening of μ_S and μ_D. a** Schematic showing a QD occupied by a single hole. **b** Upon application of an external static magnetic field, the hole spin levels split by E_Z. The spin down state is the ground state and therefore it is occupied, while the dashed circle of the spin up state marks it as non-occupied. In **a** and **b** $V_{SD} = 0$ and the electron temperature (T_e) is considered to be zero. **c** Same as in **b**, but a finite T_e broadens μ_S and μ_D, with a thermal broadening proportional to $k_B T_e$, where k_B is the Boltzmann constant. Also $V_{SD} \neq 0$.

The up $|\uparrow\rangle$ and down $|\downarrow\rangle$ spin states form a two level quantum mechanical system and all the considerations introduced above, for the spin-1/2 system, apply here. After satisfying the DiVincenzo criteria such a system can be operated as a spin qubit. For obtaining good fidelities for a single QD spin qubit [Loss and DiVincenzo, 1998], E_Z needs to be large in comparison to the thermal broadening of μ_S and μ_D (consult Figure 2.5c). This typically results in a very high qubit manipulation frequency $f_{MW} = f_{REF} =$

$f_z = E_z/h$ [Pla *et al.*, 2012]. If, on the other hand, one encodes the qubit in the spin states of one QD integrated in a serial DQD configuration, initialization and readout can be governed by the inter-dot tunneling instead of the lead to dot tunneling. Since the inter-dot transition does not suffer from the thermal broadening, the same fidelities can be achieved with a lower E_z, reducing thus f_{MW} to a range of well developed and affordable high frequency (HF) electronics.

2.5 Double quantum dot

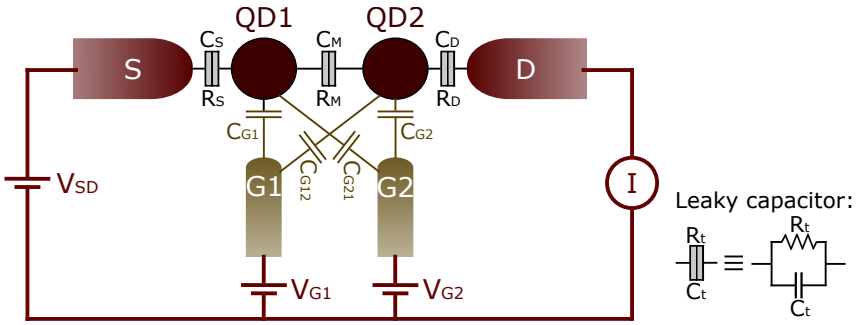


Figure 2.6: **Sketch of a double quantum dot.** A DQD consists of two single QDs, connected in series. The left QD is coupled to the source contact via the leaky capacitor characterized by C_S and R_S, while the drain couples to the right dot via the leaky capacitor characterized by C_D and R_D. The small distance between the two QDs makes them electrostatically and tunnel coupled, which is quantified by the mutual capacitance C_M and the tunnel resistance $R_M \sim \frac{1}{\Gamma_M}$. The gate electrode G1(2) is not only electrostatically coupled to QD1(2) through $C_{G1(2)}$, but also cross-coupled to QD2(1) via $C_{G12(21)}$. The reason of the cross-coupling is the small distance between gates G1 and G2 caused by the small distance between the QDs. Similarly as in the single QD case, the voltage between the source and the drain is set by V_{SD} while the voltage $V_{G1(2)}$ sets the potential of QD1(2) in respect to the S and D potential.

Figure 2.6 shows a schematic of a series DQD. Pretty much all DQD principles stated below are taken from the reviews of W.G. van der Wiel et al [van der Wiel *et al.*, 2002] and R. Hanson et al [Hanson *et al.*, 2007]. The electrochemical potential configuration can be seen in Figure 2.7. Here they are adjusted such that a small bias window fits

$\mu_1(N, M-1)$ and $\mu_2(N-1, M)$, allowing thus transport of holes between S and D. The amplitude of the transport current is set by the tunnel barriers characterized with tunnel rates $\Gamma_S, \Gamma_M, \Gamma_D$ and by the level alignment. In the case when μ_1 and μ_2 are aligned, the transport is elastic, resulting in a larger current. In the misaligned case the current transport can only happen involving energy exchange with the environment, resulting in a smaller current. In Figure 2.8a $C_{G12(21)}$,C_m and V_{SD} are assumed to be zero. If $C_m, C_{G12(21)} > 0$ (Figure 2.8b) then the lines get inclined and transport can happen at, so called, triple points at which μ_1 and μ_2 are aligned. Upon application of a bias V_{SD}, the triple points evolve into bias triangles, shown in Figure 2.8c. The triangle size depends on the applied V_{SD}. An example is given for the (1,1)-(0,2) DQD charge transition. Going from a lower to an upper point of the upper triangle baseline, $\mu_1(1,1)$ is aligned with $\mu_2(0,2)$ resulting in an elastic tunneling and therefore the pronounced current line. Along the right edge of the upper triangle, μ_1 stays aligned with the source potential. Going towards lower V_{G2} voltages initially reduces the current because of the DQD potentials misalignment, until the excited state $\mu_2^*(0,2)$ gets aligned with $\mu_1(1,1)$. Alignment of these two levels is preserved along the line parallel to the baseline, resulting in a higher current. Apart from the baseline and this parallel line, everywhere else in the triangle the current transport is enabled via inelastic tunneling. Since the hole can tunnel both through the ground and the excited state, of the right QD, the current is higher in the darker region. Similar explanation applies for the lower bias triangle as well, with a different charge configuration sequence during the transport of a single hole. For the upper triangle the sequence is (1,1)$\rightarrow$(0,2)$\rightarrow$(0,1)$\rightarrow$(1,1) while for the lower one it goes (1,2)$\rightarrow$(1,1)$\rightarrow$(0,2)$\rightarrow$(1,2). From such a stability diagram, involving tunneling via excited states, all relevant energy scales and couplings can be extracted. For example the G1(2) to QD1(2) coupling factor $\alpha_{1(2)}$ can be extracted as $\alpha_{1(2)} = \frac{|eV_{SD}|}{\delta V_{G1(2)}}$ [van der Wiel *et al.*, 2002].

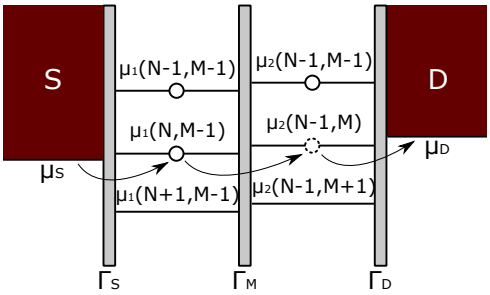


Figure 2.7: **Schematic of the double quantum dot electrochemical potentials.** Due to the mutual capacitance between the dots, the electrochemical potential configuration of one dot depends on the hole number in the other. The potentials μ_1 in QD1 are shown for M-1 hole in QD2, while for the shown potentials in QD2 (μ_2), N-1 holes are assumed in QD1. The potentials in each dot can be shifted up and down in energy by the respective gate electrode voltages, shown in Figure 2.6. The potentials $\mu_1(N-1, M-1)$ and $\mu_2(N-1, M-1)$ are above the μ_S and μ_D, thus they trap holes resulting in the DQD charge configuration being (N-1,M-1). $\Gamma_S, \Gamma_M, \Gamma_D$ are the tunnel rates between the source and QD1, QD1 and QD2, QD2 and the drain, respectively.

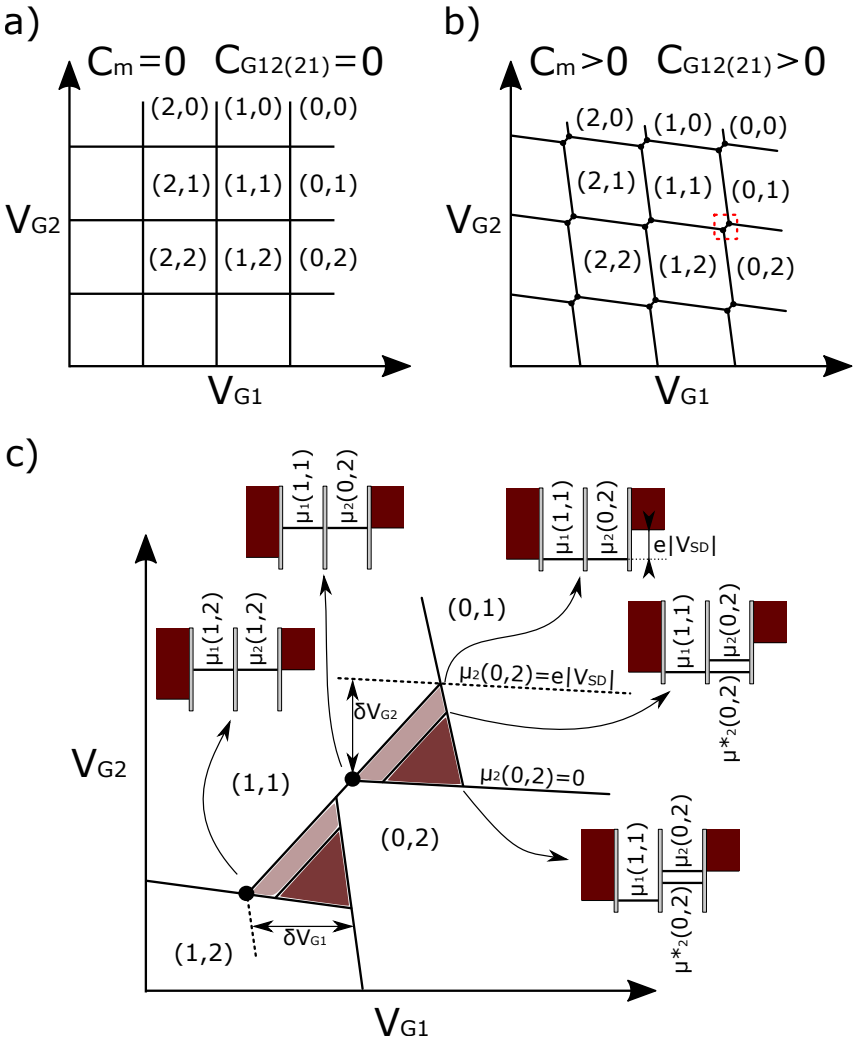


Figure 2.8: **Sketch of the charge stability diagram of a hole DQD. a** Vertical (horizontal) lines represent CPs of QD1 (QD2). For all the gate voltages inside one enclosed square, the charge configuration in the DQD is fixed. Going from far negative to far positive $V_{G1(2)}$, QD1(2) gets depleted. The mutual capacitance C_m and the cross-capacitances $C_{G12(21)}$ are considered to be zero here. **b** For $C_{G12(21)}, C_m > 0$ the lines form a honeycomb pattern. The crossing points from **a** are now splited into two triple points, in which three different DQD charge configurations meet. The triple points are connected with the inter-dot transition line. Sweeping gate voltages perpendicular to this line drives one hole between the two dots, while the overall charge number on the DQD stays the same. In **a** and **b** $V_{SD} \approx 0$. **c** Zoom-in into the (1,1)-(0,2) inter-dot transition, enclosed in the red dashed square in **b**. The condition $V_{SD} > 0$ evolves the triple points into corresponding bias triangles. The electrochemical potential alignments are shown for five characteristic gate-voltage configurations, at the edges of the triangles.

So far just charge states were considered. The spin state dependent charge transition, while changing the gate voltages along the detuning (ϵ) line (consult Figure 2.9) makes the transition between the charge state (1,1) and (0,2) interesting. The possible states for small ϵ are either the singlet S, in which the two-hole wave function has a symmetric orbital and anti symmetric spin part or the three triplet states T for which the symmetries are opposite. For zero magnetic field, S is the ground state and the three triplets are degenerate and higher in energy for both (1,1) and (0,2) charge configurations. In the (0,2) charge configuration, the singlet S(0,2) and the triplet T(0,2) form in QD2:

$$S(0,2) = (|\uparrow_2\downarrow_2\rangle - |\downarrow_2\uparrow_2\rangle)/\sqrt{2}$$

$$T_-(0,2) = |\downarrow_2\downarrow_2\rangle$$

$$T_0(0,2) = (|\uparrow_2\downarrow_2\rangle + |\downarrow_2\uparrow_2\rangle)/\sqrt{2}$$

$$T_+(0,2) = |\uparrow_2\uparrow_2\rangle$$

The subscripts mark the spin position in QD1 or in QD2. Due to the strong wave function overlap, the energy splitting between the singlet and the triplet in a single QD ($E_{ST(0,2)}$) is typically in the meV range, making the T(0,2) states not relevant in the scope of this work. In the (1,1) charge configuration, the S-T splitting is often called exchange splitting J. J is typically much lower than $E_{ST(0,2)}$, which, in addition to S(1,1), makes the three triplets relevant in the (1,1) charge configuration. Their spin parts read as:

$$S(1,1) = (|\uparrow_1\downarrow_2\rangle - |\downarrow_1\uparrow_2\rangle)/\sqrt{2}$$

$$T_-(1,1) = |\downarrow_1\downarrow_2\rangle$$

$$T_0(1,1) = (|\uparrow_1\downarrow_2\rangle + |\downarrow_1\uparrow_2\rangle)/\sqrt{2}$$

$$T_+(1,1) = |\uparrow_1\uparrow_2\rangle$$

In the CB regime, due to J being much smaller than other energy scales [Koppens *et al.*, 2007] the relevant energy levels are the $|\uparrow\rangle$ and $|\downarrow\rangle$ states in each QD (consult Figure 2.9b).

2.5.1 Pauli spin blockade

The mentioned spin state dependence of the charge state transition, occurs in the area between the green dashed baseline and the orange line in the triangles in Figure 2.9. The spin selection rules, stemming from the Pauli exclusion principle, allow the charge transition only for the singlet state. Such a mechanism of allowing or blocking the charge state transfer, depending on the spin state is called Pauli spin blockade (PSB) [Ono *et al.*, 2002] which allows readout of the spin state via charge sensing [Engel *et al.*, 2004]. If the electrochemical potentials are aligned as in Figure 2.9b, once the hole tunnels from the source contact to any of the T(1,1) states, the transport gets blocked. Depending on the energy separation between the S and T states, mechanisms such as nuclear field induced spin flip-flop processes, electrical noise via spin-orbit interaction or other, can lead to spin flips and consequently to the spin-blockade lifting. Recalling the particular case shown in Figure 2.9b, the higher energy T_+ or T_0 states can relax and the ground T_- state can be excited to the unblocked singlet state, resulting in a finite current in the PSB region.

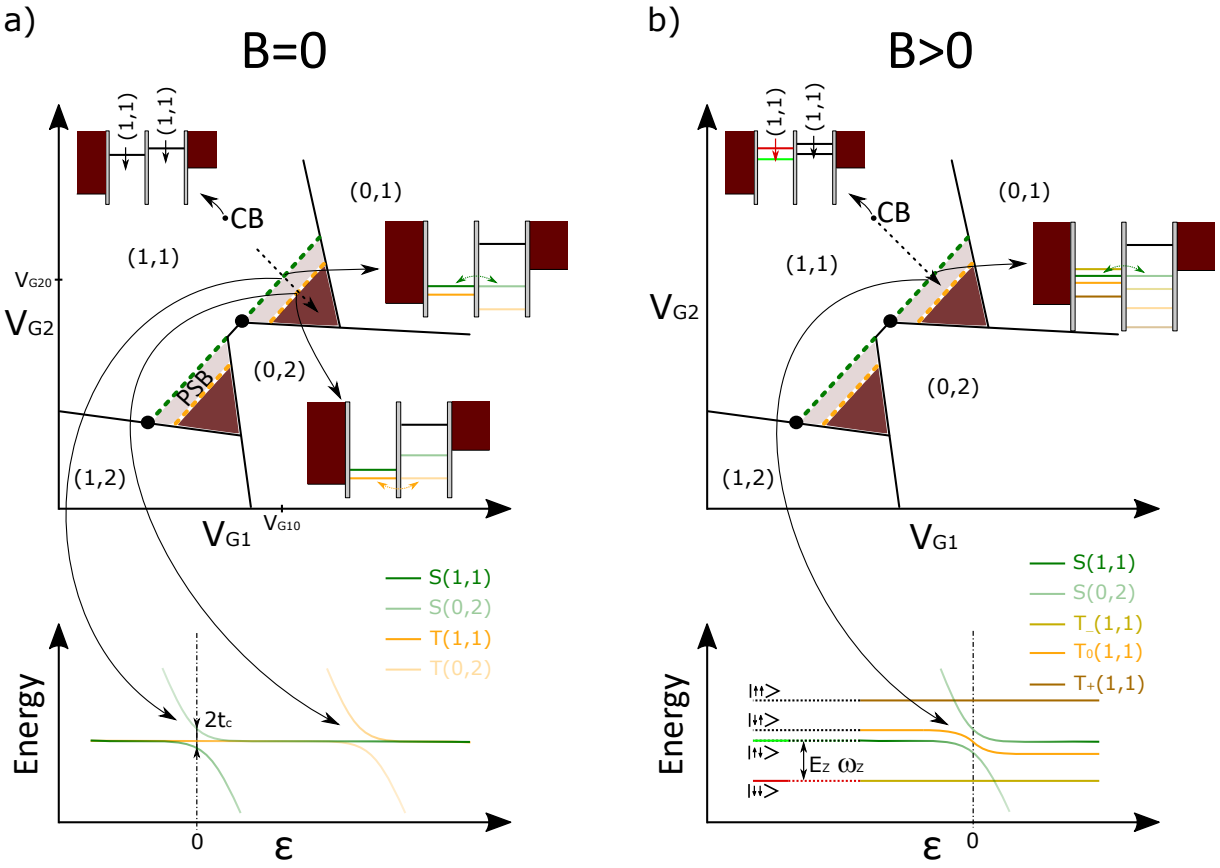


Figure 2.9: **DQD energy levels relevant for the experiments performed in this thesis.** The energies are depicted for the (1,1)-(0,2) charge transition. The bias triangles are formed due to $V_{SD} > 0$. Colored lines represent the states (darker ones the separated singlet and triplets and lighter ones joint singlet and triplets) and the dashed colored lines the transitions between the states. The DQD energies versus detuning ϵ, are shown at the bottom. The detuning is defined as the difference between S(1,1) and S(0,2) electrochemical potentials, $\epsilon = \mu_{S(1,1)} - \mu_{S(0,2)} = \alpha_1(V_{G1} - V_{G10}) - \alpha_2(V_{G2} - V_{G20})$, where V_{G10} and V_{G20} are the coordinates of zero detuning. The gate voltage along the detuning axis is marked with the black dashed arrow. **a** The electrochemical potential configuration is shown for gate voltages in deep CB, for the S(1,1) and S(0,2) alignment and for the T(1,1) and T(0,2) alignment. The transitions corresponding to the mentioned alignments are depicted with green and yellow dashed lines in the triangles (the current between the lines is small due to PSB), while the energy versus detuning shows the corresponding avoided crossings. **b** An applied magnetic field B splits the respective states by Zeeman energy E_Z. For large negative detunings (deep CB) those are the spin up and down states, while for ϵ around zero, those are the singlet and triplets. In the situation shown here $E_Z > t_c$ resulting in $T_-(1,1)$ being the ground state for $\epsilon = 0$. The detuning axis does not reach the triplet avoided crossing, so the joint triplets are not shown in the graph below. The difference between the g-factors in QD1 and QD2 causes different transition frequencies between the separated spin states. Still, if the g-factors are almost equal, one would see only one (instead of three) orange dashed lines in the triangles.

2.6 Loss-DiVincenzo qubit in a DQD

2.6.1 The qubit formation

The qubit described here is a Loss-DiVincenzo qubit encoded in a spin state of a hole. Deep in the CB spins in each QD can be treated separately and given that QD2 traps a spin down hole, the DQD states $|\downarrow_1\downarrow_2\rangle$ and $|\uparrow_1\downarrow_2\rangle$ can be translated to $|\downarrow\rangle$ and $|\uparrow\rangle$ states of the qubit hosted in QD1, respectively.

2.6.2 Initialization and readout

The qubit is initialized by mapping the PSB blocked triplet T_- to the $|\downarrow\rangle$ state in the CB region. In principle, loading any of the three $T(1,1)$ states is possible. However, since the qubit is driven only at a single frequency equal to ω_z, the g-factor difference makes the respective CB mappings of the T_+ and T_0 non sensitive to the applied drive (consult Figure 2.9b). Therefore, loading of T_+ and T_0 decreases the initialization fidelity, which is defined as the number of times when T_- is initialized divided with the total number of initializations. If all the three triplets have the same loading probability, the initialization fidelity would be 33$\%$. The initialization fidelity could be increased by e.g. waiting until the other initialized triplet states relax to T_-. But, the limitation of the spin manipulation period length, caused by the minimum readable transport current, prohibited this approach for the qubit measured in transport, which will be described below. From now on, S and T_- are taken to be the relevant states in PSB, while other two T(1,1) states are neglected and the initialization fidelity is taken to be 100$\%$. Regrading the readout, it works in the opposite fashion to the initialization, where the $|\downarrow\rangle$ from the CB maps to T_- in the PSB, therefore blocking the transport through the DQD. On contrary, $|\uparrow\rangle$ would map to $S(1,1)$ state, allowing the transport via the $S(0,2)$ state. Apart from transport, the qubit state can be also read out by sensing different capacitive contributions of the

blocked and unblocked states via the gate reflectometry [Crippa *et al.*, 2019].

2.6.3 Manipulation

In order to satisfy the DiVincenzo's criteria of having an universal set of qubit gates, the rotations about two orthogonal axis in the Bloch sphere need to be possible. The application of those gates enable the transition between any two arbitrary quantum states on the Bloch sphere. In case of a spin-1/2 system those rotations can be driven via an oscillatory magnetic field, applied perpendicular to the spin splitting static field, a mechanism also known as electron spin resonance. Alternatively, for systems with spin orbit coupling, spin manipulation is possible also via oscillating electric fields [Dobrowolska *et al.*, 1982; Golovach *et al.*, 2006; Hendrickx *et al.*, 2020] or g-tensor modulation [Kato *et al.*, 2003; Maurand *et al.*, 2016]. Additionally, a spin rotation can be driven via an optical excitation [Hanson *et al.*, 2007], pg 1254. We believe that the spin-orbit coupling enabled EDSR is responsible for the spin rotations in this thesis, as no electrically tunable g-factors have been shown for the HW system.

Rabi experiment

A typical experiment for proving a single axis spin rotation is the, so called, Rabi experiment. A step by step explanation of such an experiment, based on the EDSR mechanism in the DQD, introduced above, is given in the following.

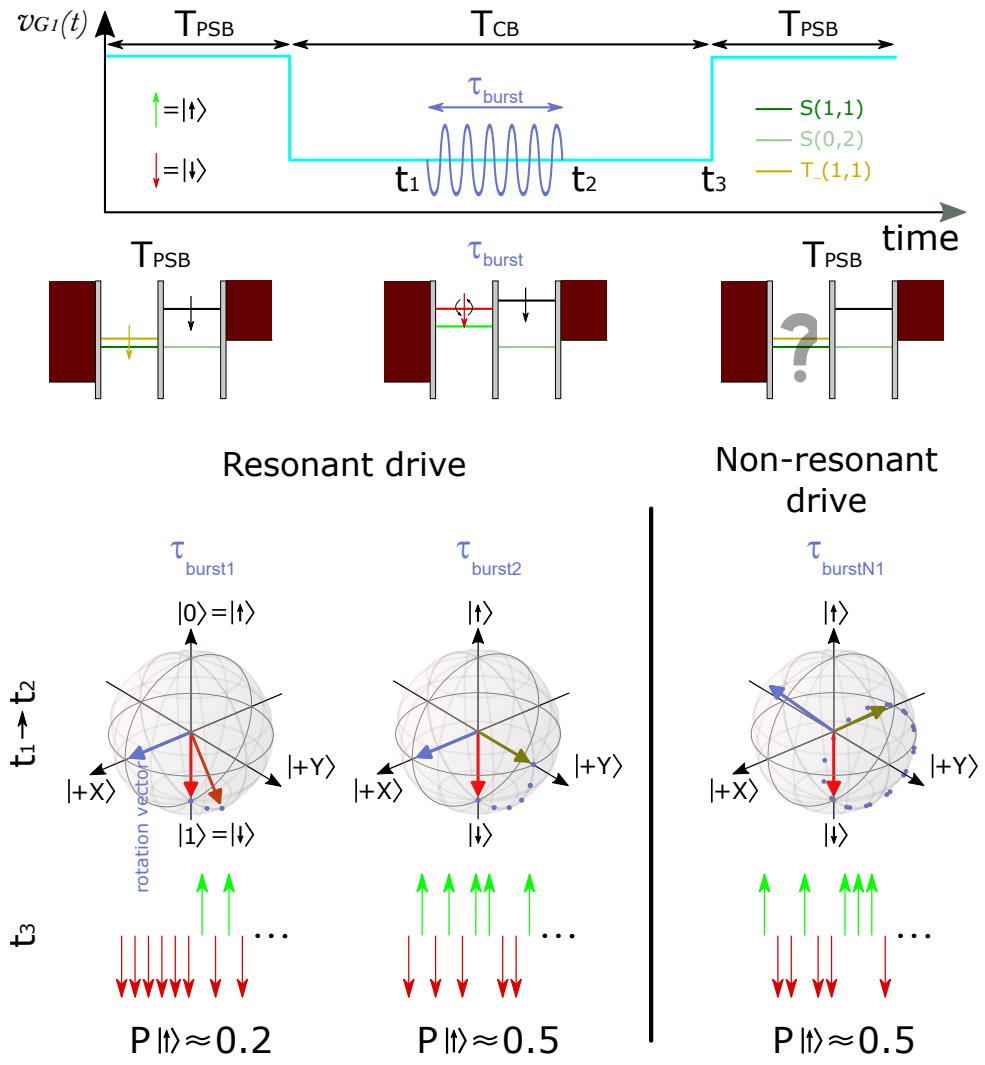


Figure 2.10: **Rabi experiment schematic.** The waveform applied to the QD1 gate $v_{G1}(t)$ is shown at the top. The duration of the CB (PSB) interval is marked with $T_{CB}(T_{PSB})$. The MW burst duration is marked with τ_{burst}. Each electrochemical potential configuration schematic shows the relevant energy levels alignment during the corresponding interval. The initialized spin down state, at the time point t_1, is represented by the pure red vector pointing down, in the Bloch spheres. The vector around which the state rotates during the MW burst (rotation vector) and the point-dashed trajectory the state describes during the rotation, are color matched to the darker blue color of the MW burst. At the time point t_2, the rotation stops and the final state is indicated with the corresponding final state vector. The ratio of red and green RGB color values in the final state vector color is proportional to $cos(\Theta)$, where Θ is a polar angle of the state (consult Figure 2.1). Bloch spheres with the rotation vector, initial and final state vectors, together with the state trajectories are shown for three different burst durations τ_{burst1}, $\tau_{burst2} > \tau_{burst1}$ and $\tau_{burstN1} > \tau_{burst2}$. A series of arrows, showed for the time point t_3, indicate the successive measurement outcomes, the average of which returns the spin up $P|\uparrow\rangle$ and the spin down $P|\downarrow\rangle = 1 - P|\uparrow\rangle$ state probability. The case of the non-resonant driving in which $\Omega = \omega_1$ (see text) is shown on the right.

The waveform $v_{G1}(t)$ drives the DQD between CB and PSB. During the T_{PSB}, once a hole tunnels from the source contact to a triplet state the transport gets blocked. The case for loading T_- is indicated in Figure 2.10 while the other two triplet states are not considered, as explained above. The triplet T(0,2) states are elevated in energy and therefore not shown as well. Switching v_{G1} towards more negative voltages, drives the DQD deep into CB where the initialized T_- state gets mapped at the spin down $|\downarrow\rangle$ state in QD1. In principle, to stay on the detuning axis, one would need to apply a counter acting waveform at the QD2 gate, but this is not absolutely necessary, since the switch between CB and PSB can be done also along a line parallel to V_{G1} in Figure 2.9. In CB, the initialized state is manipulated by the applied burst. As explained above, in the case of a resonant burst ($\omega_z = \omega_{REF}$) applied along the x-axis, the Hamiltonian from Equation 2.26 is valid. For the burst duration τ_{burst2}, the corresponding rotation operator $R_x(\omega_1 \tau_{burst2} = \frac{\pi}{2})$ can be read from Equation 2.28. Since the initialized state is $|\downarrow\rangle$, the resulting state after the burst can be calculated following Equation 2.29 as:

$$|\Psi_{rot}(t = t_2)\rangle = R_x(\frac{\pi}{2})\,|1\rangle = \begin{bmatrix} \frac{\sqrt{2}}{2} & -i\frac{\sqrt{2}}{2} \\ -i\frac{\sqrt{2}}{2} & \frac{\sqrt{2}}{2} \end{bmatrix} \begin{bmatrix} 0 \\ 1 \end{bmatrix} = \begin{bmatrix} -i\frac{\sqrt{2}}{2} \\ \frac{\sqrt{2}}{2} \end{bmatrix} = \frac{\sqrt{2}}{2} \begin{bmatrix} -i \\ 1 \end{bmatrix} = |+Y\rangle \tag{2.30}$$

At the moment of switching v_{G1} abruptly back towards the spin blockade (t_3), the spin in QD1 needs to "choose" the $|\uparrow\rangle$ or $|\downarrow\rangle$ state which consequently gets mapped to the S or T_- state, respectively. Depending on whether the state is on the southern (northern) hemisphere, after the rotation, the consecutive repetitions of the waveform yield more $|\downarrow\rangle$ ($|\uparrow\rangle$) resulting states, as illustrated with the series of red (green) arrows in Figure 2.10. Finally averaging across many of the consecutive outcomes, for the same τ_{burst}, returns in the probability of the spin state being up or down. By repeating this sequence for incrementaly increasing τ_{burst}, oscillation of the $|\downarrow\rangle$ ($|\uparrow\rangle$) state probability can be observed, with a so called Rabi frequency ω_1. An example of such a trace can be seen in Figure 2.11 in blue.

The discussion above considers resonant driving, namely $\omega_z = \omega_{REF}$. In practice the burst frequency can be detuned from the Larmor frequency causing a non-zero σ_z term in Equation 2.25 which gives the following Hamiltonian:

$$H_{rot} = \frac{1}{2}\hbar(\omega_z - \omega_{REF})\sigma_z + \frac{1}{2}\hbar\omega_1\sigma_x = \frac{1}{2}\hbar\Omega\sigma_z + \frac{1}{2}\hbar\omega_1\sigma_x \tag{2.31}$$

considering $\phi_p = 0$ as in the resonant case.

As can be seen from the Hamiltonian in Equation 2.31 and in Figure 2.10, in the case of a non-resonant driving, the spin rotates around an axis in the x-z plane. The angle of the rotation vector is determined by the $arctan(\frac{\Omega}{\omega_1})$ and the rotation frequency is increased to $\sqrt{\Omega^2 + \omega_1^2}$. The angle between the initialized $|\downarrow\rangle$ state and the rotation vector determines the small circle on which the state precesses during the rotation. In the particular case shown in Figures 2.10 and 2.11 for $\Omega = \omega_1$ the state rotates from 100% $|\downarrow\rangle$ to 50/50 mixture of $|\downarrow\rangle$ and $|\uparrow\rangle$, with a frequency $\sqrt{2}\omega_1$.

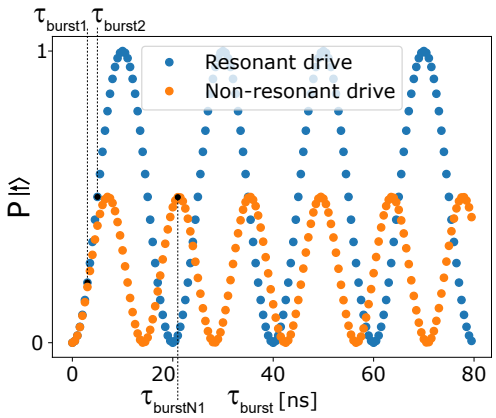


Figure 2.11: **Ilustration of ideal Rabi oscilation traces.** Simple sinusoidal traces generated in Python simulating the probability of measuring the spin up state $P|\uparrow\rangle$, at the time point t_3 versus linearly increasing τ_{burst}. Several oscillation periods are shown for both the resonant drive, with the frequency of $\frac{\omega_1}{2\pi} = 50\,MHz$ and the non-resonant drive, with the frequency of $\frac{\sqrt{\Omega^2+\omega_1^2}}{2\pi} = 50\sqrt{2}\,MHz$. The points for the three τ_{burst} from Figure 2.10 are indicated here as well. The traces color here have nothing to do with any other color in this thesis.

Two-axis qubit manipulation experiment

As mentioned above, in order to have a complete set of qubit gates, the rotations about two orthogonal axis in the Bloch sphere need to be possible. One of the possible experiments demonstrating such a rotation mechanism is explained in the following. Here we focus only at the CB interval of the experiment, since everything else is the same as in the Rabi experiment. Instead of applying a single burst during the T_{CB}, now $v_{G1}(t)$ contains two resonant (i.e. $\omega_z = \omega_{REF}$) bursts separated by the waiting time τ_{wait} (consult Figure 2.12). The duration of each burst is calibrated for a $\frac{\pi}{2}$ rotation, from the Rabi experiment. The phase of the first burst is zero, causing a $(\frac{\pi}{2})_x$ rotation of the initialized $|\downarrow\rangle$ state, to the equator of the Bloch sphere. During the waiting time the state is frozen. Recalling the Hamiltonian 2.25 one can see that ϕ_p determines the phase of the spin rotation vector in the x-y plane. Four different ϕ_p cases are shown in Figure 2.12. The probability $P|\uparrow\rangle$ is measured by averaging across many of the consecutive outcomes, for the same ϕ_p, as explained above. For $\phi_p = 0$, the rotation vector for both bursts is along x-axis, and the final spin state is 100% $|\uparrow\rangle$. For $\phi_p = \frac{\pi}{4}$ and $\phi_p = \frac{7\pi}{4}$ the final state has $\phi = \frac{\pi}{4}$ and $\phi = \frac{3\pi}{4}$ respectively, with $\Theta = \frac{\pi}{4}$ in both cases.

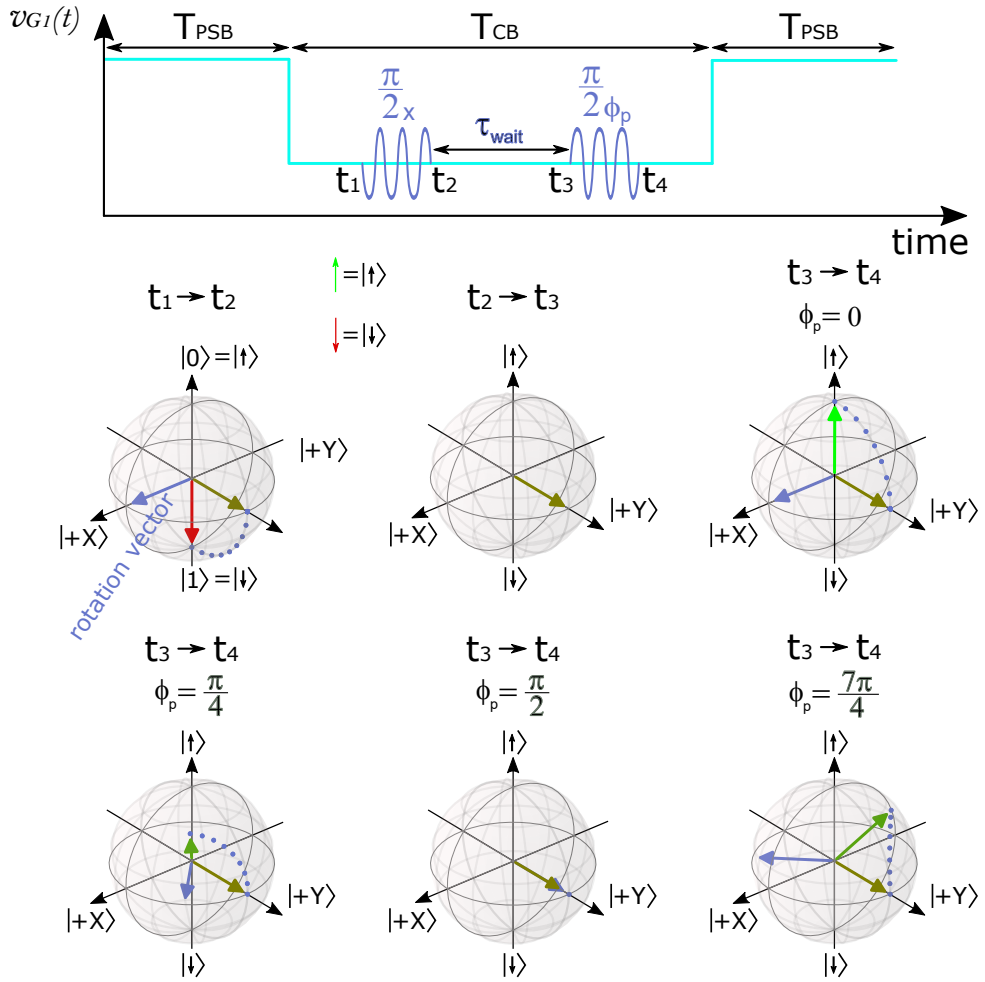


Figure 2.12: **Two-axis spin rotation.** The waveform applied to the QD1 gate $v_{G1}(t)$ is shown at the top. The duration of the CB (PSB) interval is marked with $T_{CB}(T_{PSB})$. Two bursts, separated by τ_{wait} are applied during the T_{CB}. The first burst causes rotation around the x-axis while the second causes the rotation around an axis in the x-y plane, the angle of which equals the initial phase of the second MW burst ϕ_p. The initial state, a state evolution trajectory around the indicated rotation vector and the final state are illustrated at the Bloch spheres for t_1 to t_2, t_2 to t_3 and for four different t_3 to t_4 intervals (four different ϕ_p cases). The first two intervals are the same for every waveform sequence. The color coding is the same as in Figure 2.10.

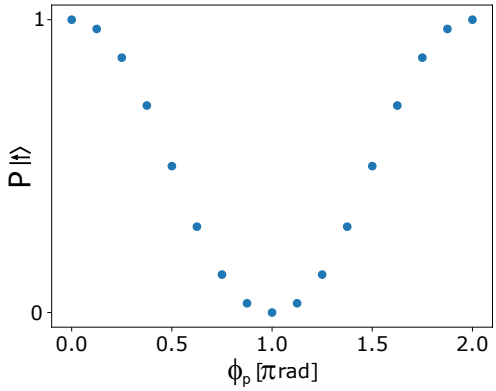


Figure 2.13: **Plot showing the probability of the state at the time point t_4 being up ($P\,|\uparrow\rangle$) versus ϕ_p of the second burst, simulated in Python (QuTiP).** While ϕ_p is being swept from 0 to 2π, the $P\,|\uparrow\rangle$ does one full sinusoidal oscillation.

The main point of the analysis is the case of $\phi_p = \frac{\pi}{2}$, illustrated at the lower middle Bloch sphere in Figure 2.12, which leads to the following Hamiltonian:

$$H_{rot} = \frac{1}{2}\hbar(\omega_z - \omega_{REF})\sigma_z + \frac{\hbar\omega_1}{2}(cos\phi_p\sigma_x + sin\phi_p\sigma_y) = \frac{\hbar\omega_1}{2}\sigma_y \tag{2.32}$$

The corresponding rotation operator can be calculated according to Equation 2.10 and for this case it is:

$$R_y(\frac{\pi}{2}) = \begin{bmatrix} \frac{\sqrt{2}}{2} & -\frac{\sqrt{2}}{2} \\ \frac{\sqrt{2}}{2} & \frac{\sqrt{2}}{2} \end{bmatrix} \tag{2.33}$$

Since the state at the time point t_3 is $|+Y\rangle$, for $\phi_p = \frac{\pi}{2}$ the final state after the second burst is then:

$$\begin{aligned} |\Psi_{rot}(t = t_4)\rangle = R_y(\frac{\pi}{2})\,|+Y\rangle = \begin{bmatrix} \frac{\sqrt{2}}{2} & -\frac{\sqrt{2}}{2} \\ \frac{\sqrt{2}}{2} & \frac{\sqrt{2}}{2} \end{bmatrix} \frac{\sqrt{2}}{2} \begin{bmatrix} -i \\ 1 \end{bmatrix} = \frac{\sqrt{2}}{2}\frac{\sqrt{2}}{2} \begin{bmatrix} -1-i \\ 1-i \end{bmatrix} \\ = \frac{\sqrt{2}}{2} e^{-i\frac{\pi}{4}} \begin{bmatrix} -i \\ 1 \end{bmatrix} = \frac{\sqrt{2}}{2} \begin{bmatrix} -i \\ 1 \end{bmatrix} = |+Y\rangle \end{aligned} \tag{2.34}$$

The fact that the $|+Y\rangle$ state remained the same after the second burst means that it was rotated around y-axis, which further **proves the rotation around two orthogonal axis**. In general, by sweeping ϕ_p of the second burst, from 0 to 2π, a sinusoidal oscillation of the spin up probability (consult Figure 2.13) proves the rotation around an arbitrary axis in the x-y plane.

2.6.4 Decoherence

In order to satisfy another DiVincenzo's criterion, the coherence time needs to be long in comparison to the rotation time. The general decoherence mechanisms for a spin-1/2 qubit, hosted in a DQD introduced above, together with the protocol for their quantification is explained in the following. The quantum state is considered coherent as long as it stays in the prepared state defined with Θ and ϕ (consult Figure 2.1). For the spin-1/2 system the interaction with the environment can flip the spin state (relaxation) and randomize or dephase ϕ, causing decoherence. This interaction is governed via the mechanisms of spin-orbit coupling, hyperfine coupling with the host material nuclei and virtual exchange processes with electrons in reservoirs. In case of very small tunnel rates towards the reservoirs and/or large detuning between the reservoirs and the dot electrochemical potentials, the last mechanism can be typically neglected [Hanson *et al.*, 2007](pg 1234). Which of the other two mechanisms will cause which decoherence effect (i.e. the spin state relaxation or the dephasing) is determined by the specific experimental parameters, e.g. host material, hole or electron, amount of applied magnetic field. In the case of heavy holes states in Ge, the p-type orbital symmetry is expected to greatly reduce the effect of the Overhauser field, whose longitudinal component B_N^z is the main cause of **dephasing** for electrons in GaAs [Hanson *et al.*, 2007](pg 1241). For the case of electrically tunable g-factors, the charge noise could cause the noise in the Larmor frequency and consequently the dephasing. However there are suggestions that charge noise insensitive, gate-voltage sweet spots can decrease the dephasing [Wang *et al.*, 2019]. Anyhow, the exact mechanisms leading to

a hole spin dephasing are yet be investigated.

The **relaxation**, on the other hand, is expected to be mainly caused by the fluctuations in the dot potential (phonons, charge noise, electrical noise at the gate electrodes coming from the room temperature instrumentation...) via the strong spin-orbit coupling. However, experimental findings non-negligibly deviate from what is theoretically predicted [Vukušić *et al.*, 2018].

For quantifying the decoherence, the dephasing time (T_2^*) and the relaxation time (T_1) can be measured separately. The experiment for measuring T_1 is presented in a previous thesis [Vukušić, 2018] and it will not be discussed here. T_2^* is typically measured by means of the Ramsey experiment, which is explained below.

Dephasing T_2^* - Ramsey experiment

In principle the Ramsey experiment can be performed following the same procedure as for the two axis qubit manipulation experiment, with the difference of sweeping τ_{wait} instead of ϕ_p. As can be seen in Figure 2.14, two bursts calibrated for the $(\frac{\pi}{2})_x$ rotation, in the resonant case, separated by the time interval τ_{wait}, are applied here as well. Apart from the resonant drive, also the non-resonant drive case, which consequently includes the z-axis rotation, is explained here. In the resonant case the $|+Y\rangle$ state, at the time point t_2, picks up a random phase during the τ_{wait} interval. The reason is the longitudinal noise component (as explained above), causing the randomization of the Larmor frequency and consequently the noisy σ_z term in Hamiltonian 2.25. Such introduces a random z-axis rotation and finally the mentioned random phase. Without the dephasing the subsequent $(\frac{\pi}{2})_x$ burst would result in $|\uparrow\rangle$ state which would translate to the singlet state in the PSB and result in the maximum current transport. As can be seen in Figure 2.15, from the blue trace, small τ_{wait}, even with dephasing, produces such a case. $P|\uparrow\rangle$ is measured by averaging amongst many final state outcomes, with random phases, for the same τ_{wait}. For increasing τ_{wait} the phase gets more randomized and consequently the measured $P|\uparrow\rangle$ is asymptotically approaching to the

50%. The decay of such a trace versus τ_{wait} gives information about dephasing. The decay shape might give an additional information about the noise, e.g. noise with a Gaussian distribution should cause a decay of a Gaussian form as well [Hanson *et al.*, 2007](1241). Fitting the trace with $e^{-(\frac{\tau_{wait}}{T_2^*})^2}$, then, allows to extract T_2^*. In the non-resonant case, apart from the dephasing there is a deterministic rotation around the z-axis caused by the non-zero detuning: $\omega_z - \omega_{REF} = \Omega \neq 0$. Therefore during τ_{wait} the state picks up also the deterministic phase $\Delta\phi = \Omega\tau_{wait}$. The linear increase of the state phase causes the oscillation in the measured probability $P|\uparrow\rangle$ as can be seen from the orange trace in Figure 2.15. This can be understood by observing the cases of τ_{wait1} and $\tau_{wait2} > \tau_{wait1}$ in Figure 2.14. From the rightmost Bloch spheres one can see that the state phase ϕ (Figure 2.1) at the time point t_3 determines the $P|\uparrow\rangle$ at the time point t_4. In particular, for τ_{wait1} the state at t_3 is almost $|-X\rangle$, rotated to the $|\downarrow\rangle$ state (indicated by a red arrow) by the second burst. The longer τ_{wait2} (longer z-rotation) produces the $|+X\rangle$ state at t_3 which is then being rotated to a northern hemisphere, indicated with the darker green arrow. So, apart from the dephasing measurement, Ramsey experiment demonstrates the ability to rotate the spin purely around the z-axis, during the τ_{wait} interval, due to the detuning ($\omega_{REF} \neq \omega_z$). It should be also noted that, during the two bursts the rotation vector is not along the x-axis, but it lays in the x-z plane, because the z-rotation is also present during the bursts and not only during the τ_{wait} interval. Thus, at the t_2 point the state is not perfectly at the Bloch sphere equator. But, as can be seen in Figure 2.14, even in the case of high detuning ($\Omega = \omega_1$) the state at t_2 is still close to the equator, so it is fine to call the applied MW bursts $\frac{\pi}{2}$ pulses.

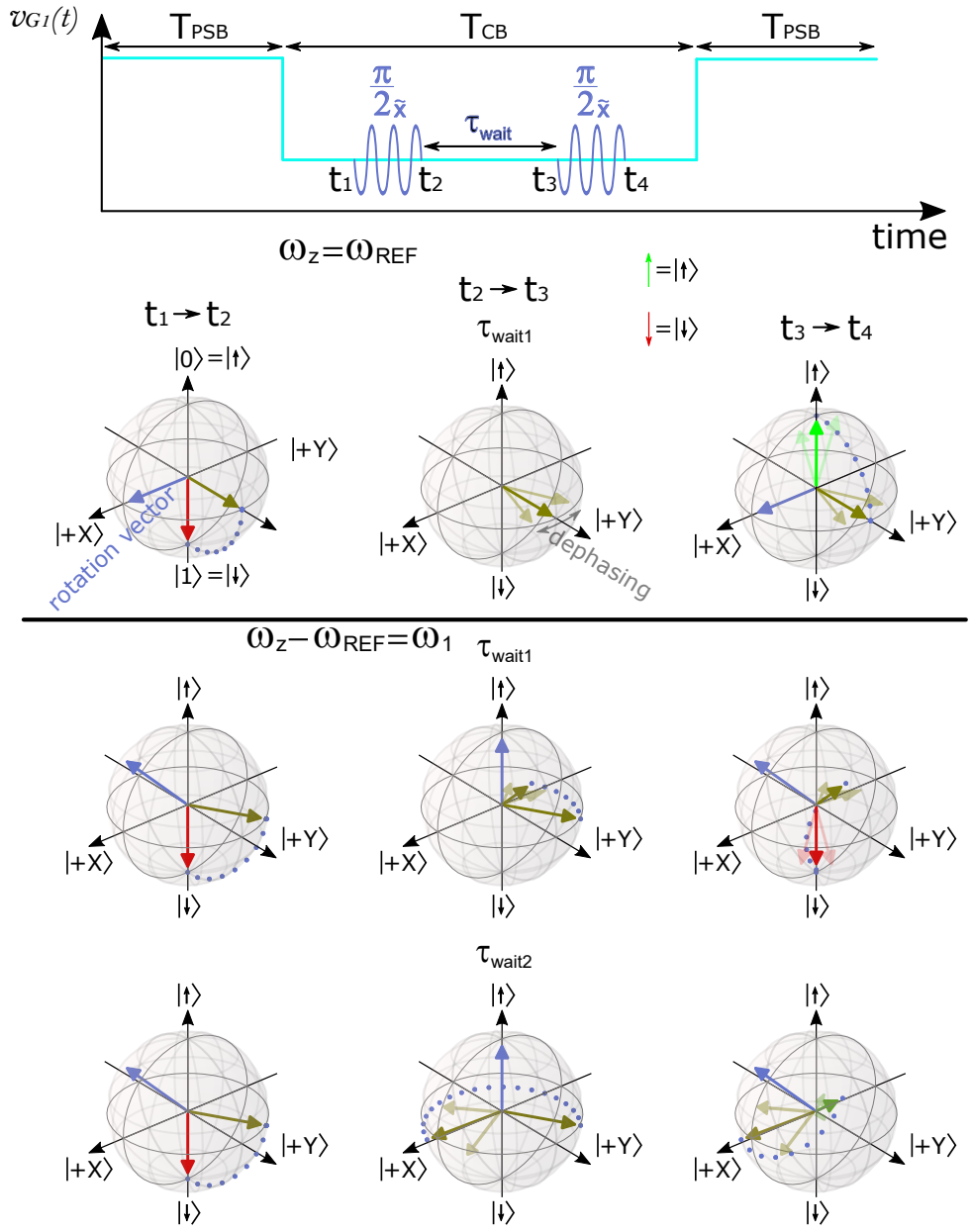


Figure 2.14: **Illustration of the Ramsey experiment.** The waveform applied to the QD1 gate $v_{G1}(t)$ is shown at the top. The duration of the CB (PSB) interval is marked with $T_{CB}(T_{PSB})$. Two bursts, separated by τ_{wait} are applied during the T_{CB}. The subscript $\tilde{x}$, instead of x, indicates that the rotation vector, corresponding to a burst, can be also in the x-z plane and not only along the x-axis. The rotation vector is a vector sum of the vector along the x-axis, with the amplitude (x-rotation frequency) equal to ω_1 and the vector along the z-axis, with the amplitude (z-rotation frequency) equal to detuning $\Omega = \omega_z - \omega_{REF}$. Therefore, in the resonant case ($\omega_z = \omega_{REF}$), rotation vector is along the x-axis and it is non-zero only during the bursts. In the detuned case, the rotation vector lays in the x-z plane during the bursts and during the τ_{wait} it is positioned along the z-axis. Initial state, a state evolution trajectory around indicated rotation vector and a final state are illustrated at the Bloch spheres for t_1 to t_2, t_2 to t_3 and t_3 to t_4 intervals. The considered condition for the detuned bursts is $\Omega = \omega_z - \omega_{REF} = \omega_1$ and it is shown for two different τ_{wait} ($\tau_{wait2} > \tau_{wait1}$) to illustrate the state evolution around z-axis due to detuning. The color coding is the same as in Figure 2.10.

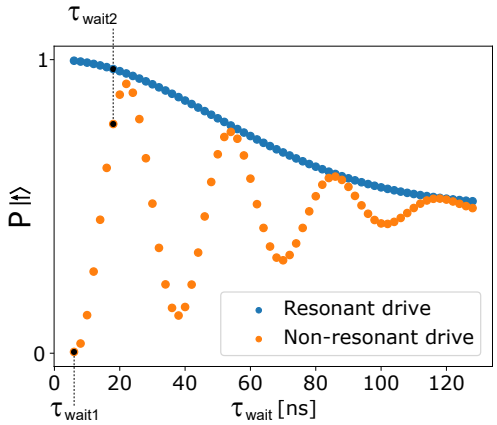


Figure 2.15: **Ramsey experiment with dephasing.** Plot showing the probability of the spin up state $P\left|\uparrow\right\rangle$ for both the resonant and the non resonant drive. In case of the non resonant drive, the detuning frequency $\frac{\Omega}{2\pi}$ is chosen to be $50\,MHz$, which is the frequency of $P\left|\uparrow\right\rangle$ oscillations. τ_{wait} is stepped in 2 ns steps and the cases for τ_{wait1} and τ_{wait2} from Figure 2.14 are indicated here as well. The two traces start with different $P\left|\uparrow\right\rangle$ because the first value of τ_{wait} is 6 ns, for which the phase of the non-resonant trace has a value of $\Delta\phi = \Omega\tau_{wait} = 2\pi 50 \cdot 10^6 \cdot 6 \cdot 10^{-9} = 0.6\pi\, rad$ causing approximately a minimum. The dephasing free data simulated in Python (Qutip), were multiplied with the Gaussian envelope $e^{-(\frac{\tau_{wait}}{T_2^*})^2}$ to simulate the dephasing. T_2^* was set to 70 ns, for both traces.

Decoherence in the Rabi experiment

Different rotation vectors in Rabi and Ramsey experiments cause sensitivity to different noise sources as well, causing decoherence on different length scales, with different decay shapes. For noise static at the Rabi period timescale, a power law decay has been observed [Koppens *et al.*, 2007]. Traces for the resonant and the non resonant driving in the case of a power law decay are illustrated in Figure 2.16.

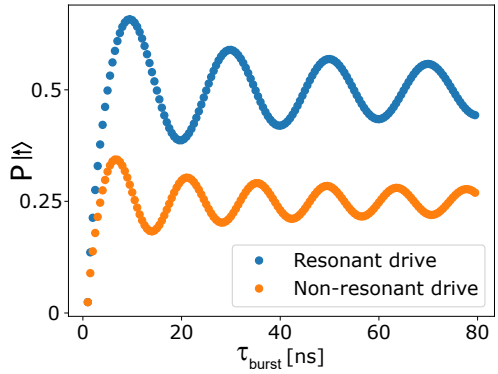


Figure 2.16: **Ilustration of Rabi oscilation traces with a power law decay.** The non-decaying sinusoidal traces in Figure 2.11 are multiplied with the envelope $\frac{1}{\tau_{burst}{}^{0.5}}$, to illustrate the power law decay. Each point represents an average over many experimental runs, yielding the probability of the $|\uparrow\rangle$ state for a single τ_{burst}. Several oscillation periods are shown for both the resonant drive, with a frequency of $\frac{\omega_1}{2\pi} = 50\,MHz$ and the non-resonant drive, with a frequency of $\frac{\sqrt{\Omega^2+\omega_1^2}}{2\pi} = 50\sqrt{2}\,MHz$.

3 Material and fabrication

As mentioned above, holes in Ge have many advantageous properties for a spin qubit implementation. The Ising type hyperfine interaction for heavy holes [Fischer *et al.*, 2008] states together with the possibility for isotopical purification of Ge could allow long coherence times. Meanwhile, the large and tunable spin orbit coupling should enable fast and fully electrical manipulation of hole spins.

3.1 Growth

The QDs used for confining hole spins in this thesis were formed in self-assembled Ge nanostructures, which appear as a result of the compressive strain relaxation of Ge layers grown on Si. Such a process is known as the Stranski-Krastanov growth mechanism [Mo *et al.*, 1990]. The realization of such structures starts with the deposition of a Si buffer layer on a Si wafer (typically with 001 crystaline orientation). The highly controllable material deposition rate, in the molecular beam epitaxy machine, allows subsequent deposition of a few Ge monolayers. Due to a 4% larger crystal lattice, compressive strain builds up in Ge, which is getting released through formation of hut clusters (Figure 3.1a). With the correct amount of the deposited material and the temperature of the subsequent annealing step, the clusters can evolve into defect free HWs [Zhang *et al.*, 2012; Watzinger *et al.*, 2016; Watzinger *et al.*, 2014], with lengths up to $\sim 2\,\mu m$, a base width of $\sim 20\,nm$ and a height of $\sim 2\,nm$ (Figure 3.1b). In order to

avoid Ge from being oxidized, a few nm thick Si cap is deposited as the last step. The samples used in this thesis were fabricated out of HWs grown by Hannes Watzinger at JKU Linz and Fei Gao working in the group of J.J. Zhang at the Chinese Academy of Sciences. More specific growth parameters can be found in [Watzinger, 2018].

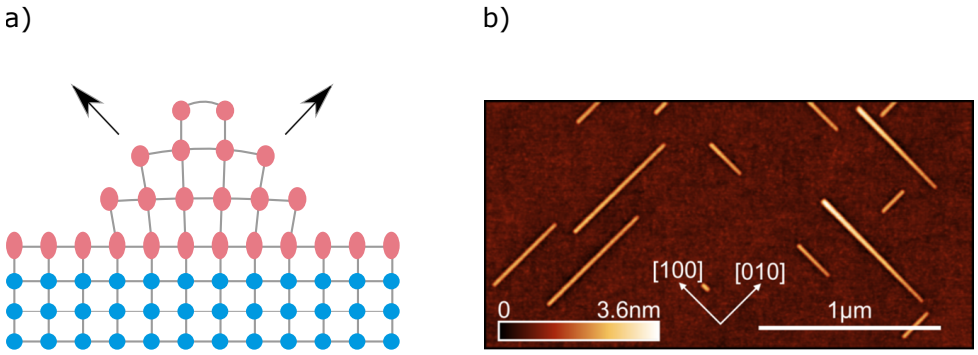


Figure 3.1: **HW growth. a** Illustration of a hut cluster formation due to the compressive strain in the Ge atomic layers (pink dots) grown of Si (blue dots) **b** Atomic force microscopy image of a sample showing up to $1\mu m$ long HWs [Watzinger *et al.*, 2016].

3.2 Band structure

The Luttinger Hamiltonian describes the top of the valence band of Ge at much lower energies than the split-off splitting. One distinguishes between the heavy hole, light hole and split-off band. We can safely ignore the split-off band due to the large spin-orbit in Ge. This allows us to restrict ourselves to the $J = 3/2$ subspace. The Luttinger Hamiltonian can be thus written as $H = \begin{bmatrix} H_{HH} & H_{HL} \\ H_{LH} & H_{LL} \end{bmatrix}$, where the diagonal terms describe the heavy and light holes and the off diagonal the mixing (each of the terms is a 2x2 matrix) [Katsaros *et al.*, 2011]. Strain and confinement lead to splitting of heavy holes and light holes. The very small HW height leads to a large confinement, resulting in a heavy hole-light hole splitting larger than $500\,meV$ [Watzinger *et al.*, 2016] and thus the light hole band can be ignored. As a consequence, the Hamiltonian of our system can be described by a 2x2 matrix made-up of the heavy hole spin-3/2 state.

This resembles a spin-1/2 system.

3.3 Hut wires and double quantum dots

The Si-Ge-Si sandwich (Figure 3.2a), the Ge HW encapsulated between the Si buffer and the cap, results in a type-II valence band alignment [Yakimov *et al.*, 2006], creating a confinement potential for holes inside the HW. In order to form a confinement in all the three spatial directions, a confinement along the HW axis is induced by a metallic gate, below which a QD forms. Furthermore, by putting two metallic gate electrodes next to each other (Figure 3.2b), a DQD is formed. The thin layer of oxide, which is a combination of the native Si oxide and typically a Hafnium oxide (HfO_2) deposited on top of it (not shown in the figure), separates the HW and gate electrodes. For being able to do hole transport through the DQD, the deposited source and drain metal needs to have a high work function. Like this, a DQD system, sketched in Figure 2.6, can be physically achieved. In order to be able to control all the tunnel couplings, initially we tried to implement a five gate device. But, it turned out that QDs form below the gates presumably due to strain [Park *et al.*, 2016] and therefore a DQD was much easier to achieve in a two gate device. Also, initial trials with side gates, instead of overlapping ones, did not work very well.

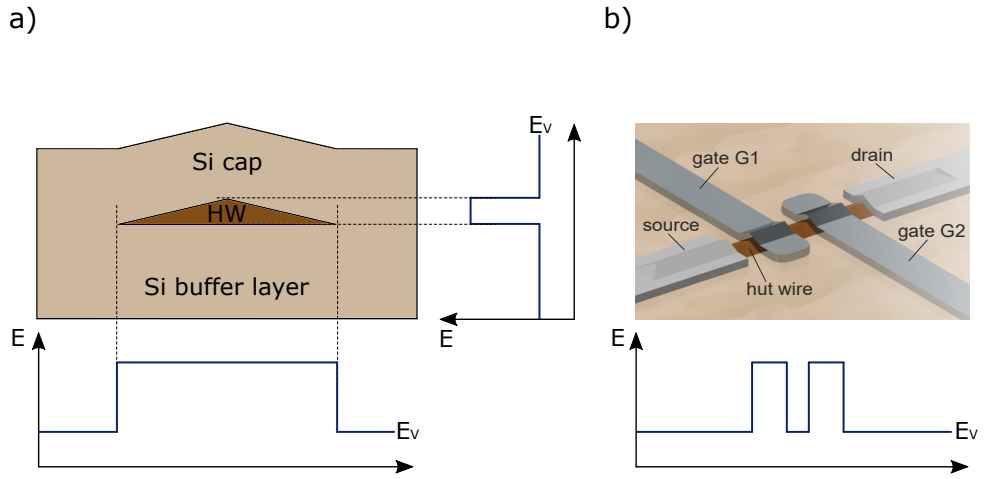


Figure 3.2: **Illustration of the valence band alignment and a DQD in a Ge HW. a** Illustration of the cross section of a HW grown on a Si buffer layer and surrounded by the Si cap. The graph below shows the valence band (E_v) alignment between the surrounding Si and the Ge HW. The valence band is higher inside the HW. **b** Illustration of a two gate DQD made out of a Ge HW. It is drawn by Hannes Watzinger and presented here with his permission. Metallic gates covering the HW cause additional confinement of holes, along the HW axis, creating thus a DQD.

The major drawback of two gate DQDs is the limited tunability, but it was possible to achieve a satisfactory amount of tunnel couplings by adjusting the separation between the leads and the gates and the gates themselves. On the other hand, the two gate structure carries a great advantage as well, which is a reduced complexity of both fabrication and experimental protocols later on.

3.3.1 Fabrication of DQDs

The nanometer dimensions of DQD devices make them very fragile during the fabrication process, meaning that dust or other micron-sized particles can destroy the device. Therefore, all the devices were fabricated in a cleanroom with ISO 7,6 and 5 certificates. The fabrication starts with cutting the HW wafer, typically into 2x2 cm^2 chips. A set of alignment markers is then ”written” on such a chip. For this, a positive electron beam resist (typically PMMA 4$\%$ 950K) is spinned on the chip’s surface and baked.

Next, by using a 100 kV Raith EBPG5150 EBL (e-beam) machine, the marker pattern is ”written” on the resist with the electron beam. After removing the exposed parts of the resist, with the resist developer, Cr/Au 10 nm/50 nm is deposited using a Plassys MEB 550S metal evaporator. All the metal residing on the resist is then removed by the lift-off process, typically in Acetone at $55^0\,C$, leaving the metal only at positions where the resist had been exposed to the electron beam. Next, the 2x2 cm^2 chip is cut into smaller 6x6 mm^2 chips. The surface of such a 6x6 mm^2 chip is then imaged with the scanning electron microscope (SEM) Teneo LV in order to find HWs. An example of such an image, showing a small region of the 6x6 mm^2 chip, after the marker fabrication, can be seen in Figure 3.3a. Those SEM images are then incorporated into the layout drawing software where marker image representations are aligned with the marker layout design and the layout of contacts is drawn onto a specific HW, picked from the image. Next, by aligning the e-beam exposition pattern, generated from the drawn contact layout, to the markers, in the e-beam machine, a nm precise contacting of the chosen HW is achieved. By repeating the fabrication steps, as explained for markers, namely spinning and baking of the resist, e-beam writing, metal deposition (typically $\sim 25\,nm$ of Pt) and lift-off, source and drain contacts are fabricated as the next layer. Right before the source and drain metal deposition, a 10 seconds HFA (hydrofluoric acid) dip, for removing the native Si oxide and getting thus good contacts to the HW, is performed. The subsequent fabrication of the gate layer follows a similar procedure as well. The typically used resist for gates is CSAR 13$\%$ and the typical gate metal is Ti ($\sim 5\,nm$), as a sticking layer, and Pt ($\sim 25\,nm$) bilayer. Before the gate metal deposition, an insulating oxide layer, with a typical thickness between 4 and 10 nm, is deposited using the atomic layer deposition machine (ALD) FlexAL II from Oxford. An example of a DQD device after the fabrication can be seen in Figure 3.3b and c.

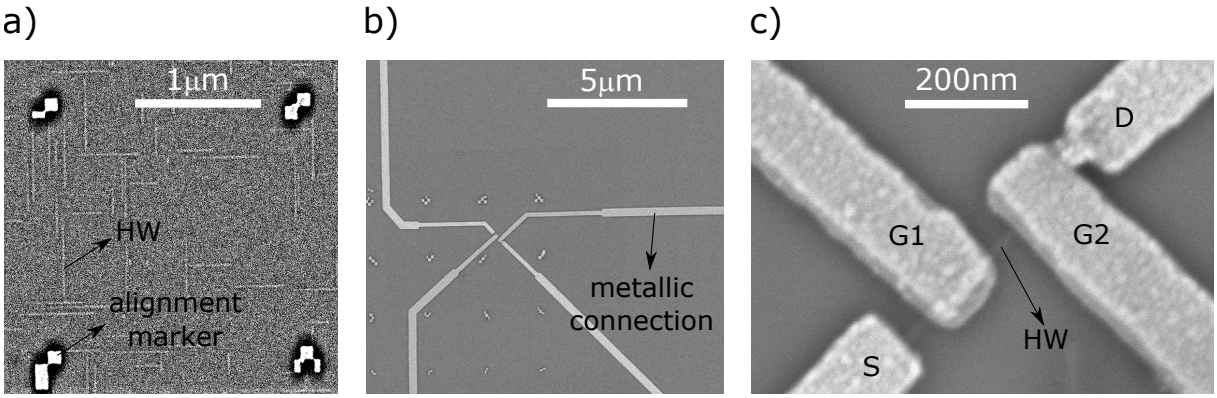


Figure 3.3: **SEM images illustrating the Ge HW DQD fabrication steps. a** Adjusted 2x2 μm^2 SEM image showing randomly distributed Ge HWs on the Si substrate and alignment markers. Thresholds of the original image are adjusted for better hut wire visibility. **b** A zoomed out SEM scan of the qubit hosting DQD device, fabricated by Hannes Watzinger. The metallic leads connect the DQD electrodes with bonding pads (consult Figure 3.5a). **c** A zoomed in SEM scan of the qubit hosting DQD device. The Ge HW, which is also visible, is contacted with S, D, G1 and G2 electrodes. The metal blob, non-intentionally standing in between the G2 and D electrodes did not cause a short in DC (direct current) terms but it could be the reason why the device did not react to HF signals sent to G2.

Reducing the oxide thickness

The initial two gate DQD devices, like the one used for the qubit, shown above, had $\sim 8\,nm$ of HfO_2 on top of a thin layer of the native Si oxide, formed due to the natural oxidation of the HW Si cap. Gate reflectometry on such devices did not work reproducibly and the measured signal was too weak. In order to increase the signal by increasing the gate to dot coupling factor, we decided to reduce the oxide thickness, namely to etch away the native Si oxide and to deposit a smaller amount of the HfO_2 oxide. Removing the native Si oxide was done right before the ALD deposition of the HfO_2 oxide. For this, after developing the resist with the e-beam patterned gate design, the samples were dipped into HFA for 10 seconds, same as for the leads. In order to avoid the formation of the native Si oxide, the samples were, in the shortest possible amount of time, put into the ALD machine under vacuum conditions, where a precise amount of HfO_2 oxide got deposited on top. The illustration of the HW cross

section before and after HFA dip and after the complete fabrication is shown in Figure 3.4.

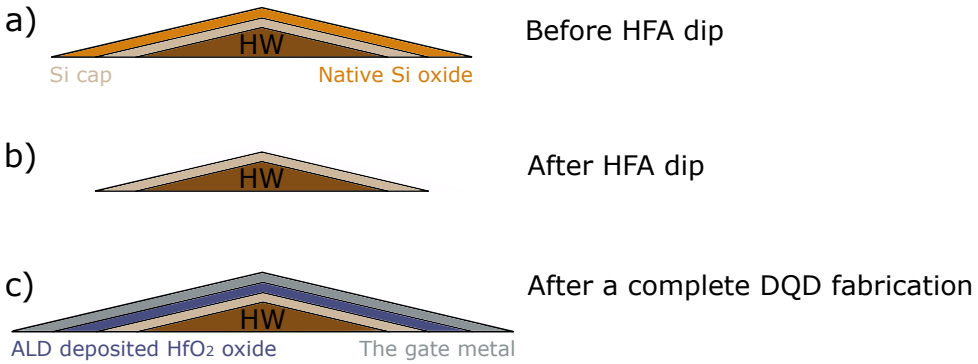


Figure 3.4: **Illustration of the HW cross section after different fabrication steps.** The illustrated layer thicknesses are not in scale with the real layer thicknesses. **a** Illustration of the cross section before the fabrication. Approximately 2 nm of native Si oxide covers a few nm thick Si cap. **b** Immediately after the HFA dip, the native Si oxide is expected to be removed. **c** HfO_2 oxide is deposited in the next step, in the ALD machine, with the typical thickness varying from 4 to 10 nm. Subsequently, the gate metal is deposited on top of the HfO_2 oxide.

Etching

In order to try to reduce the amount of background features and noise in the gate reflectometry signal, the HW chips were etched by bombarding them with Ar ions in the Plassys evaporator machine. The CSAR 13% resist was protecting only a few tens or a few hundreds of μm^2 large area around the target HW. From all the remaining sample surface, the Si cap and the Ge layer, together with the HWs, were etched away. The typically applied etching recipe was: 300 V, 10 mA, 4 sccm of Ar, applied during two min intervals, repeated four times, with a waiting time of 5 min in between the etching intervals. This should result in the etching depths between 8 and 20 nm, which is deep enough to remove the Si cap and the Ge layer. A zoomed out view of the etched DQD device in Figure 3.5a shows the idea of etching, namely that all the metallic connections are routed inside the etched area, reducing thus the amount of charges below them. In Figure 3.5c the non etched area was further decreased while

the etching was additionally applied below the gate contacts all the way up to a distance of a few hundred nm from the HW.

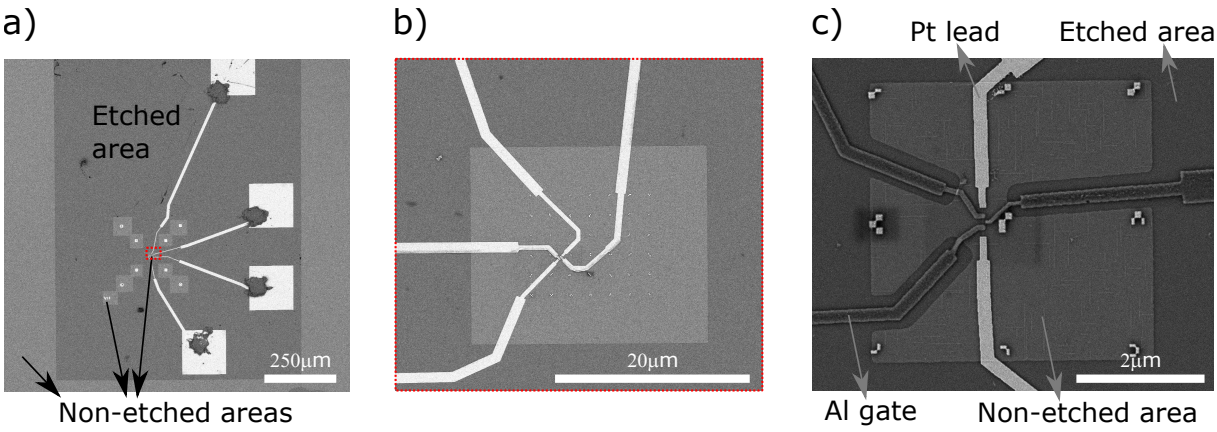


Figure 3.5: **SEM images of etched Ge HW DQD samples. a** SEM image of one DQD device showing all the metallic connections and bonding pads (bright squares). All the metallic connections, especially gates, are positioned inside the etched area, which appears a bit darker in the images. **b** Zoom in into the red dashed square in **a**, showing approximately $20x20\,\mu m^2$ of a non etched area around the contacted HW. **c** SEM image of one device on another sample. The non-etched area was reduced to a few tens of μm^2 around the contacted HW. Etching was additionally applied below the Al gate electrodes, until a few hundreds of nm before the contacted HW. The Pt source and drain leads appear brighter because Pt is a heavier element than Al and thus scatters back more electrons.

For some wafers, the presented etching technique caused electrical shorts between all or several metallic connections inside the etched area (consult Figure 3.5a). The wafer called ”S228”, grown in China, did not show this, while the other one called ”MJ”, grown in the same molecular beam epitaxy machine, had this problem. Also, a wafer grown in Linz, called ”4274”, had this problem. The origin of this behavior is still not clear.

Different gate oxide and addition of a middle gate

At the present stage, a controllable tuning of DQDs is needed for qubit devices. To achieve this, a middle gate was implemented in the DQD design. After several samples were fabricated and measured, the version with the middle gate on top, whose layout can be seen in Figure 3.6a, proved to be the best as confirmed by the results from

two samples. The main gates are separated from the HW by a native Al oxide. The oxide was formed by heating the sample to $150^0\,C$ for 5 min, after Al deposition, which should result in a few nm thick Al oxide. The middle gate was fabricated afterwards in a subsequent e-beam step. The oxide layer below the middle gate is a 30 nm thick Al oxide, deposited in the ALD at $300^0\,C$. It is very thick to relax the strain coming from the gate metal, to avoid an additional, strain induced, QD below it. After the oxide deposition, the middle gate was patterned and Ti/Pt 5/30 nm was deposited.

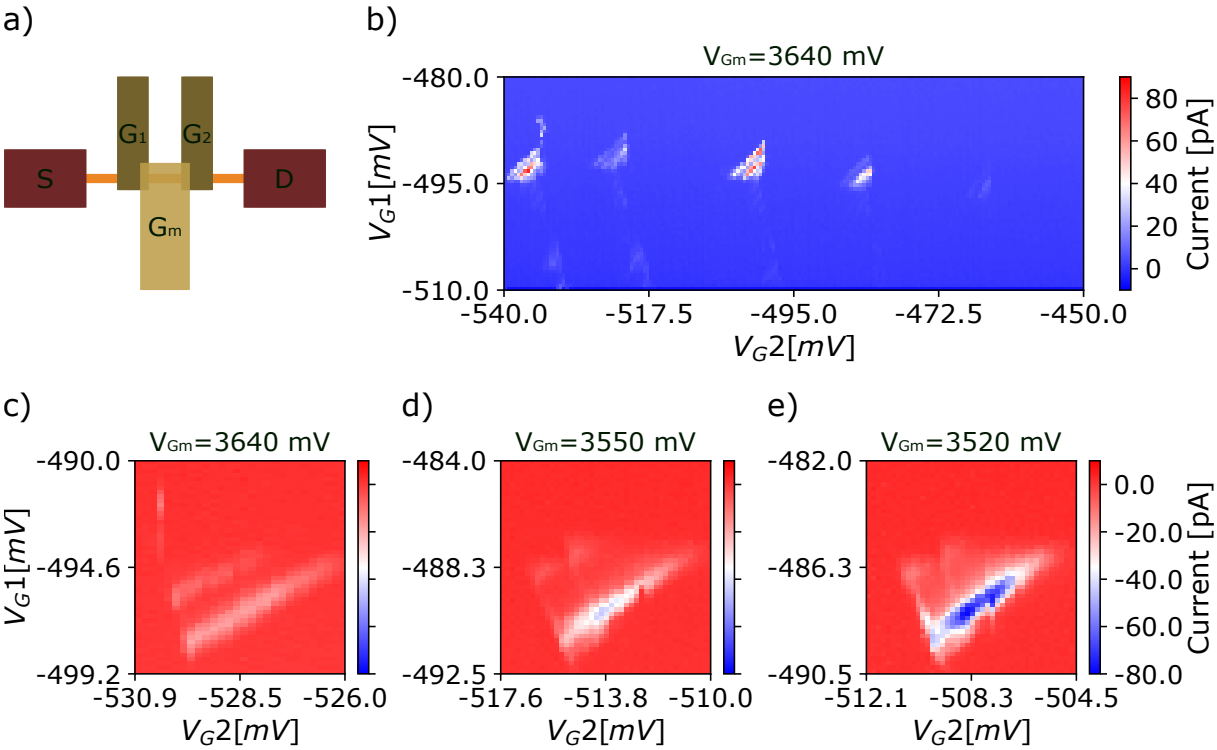


Figure 3.6: **Tunable DQD tunnel coupling on the "MJ_5_S33" sample. a** Illustration of a DQD with a middle gate on top. **b** Larger V_{G1} versus V_{G2} scan, taken with $V_{SD} = 2\,mV$ showing a series of bias triangles with a possible PSB. **c,d** and **e** Zoom in into a pair of bias triangles, taken with $V_{SD} = -2\,mV$. The transport current increases with decreasing middle gate voltage (V_{Gm}), indicating a decrease of the middle tunnel barrier. The color bar is the same for all the three graphs. Going from left to right, the range of V_{G1} and V_{G2} is shifting to more positive values in order to compensate the triangle shift for more negative V_{Gm} values.

The layout of the "MJ_5_S33" DQD sample, with the middle gate on top, which showed the best results out of several fabricated samples, is illustrated in Figure 3.6a. A larger

stability diagram (Figure 3.6b), reveals a pattern of bias triangles with a current (coupling) range, similar to the one of the qubit hosting DQD (consult Figure 5.2). The zoomed in pair of bias triangles, shown in Figure 3.6c, d and e, taken for a decreasing middle gate voltage, indicates the tunability due to the middle tunnel barrier. Going towards more negative middle gate voltages, reduces the height of the middle tunnel barrier (most probably), increasing thus the transport current.

The problems with this batch of samples were instabilities and non wanted additional features in the gate reflectometry readout, as can be read in Chapter 6.

Conclusion

Initially we started with two gate DQDs and one of them had good enough parameters to be a qubit host, which was measured in current transport (Chapter 5). A good gate reflectometry signals started to be reproducibly obtained after the described oxide thickness reduction and etching. But, a very small leak free gate range prohibited the necessary tuning towards the qubit regime. Therefore, a wider range of fabrication parameters was examined. Firstly, the HfO_2 oxide was replaced with the Al oxide and the middle gate was added in order to achieve the necessary tunability of the inter-dot tunnel barrier. Out of several fabricated samples, the one with overlapping middle gate, separated by a 30 nm Al oxide, showed a good potential for tuning towards the qubit regime. Here, the obstacle was the sample instability. A previous batch of etched samples with an HFA dip before the gate oxide deposition showed a better stability and a reduced amount of background features. But, the middle gate test samples were fabricated out of the ”MJ” wafer which showed the mentioned electrical shorting problems, when etched.

In conclusion, it seems that the addition of the middle gate in combination with another wafer, which would allow etching and HFA removal of the native Si oxide, might lead to both more stable and tunable devices.

Sample name	Wafer name	Source and drain metal	Gate metal	Gate oxide	HFA dip	Ar etching
The qubit sample	4279	Pt 25 nm	Ti/Pt 3/25 nm	ALD grown thermal $HfO_2 \approx 8\,nm$	no	no
S228_111	S228	Pt 25 nm	Ti/Pt 3/25 nm	ALD grown thermal $HfO_2 \approx 6\,nm$	yes, described above	yes, described above
MJ_5_S33	MJ	Pt 25 nm	Main gates: Al 25 nm Middle gate: Ti/Pt 5/30 nm	Main gates: native Al_2O_3, $150^0\,C$, 5 min Middle gate: ALD grown Al_2O_3 at $300^0\,C$, $\approx 30\,nm$	no	no

Table 3.1: **Parameters of samples, measurements of which are reported in this thesis.** HFA dip is the one before the gate oxide deposition, for the native Si oxide removal, as explained above.

4 Setup

Let's first clarify the notation regarding high frequencies, before starting the description of the setup. High frequency (HF) includes complete frequency spectrum of high-frequency signals, starting form MHz. It is subdivided into RF (radio frequency), which covers a range from MHz until hundreds of MHz and microwave (MW) which covers everything above. The subdivision is introduced to make clear distinction between the reflectometry, which operates in hundreds of MHz, and a qubit manipulation signals which reside in the GHz range. As can be seen at Figure 4.1 the setup consists of instruments for providing a low temperature environment, magnetic field for the experiments involving a spin, for providing stable and low noise DC voltages and currents, for measuring DC currents and voltages, for generating arbitrary waveforms and GHz sinusoidal signals and for a phase sensitive detection. Low temperatures are provided by the dilution refrigerator and more about it can be found in Section 4.1. The magnetic field is generated by a two-axis superconducting 9/3 T vector magnet controlled with the power supply from American Magnetics AMI 430. For generating and measuring LF and DC signals, the battery powered IVVI electronics is used. Voltages are generated by the low noise DAC module as a part of the IVVI electronics. The current is measured by isolated current to voltage (IV) converters and it is generated by voltage to current (VI) converters, therefore the name IVVI. It is designed by Raymond Schouten from QuTech at Delft University of Technology. LF signals generated by the IVVI DAC enter the LF circuit through the matrix box, as can be seen in Figure 4.2. The matrix box addresses each PCB bonding pad and consequently the measured sample electrode

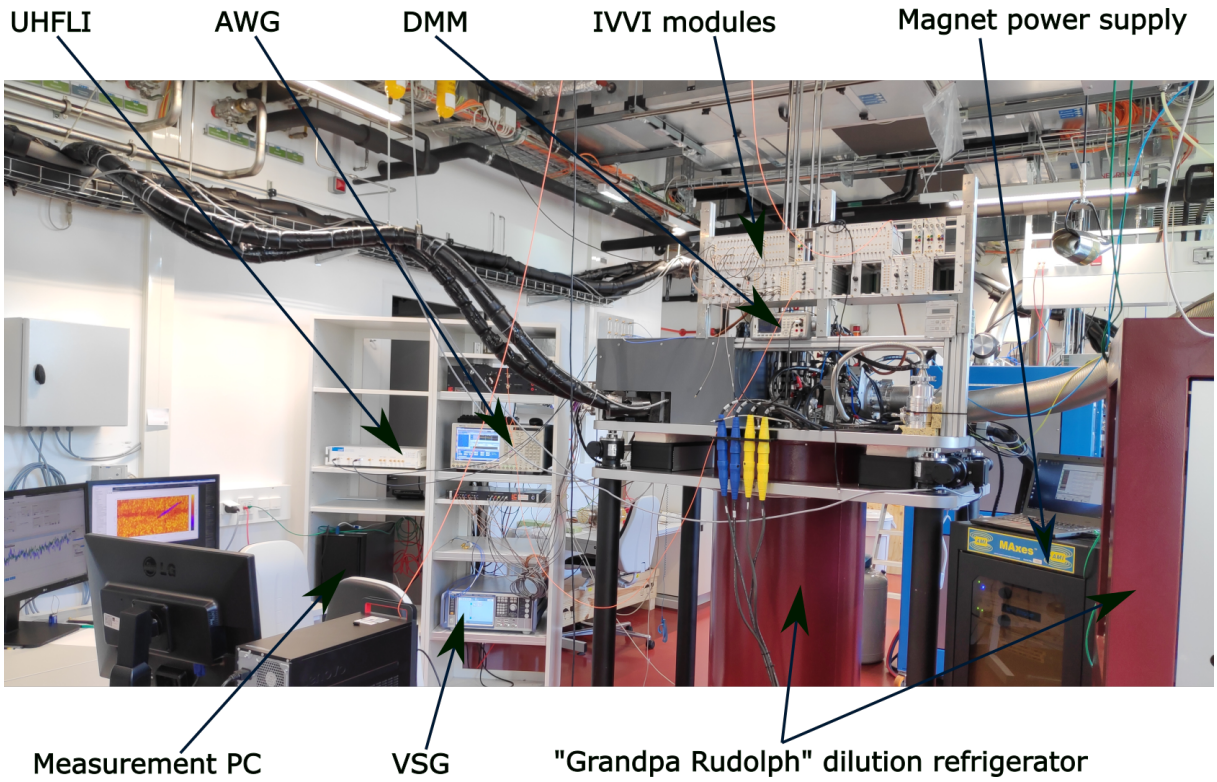


Figure 4.1: **Image of the full setup used in the majority of the experiments described in this thesis.** The red cylinder is the main unit of the dilution refrigerator called ”Grandpa Rudolph”. IVVI modules mounted on the top of the fridge consist of the IVVI rack with the digital to analog converter (DAC) and the matrix box. Below the IVVI, there is the digital multimeter (dmm), Agilent 34410. Instruments for HF signal generation and measurements are located in the wooden rack, left to the fridge. These are the arbitrary waveform generator (AWG) Tektronix AWG 5014C and the vector signal generator (VSG) SMW200A from Rohde&Schwarz. For the phase sensitive signal detection, we used the ultra high-frequency lock-in (UHFLI) amplifier from Zurich Instruments.

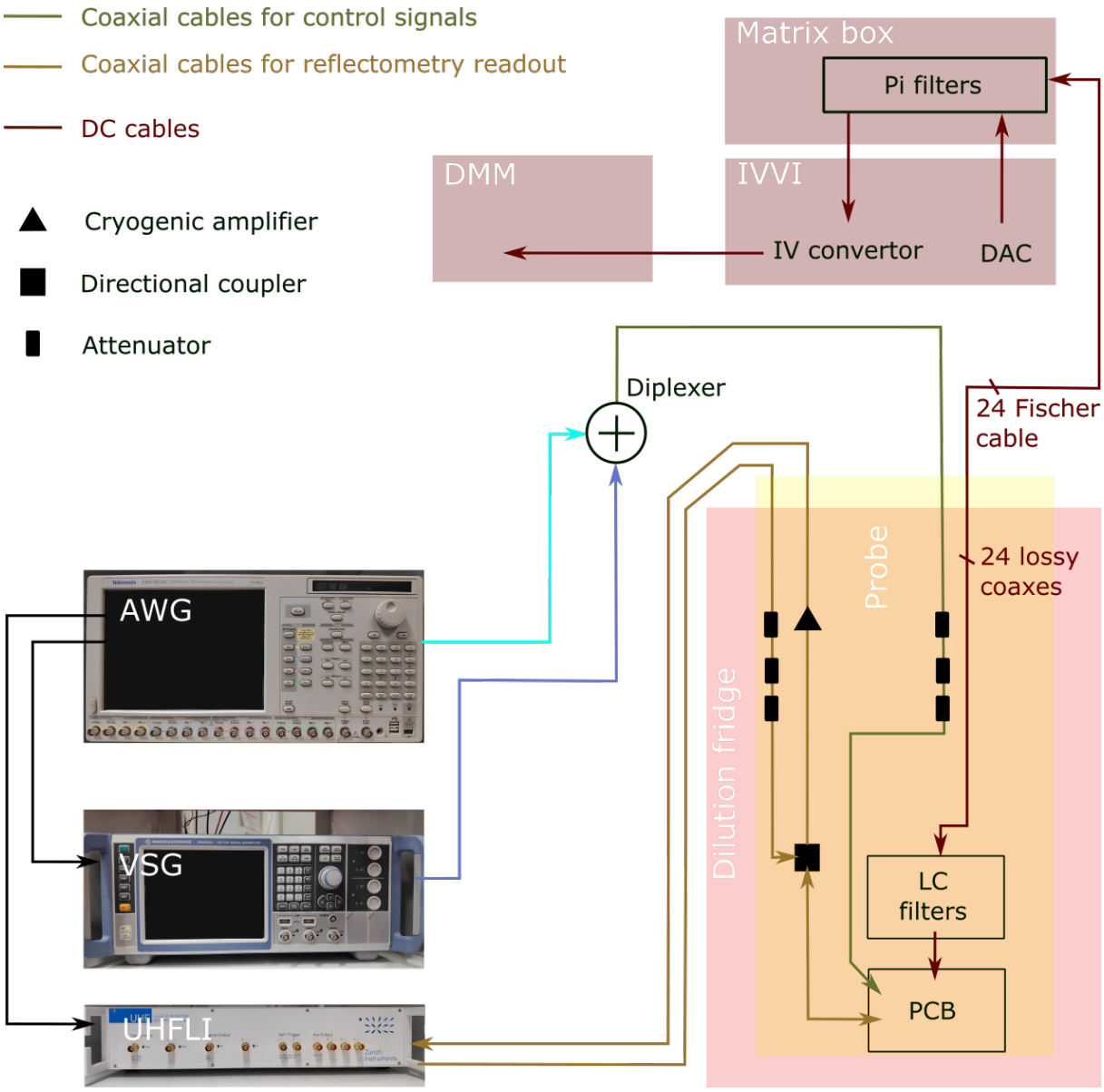


Figure 4.2: **Schematic of the full setup used in the majority of the experiments described in this thesis.** Two divisions can be used. Room temperature (RT) outside of the dilution refrigerator/low temperature (LT) inside the dilution refrigerator and HF/LF (low frequency) circuit. All LT parts are positioned in the dilution fridge insert (probe), indicated by the yellow rectangle. LF signals are shown by red lines. At RT those are guided via Fischer cables, at LT via lossy coaxial (coax) cables which act as a low-pass filter for high frequencies. The HF circuit is subdivided into the control (green lines) and the reflectometry readout part (yellow lines). All HF lines guiding signals towards the printed circuit board (PCB) are attenuated at LT, while the signal reflected from a measured sample gets LT amplified. More about the attenuator configuration can be found in Section 4.1.1. The diplexer (Marki Microwave DPXN-3 or DPXN-0508) allows sending two different control signals via a single line at LT.

to which the PCB bonding pad is bonded to. The LF signals are further guided via 24 wires organized in a shielded wiring harness called Fischer cable at RT and via lossy coaxes at LT. On the way towards the PCB, those signals go through several low-pass filter stages enabling thus a low electron temperature for the measured sample. More about the LF lines filtering can be found in Section 4.1.1. The IVVI and the matrix box are fixed at the fridge top to minimize the length and vibrations of the Fischer cable reducing thus the induced noise. Coming back to the PCB, it acts as a mechanical carrier and provides a platform for electrical connection to the measured sample. An example of a PCB, with the bonding pad layout, can be seen at Figure 4.9a. More about PCBs can be found in Section 4.3. Regarding the control part of the HF circuit, arbitrary waveforms, needed for arbitrary and fast changes in the stability diagram of a qubit, are generated by the AWG. Having four channels with corresponding trigger outputs (markers), the AWG constitutes the backbone of our spin-qubit experiments, driving the qubit and at the same time controlling instruments for the qubit manipulation (VSG) and the readout. The VSG, with the IQ and the pulse modulation options installed, allows a rapid control of the amplitude and the phase of GHz microwave (MW) bursts, down to tens of nanoseconds in length and 80 dB on/off ratio. Since both VSG and AWG output signals need to be sent to one device gate, they are merged by the diplexer. We have chosen to use the diplexer, but a splitter/combiner with a frequency range from DC to more than 10 GHz (e.g. Mini Circuits ZFRSC-183-S+) could in principle be used as well. We have not tested it though. Finally, for the reflectometry readout, from Hz to 600 MHz range, we used the UHFLI. Apart from being a very wide range digital lock-in amplifier, it offers various triggering options and the measured signal representations. More about the reflectometry can be found in Section 4.2. All measurements are performed using the QTlab measurement software.

4.1 Dilution refrigerator

For achieving the millikelvin environment we use a CS81-1400MAG dilution fridge from Leiden Cryogenics, known as ”Grandpa Rudolph” in the lab. It has a base temperature of 20 mK and a 1 mW of cooling power at the mixing chamber (MC) plate. The fridge interior with the inserted probe can be seen in Figure 4.3. To enable the dilution cooling process, a constant temperature is ensured by the pulse tube cooler connected to the 4 K and the 50 K plate (not shown in the Figure 4.3). The fridge is also equipped with a $\sim$100 kg superconducting 9/3 T vector magnet attached to its 4 K plate. Since the thermal mass is huge it takes three to four days to cool down the fridge from RT to the base temperature. Therefore we use the top-loading mechanism which enables the probe to be cooled down in about 20 hours.

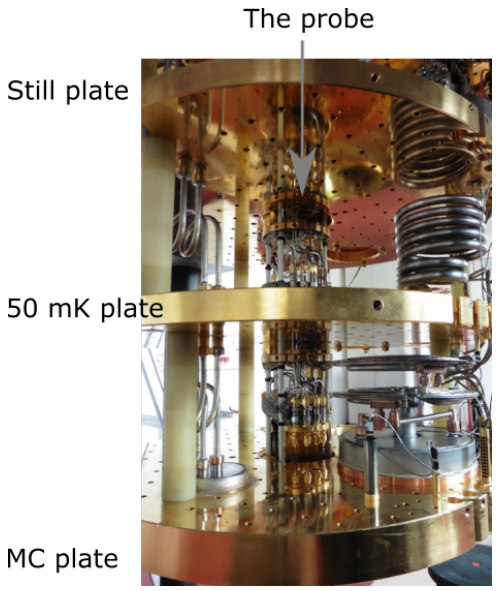


Figure 4.3: **Image showing the interior of the fridge with the probe inserted.** The corresponding probe plates are thermally connected to the fridge ones via the probe clamping mechanism. The probe diameter is 81 mm.

4.1.1 The Probe

As mentioned earlier, the probe allows five times higher sample exchange rate than cooling completely the whole fridge. It consists of five gold-plated copper stages connected together by thermally insulating plexiglass rods, as can be seen at Figure 4.4. Here we also have all coaxial cables, attenuators, filters and the reflectometry circuit installed in it. Apart from the faster sample exchange rate, a possibility for fast repairs is also the advantage of such an approach, which was good during the lab setup stage, but the disadvantage is very limited space and smaller cooling power. Cooling is enabled by the clamping mechanism. Presurizing the clamps, with $\sim$ 25 bar of Helium, thermalizes the probe plates to the fridge ones. Still, there is a finite thermal impedance between the fridge and the probe plates reducing the cooling power in the probe.

Regarding the wiring, the break-out box, on the top of the probe, joins 2X24 DC lines and two 24 pin Fischer connectors and connects 8 coaxial lines to 8 SMA connectors. Each DC line is a lossy coaxial cable acting as a low-pass filter which efficiently cuts the high-frequency noise. Before connecting to the PCB all DC lines undergo a low-pass filtration with LC filters. More about the filtering can be found in Section 4.1.1. The requirement for all parts connecting between two fridge plates is a low thermal conductance, not to heat up lower temperature plates. For electrical connections additional criterion is a relatively good electrical conduction and for high-frequency lines a high bandwidth as well. Accordingly, the coaxial cables 1,2,3,4, installed by the IST workshop, are made of the stainless steel cable UT-085-SS-SS, which is a compromise between the mentioned criteria and the price. The L1 and the L2 are installed by Leiden Cryogenics and they are made out of BeCu/BeCu and BeCu/CuNi respectively. In order to additionally suppress the heat flow from the cryogenic amplifier to the sample, the superconducting cable SC-086/50-NbTi-NbTi was partially used for the A line. Finally, coaxes connecting to the PCB, within the MC, are made of the copper UT-047C cable. Each coaxial cable is attenuated with the attenuator configuration showed in

Figure 4.4. The attenuator values are chosen as a compromise between:

- Lowering the noise temperature at the attenuator's output $T_{out} = \frac{T_{in}}{L} + \frac{L-1}{L} T_{ambient}$, where T_{in} is the noise temperature at the respective attenuator input, L is the attenuation and $T_{ambient}$ is the ambient temperature of the attenuator.

- Attenuating as little as possible while still allowing sufficiently large voltage amplitudes to our samples.

- Dissipating less heat than the cooling power of the respective probe plate. The dissipated power is $P_{dis} = P_{in} - P_{trans} = P_{in} - \frac{P_{in}}{L} = P_{in}(1 - \frac{1}{L})$, where P_{in} is the input noise power and P_{trans} is the transmitted noise power on the respective attenuator's output.

- Availability of attenuators.

A few possible combinations satisfy all the above conditions and the chosen one is shown in Figure 4.4. The probe carries the circuit for the reflectometry readout as well. It consists of the directional coupler, cryogenic amplifier and corresponding coaxial cables. More info about the reflectometry circuit can be found in Section 4.2.

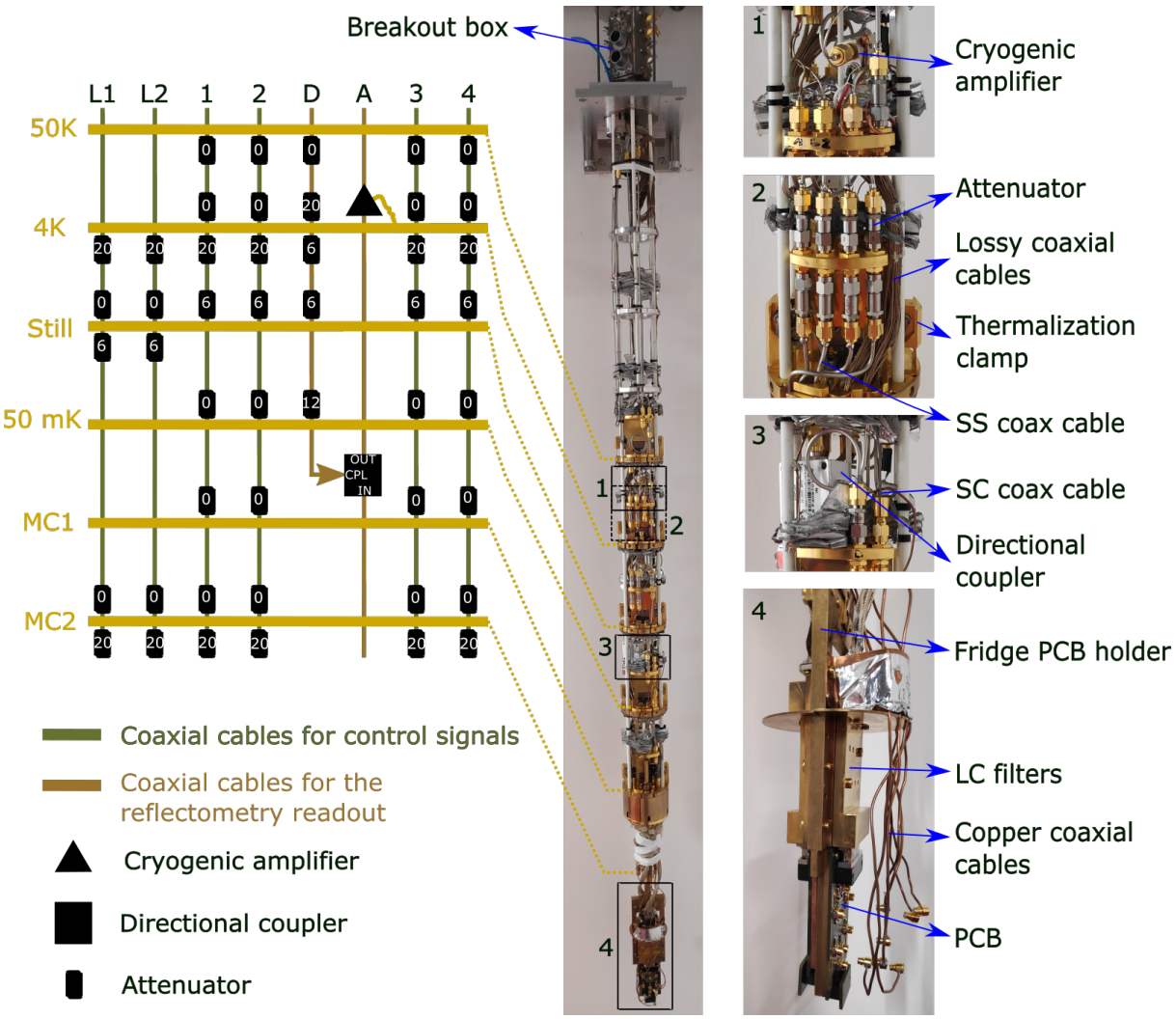


Figure 4.4: **The probe with the attenuator configuration.** The attenuator configuration is shown on the left. *The qubit measurements were performed with different (not optimized) attenuator configuration.* The white number inside attenuators indicates their attenuation. Numbers 1,2,3,4 indicate coaxial cables installed by the IST workshop and, L1 and L2 the coaxial cables installed by Leiden Cryogenics. D stands for the directional coupler branch and A for the amplifier branch. The horizontal yellow lines represent the probe plates, connected with dashed lines to the corresponding plates shown in the middle. Zoom-ins to probe parts are shown on the right. The numbers correspond to those in the middle image. The cryogenic amplifier is thermalized to the 4 K plate with the copper braid. SS stands for stainless steel and SC for superconducting material.

Filtering

One of the pre-requisites to access single energy levels of holes and electrons is a low electron temperature. Electrical noise arriving to the sample increases it. Therefore, DC lines need to be low-pass filtered in order to reduce the amount of the electrical noise coming from the room temperature electronics and cables. An ideal low-pass filter is transparent until a certain frequency after which it abruptly blocks higher frequencies. In reality low-pass filters do not cut abruptly, but have a finite slope, have a finite transparency in the blocking range and lose their filtering behaviour after a high enough frequency. Filters differ in those parameters and a proper combination can approach to the ideal one.

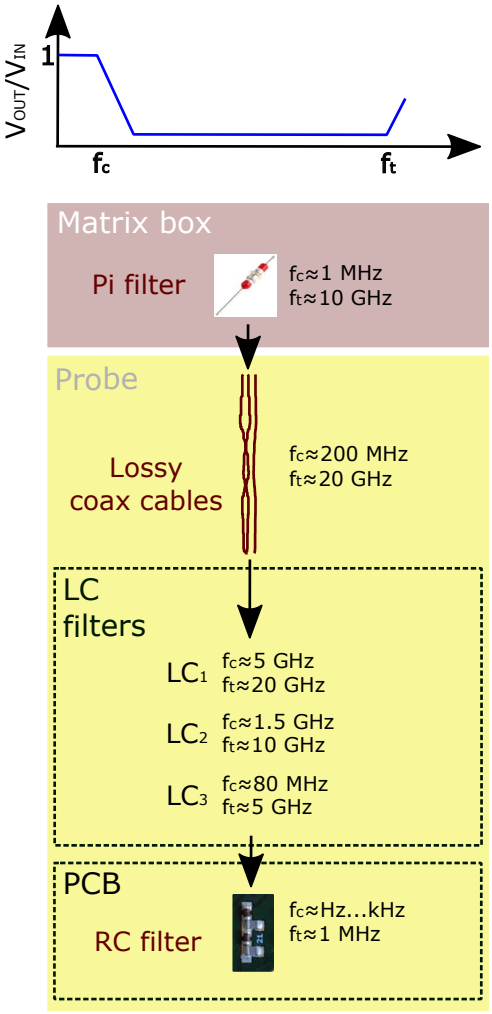


Figure 4.5: **Low-pass filter configuration.** The upper graph shows an oversimplified low-pass filter amplitude vs frequency response introducing f_c and f_t. f_c stands for the cutoff frequency and f_t for the frequency at which the low-pass filter losses its filtering behaviour. The filter sequence starts with Pi fiters, which can be found at RS components under number 239-214. The Pi filter schematic is an inductor sandwitched between two capacitors to ground which reminds of the letter "π". The sequence continues with lossy coaxes and then with LC filters, mounted on the mixing chamber.

A low f_c and f_t in tens of GHz are desired filter parameters. These two oppose each other because a low-pass filter with a lower f_c typically has a lower f_t as well. This can be solved by using a series of filters, combined in a way that the combined frequency response has the lowest f_c and the highest f_t of all the filters in the series. Filtering starts at room temperature with Pi filters integrated in the matrix box as shown in Fig-

ure 4.5. In order to cut very-high-frequency noise, 67 Ω coaxial cables called "lossy coaxial cables" are used for the DC wires in the probe. They have high $f_t > 20\,GHz$ and $f_c \approx 100\,MHz$. To limit the noise bandwidth from higher temperature stages to 80 MHz, additional three stages of LC filters are positioned at the MC plate just before the PCB. Since the voltage sweep speed at our samples is quite low (typically much less than 1 kHz) we can afford a really low noise bandwidth so additional RC filters are implemented at the sample PCB. Their implementation differs from PCB to PCB and some examples can be seen in Figures 4.9, 4.10 and 4.12. More about RC filters can be found in Section A.1.2. Except for RC filters, for all the other filter stages the datasheet behaviour is taken for granted. To evaluate the probe filtering, the effective electron temperature has been estimated to be from 40 to 100 mK, from co-tunneling measurements.

4.2 Reflectometry

The readout technique which senses a device impedance change through the reflected wave amplitude and phase change is called reflectometry. As shown in Figure 4.6, typically an RF sinusoidal wave of amplitude A_{in} is sent towards the measured device. Changes in the device impedance Z modify the reflection coefficient (Γ) according to

$$\Gamma = \frac{Z - Z_0}{Z + Z_0} \tag{4.1}$$

where the $Z_0 = 50\Omega$ is the characteristic impedance of the coaxial cables. Consequential changes of the amplitude and the phase of the reflected wave $A_r = A_{in}\Gamma$ are measured with the lock-in technique. From Figure 4.7b we can see that the highest sensitivity ($\frac{\Delta\Gamma}{\Delta Z}$) takes place for Z smaller than Z_0. Since the impedance of our devices are typically much higher than Z_0, we use a LC matching circuit in order to reduce the resulting impedance and increase the sensitivity. A simplified schematic of the matching circuit and the measured device can be seen at the bottom right of Figure 4.6. Since

the changes of Γ are typically very small the reflected signal needs to be amplified at low temperatures where the noise is still relatively small, to preserve the SNR.

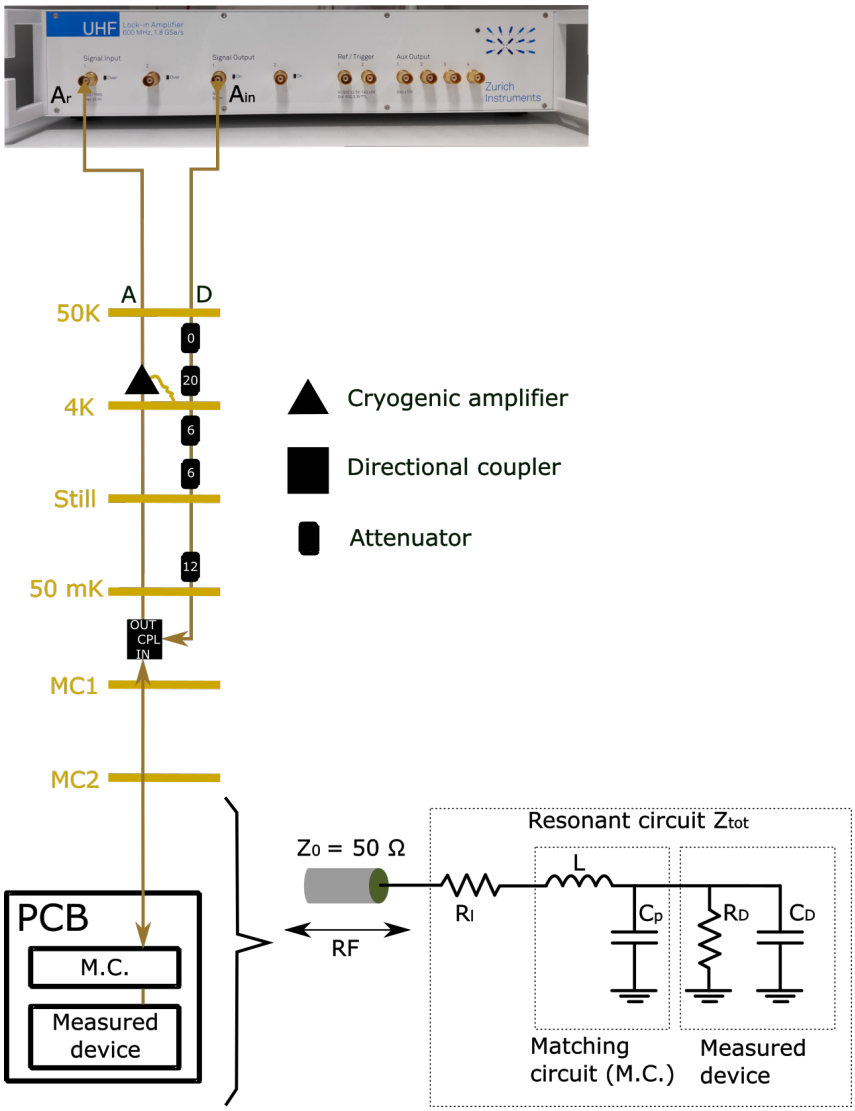


Figure 4.6: **Schematic of the reflectometry in the probe.** The excitation signal, with the amplitude A_{in}, is sent from the UHFLI output to the CPL port of the directional coupler where it couples towards the resonant circuit. Part of it A_r reflects from the resonant circuit and gets amplified by the cryogenic amplifier after which it enters the UHFLI input port and gets measured. In the lower right schematic, the measured device is electrically represented as a parallel combination of the capacitance C_D and the resistance R_D. The matching circuit consists of the inductor L and the parasitic capacitance to ground C_p. Combination of the matching circuit and the device is called resonant circuit with a total impedance Z_{tot}. R_l represent ohmic losses, mainly in the inductor.

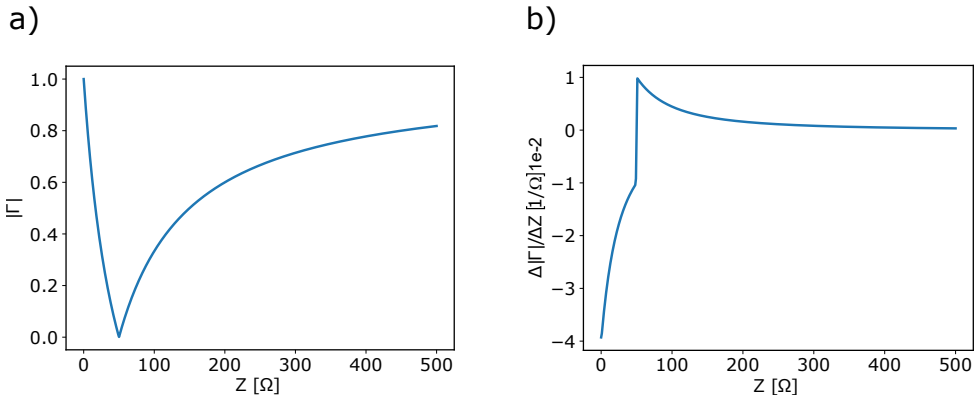


Figure 4.7: **Amplitude of the reflection coefficient and its change versus the impedance. a** $|\Gamma|$ versus the real valued Z going from 0 to $500\,\Omega$, for $Z_0 = 50\,\Omega$. $Z = Z_0$ results in a zero reflection, while for a short ($Z = 0$) a signal gets fully reflected because $|\Gamma| = 1$. **b** Plot showing the numerical derivative $\frac{\Delta|\Gamma|}{\Delta Z}$, which represents the sensitivity of $|\Gamma|$ to changes in Z. The sensitivity increases for lower Z values.

How does the amplification preserve the SNR The S_{md} in Figure 4.8 gets amplified by all the three amplifiers resulting in the output signal $S_O = S_{md}G_1G_2G_3$.

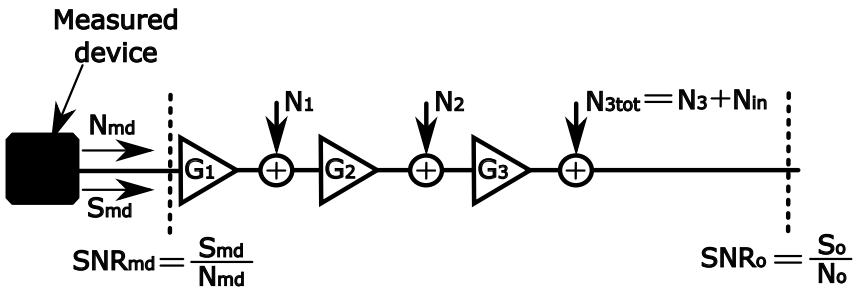


Figure 4.8: **Schematic of the exemplary amplifier chain.** The measured device (md) outputs a signal of power S_{md} and noise of power N_{md} whose ratio yields the signal to noise ratio of the measured device SNR_{md}. N_1, N_2 and N_3 are noise powers generated by the respective amplifiers as seen at their outputs, called output referred noise. G_1, G_2 and G_3 are amplifications of the first, the second and the third amplifier, respectively. N_{in} represents the input noise of a measuring instrument, which comes after the amplifier chain, consisting of the thermal noise of the input resistance and other noise sources. Since N_{in} and N_3 appear at the same point of the circuit, N_{3tot} defines as the sum of these two. The ratio of the output signal power S_O and the output noise power N_O is the signal to noise ratio at the output SNR_O.

Meanwhile, the output noise power has four parts:

- The noise of the measured device amplified by the whole amplifier chain: $N_{md}G_1G_2G_3$
- The N_1 amplified by the second and the third amplifier: $N_1G_2G_3$
- The N_2 amplified by the third amplifier: N_2G_3
- The N_{3tot}

which sums up to the total noise power at the amplifier chain output:

$$N_O = N_{md}G_1G_2G_3 + N_1G_2G_3 + N_2G_3 + N_{3tot} \tag{4.2}$$

Therefore, the output SNR is:

$$SNR_O = \frac{S_O}{N_O} = \frac{S_{md}G_1G_2G_3}{N_{md}G_1G_2G_3 + N_1G_2G_3 + N_2G_3 + N_{3tot}} \tag{4.3}$$

Dividing both the numerator and the denominator in Equation 4.3 with the total amplification $G_1G_2G_3$ yields

$$SNR_O = \frac{S_{md}}{N_{md} + \frac{N_1}{G_1} + \frac{N_2}{G_1G_2} + \frac{N_{3tot}}{G_1G_2G_3}} \tag{4.4}$$

From Equation 4.4 one can see that the role of the amplifier chain is to achieve $\frac{N_1}{G_1}$, $\frac{N_2}{G_1G_2}$ and $\frac{N_{3tot}}{G_1G_2G_3}$ negligible in comparison to N_{md} and therefore provide $SNR_O \approx SNR_{md}$. The fact that the N_1 gets divided only by the G_1 sets the most stringent criterion for the first amplifier in the chain. its output referred noise N_1 should be as low as possible while having large amplification G_1 to achieve the condition $\frac{N_1}{G_1} << N_{md}$. Having this, it is typically easy to achieve $\frac{N_2}{G_1G_2} + \frac{N_{3tot}}{G_1G_2G_3} << N_{md}$ by using standard, off-the-shelf, low noise amplifiers as other amplifiers in the chain. One might ask what would happen if the amplifiers are left out. In that case the output SNR would be:

$$SNR_O = \frac{S_{md}}{N_{md} + N_{in}} \tag{4.5}$$

N_{in} is typically much larger than N_{md}, especially if the measured device is at very low temperature while the measuring equipment is at room temperature. Therefore, without amplifiers, the SNR_O would be much smaller than SNR_{md} and the necessity of the amplifier is obvious. The majority of the considerations in this paragraph are taken from [1].

Now let's consider the amplification in the described reflectometry setup in Figure 4.6. Only one amplifier is used here and it is CITLF3[2], a model designed and fabricated by Cosmic Microwave Technology, Inc. Due to the power dissipation in tens of mW, it is positioned at the 4K plate in the probe, which is the lowest temperature plate that can sustain such a dissipation. In spite of being one of the best known semiconductor amplifiers at the market, its $\frac{N_1}{G_1}$, in Equation 4.4, is typically still higher than N_{md}. Therefore the amplifier noise limits the output SNR in this case, leaving thus room for an improvement in terms of using amplifiers with lower output referred noise power, e.g SQUID (superconducting quantum interference device) or JPA (Josephson parametric amplifier) amplifiers. Before the amplifier, the reflected signal needs to be separated from the signal sent to the device which is achieved by using a directional coupler. The directional coupler needed to be replaced a couple of times due to breaking, but the currently used ZFDC-20-50-S+ seems to be good. It is also the best in terms of the directivity (the most important parameter), amongst the ones we looked into, but it is bulky.

It is important to note that in reality the inductor losses and its stray capacitance might play a more important role, but for understanding the physical principle, the matching circuit schematic in Figure 4.6 contains all relevant parameters.

How does the matching circuit work The equations below are taken from the supplementary of [Frake *et al.*, 2015]. As can be seen in Figure 4.6, the resonant circuit consists of the device parameters R_D and C_D connected in parallel to the parasitic

[1] https://en.wikipedia.org/wiki/Friis_formulas_for_noise

[2] https://www.cosmicmicrowavetechnology.com/citlf3

capacitance C_p and this combination is then connected in series to the inductor L and the wiring resistance R_l. The expression for the total impedance of the resonant circuit Z_{tot} then looks like:

$$Z_{tot} = R_l + i\omega L + R_D||(C_D + C_p) \tag{4.6}$$

Expanding the expression above and separating the real and imaginary part, produces the following expression:

$$Z_{tot} = [R_l + \frac{R_D}{1 + (\omega C_{tot} R_D)^2}] + i\omega[L - \frac{C_{tot} R_D^2}{1 + (\omega C_{tot} R_D)^2}] \tag{4.7}$$

where the $C_{tot} = C_p + C_D$. As $\omega C_{tot} R_D >> 1$ (because typically $\omega > 2\pi 100\, MHz$, C_{tot} is around 1 pF and $R_D > 100\, k\Omega$) the expression (4.7) gets simplified to:

$$Z_{tot} = R_l + \frac{1}{(\omega C_{tot})^2 R_D} + i\omega L - \frac{i}{\omega^2 C_{tot}} \tag{4.8}$$

At resonance the imaginary part vanishes, as can be seen by substituting ω with the resonant frequency $\omega_0 = \frac{1}{\sqrt{LC_{tot}}}$:

$$Z_{tot,res} = R_l + \frac{L}{C_{tot} R_D} = R_{eff} \tag{4.9}$$

where res in $Z_{tot,res}$ marks the resonant case and $R_{eff} = R_l + \frac{L}{C_{tot} R_D}$ is the effective resistance on resonance. So, taking into account the typical values for L $\approx 1\,\mu H$, $C_{tot} \approx 1\, pF$, $R_D > 100\, k\Omega$ and R_l of a few ohms yields $R_{eff} < 20\,\Omega$ positioning thus the $Z_{tot,res}$ in the sensitive part of the graph on Figure 4.7b. This is how the matching circuit "matches" or, maybe better to say, reduces a large device resistance.

Sensitivity Now let's see which factors influence the sensitivity of Γ to changes of C_D and R_D. Since the typical measured values are the phase Γ_ϕ and the amplitude component $|\Gamma|$, let's calculate sensitivities $\frac{\delta\Gamma_\phi}{\delta C_D}$, $\frac{\delta\Gamma_\phi}{\delta R_D}$, $\frac{\delta|\Gamma|}{\delta C_D}$, $\frac{\delta|\Gamma|}{\delta R_D}$. Firstly, the real and the imaginary component of the reflection coefficient need to be separated as:

$$\Gamma = \frac{Z - Z_0}{Z + Z_0} = \frac{Z_r^2 + Z_i^2 - Z_0^2 + 2iZ_0Z_i}{(Z_r + Z_0)^2 + Z_i^2} \tag{4.10}$$

where Z_r is the real and Z_i is the imaginary component of a circuit impedance. Now, the amplitude $|\Gamma|$ and the phase Γ_ϕ of the reflection coefficient can be calculated:

$$\Gamma_\phi = arctan\frac{2Z_0Z_i}{|Z|^2 - Z_0} \tag{4.11}$$

$$|\Gamma| = \frac{\sqrt{(Z_r^2 + Z_i^2 - Z_0^2)^2 + (2Z_0Z_i)^2}}{(Z_r + Z_0)^2 + Z_i^2} \tag{4.12}$$

Substituting Z_r and Z_i, in Equation 4.11, with the real and the imaginary components of Z_{tot}, from Equation 4.8, and by calculating a partial derivative of Γ_ϕ in respect to C_D, the phase sensitivity $\frac{\delta\Gamma_\phi}{\delta C_D}$ can be obtained. After substituting the resonant condition $\omega = \omega_0$, we get:

$$\frac{\delta\Gamma_\phi}{\delta C_D}|_{\omega=\omega_0} = \frac{2\sqrt{\frac{L}{C_{tot}}}Z_0}{C_{tot}(R_{eff} + Z_0)(R_{eff} - Z_0)} \tag{4.13}$$

For such a circuit, the quality factor can be calculated as $Q = \frac{\omega L}{R_s}$[3], where $R_s = R_{eff} + Z_0$ is the circuit series resistance. By substituting ω with ω_0 the quality factor reads as $Q = \frac{\sqrt{\frac{L}{C_{tot}}}}{R_{eff}+Z_0}$ which can be further substituted into Equation 4.13:

$$\frac{\delta\Gamma_\phi}{\delta C_D}|_{\omega=\omega_0} = \frac{2QZ_0}{C_{tot}(R_{eff} - Z_0)} \tag{4.14}$$

The sensitivity of Γ_ϕ in respect to R_D is negligible for large R_D and the already made assumption $\omega C_{tot} R_D >> 1$ results in $\frac{\delta\Gamma_\phi}{\delta R_D}|_{\omega=\omega_0} = 0$. The expression $\frac{\delta\Gamma_\phi}{\delta R_D}$, prior to the substitution of ω with ω_0, is very long and therefore not shown.

[3] http://ve2azx.net/technical/QEXaudet-Rev1.pdf

Similarly, upon substitution of the the real and imaginary components of Z_{tot} from Equation 4.8 into Equation 4.12 and after calculating partial derivatives of $|\Gamma|$ in respect to R_D and C_D the corresponding sensitivities read as:

$$\frac{\delta|\Gamma|}{\delta R_D}|_{\omega=\omega_0} = \frac{2Z_0L}{C_{tot}(R_{eff}+Z_0)^2R_D^2} = \frac{2Z_0Q^2}{R_D^2} \tag{4.15}$$

$$\frac{\delta|\Gamma|}{\delta C_D}|_{\omega=\omega_0} = \frac{-2Z_0L}{C_{tot}^2(R_{eff}+Z_0)^2R_D} = \frac{-2Z_0Q^2}{C_{tot}R_D} \tag{4.16}$$

For the later discussion it is useful to make a distinction between the **ohmic reflectometry** where changes in R_D are mainly sensed and the **gate reflectometry** where changes in C_D are mainly sensed. The general conclusion is that all the sensitivities can be boosted by increasing the Q factor and decreasing the total capacitance $C_{tot} \approx C_p$. From Equation (4.15) it is also clear that for the ohmic reflectometry smaller device resistance gives better sensitivity.

Boosting the sensitivity of the reflectometry As said above, the reflectometry sensitivity can be increased by reducing the parasitic capacitance towards ground C_p and by increasing the Q factor. The parasitic capacitance is reduced by engineering the HF PCB layout and more about this can be found in Section 4.3.2. Regarding the matching circuit inductor, there are two common approaches. One is to use an SMD (surface mounted device) copper inductor which limits the Q factor of the circuit with its own low Q factor, to below 100. The exact value can be found in the inductor datasheet. Higher Q factors can be obtained with superconducting planar inductors because they have smaller losses. More info about superconducting planar inductors, which we fabricated out of a NbTiN film on a Si chip, can be found in Section A.1. It is worth to mention **another loss source**, namely losses in the dielectric, which are not shown in the schematic in Figure 4.6, but could be represented as an equivalent resistance in parallel to the measured device. These are typically consisted of the PCB dielectric losses, seen by the electric field (reflectometry excitation signal) running through the

PCB HF lines and losses in the dielectric of the measured sample. They highly depend on the geometry of the PCB HF lines and the sample as well as on the material used for the PCB dielectric and the sample material. In some cases their value can be in tens of $k\Omega$ [Zalba *et al.*, 2015], thus smaller than the sample resistance R_D, reducing thus the circuit Q factor and the reflectometry sensitivity. The dielectric losses are taken into account in Chapter 6.

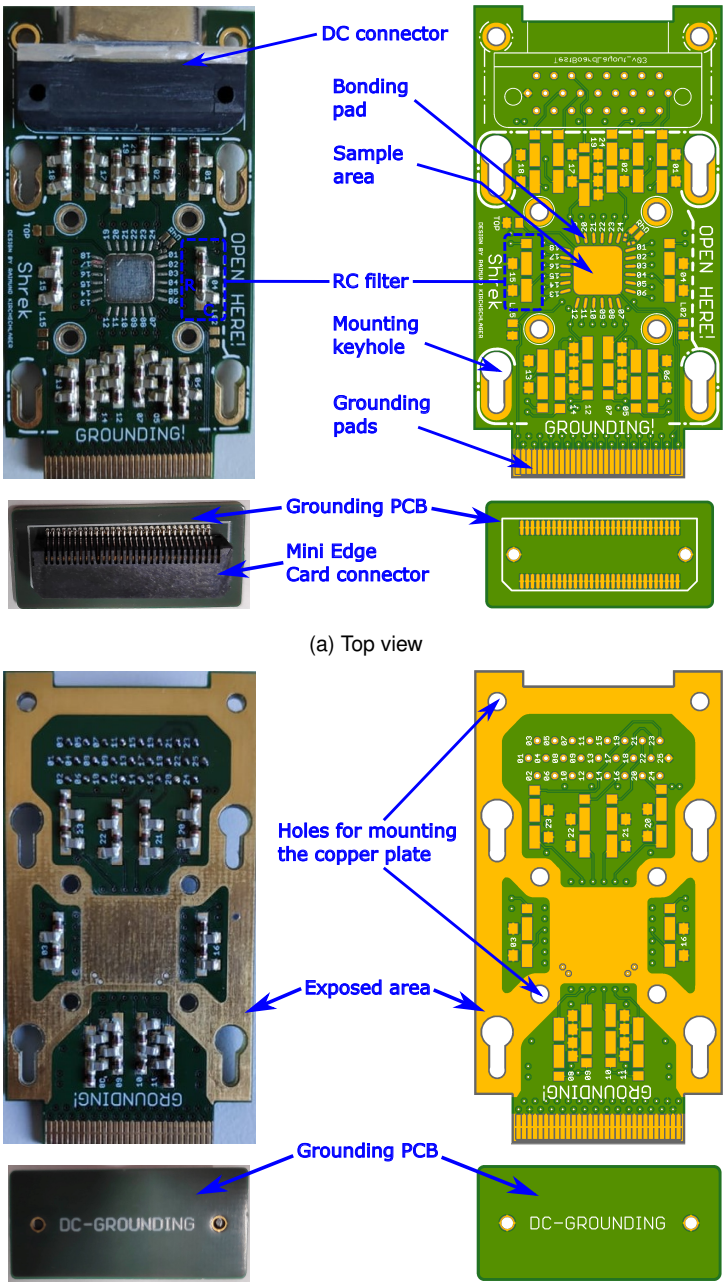
General approach for calculating the sensitivity In case the resonant circuit schematic differs from the one presented above (e.g. inductor is in parallel instead of in series to the sample) then the reflection coefficient sensitivity in respect to a sensed quantity can be calculated by the following approach. First calculate the total impedance Z_{tot} of the resonant circuit, as seen from the coaxial cable and split it into the real Z_r and the imaginary part Z_i. Next, substitute Z_r and Z_i in Equations 4.11 and 4.12. Finally, calculate the partial derivatives of resulting $|\Gamma|$ and Γ_ϕ in respect to the sensed quantity and afterwards substitute ω with the resonant frequency ω_0 which formula depends on the resonant circuit schematic. The partial derivative represents the sensitivity.

4.3 Printed circuit boards

The initial PCBs contained lines only for LF transport measurements (DC PCB). Since spin dynamics experiments require high-frequency signals, we have upgraded the DC PCB design with high bandwidth HF lines. Additionally, four RF lines with an integrated matching circuit were added for the reflectometry readout. In Figures 4.9, 4.10 and 4.12 one PCB from each family is shown. Different PCBs, from the same family, have different components soldered to them. The component values of all the PCBs mentioned in this chapter can be found in Table A.1. All the boards are designed in Eagle CAD.

4.3.1 DC PCB

As an example of a DC PCB, the PCB named ”Shrek” is shown in Figure 4.9. It is 67 mm long and 36 mm wide and consists of four copper layers with FR-4 as the dielectric in between them. It fits in liquid helium dipsticks for 4 K measurements, in the Oxford Heliox for 250 mK measurements and in the Grandpa Rudolph fridge. Electrical connections start with the 25-pin DC connector of a micro D type (M83513/13-D01NN) after which they are routed as $125\,\mu m$ (minimum width the PCB manufacturer ”Beta Layout” can provide) copper traces. On the way towards the bonding pads and the grounding part, each line is low-pass filtered with a two stage RC low-pass filter. From the PCB side, the grounding part consists of an exposed raster of copper strips which act as grounding pads. From the other side, the Mini Edge Card connector shortens all DC lines to the ground plane of the board, when plugged. Therefore all the bonding pads are kept at the same potential, protecting thus the a sample from electrostatic discharges. It is worth mentioning that the surface finish technique is ENIG (electroless nickel gold), but in our measurements we did not see the influence of the ferromagnetic nickel, presumably due to its low thickness of $4 - 8\,\mu m$. The used micro-D connector is slightly magnetic too.



(a) Top view

(b) Bottom view

Figure 4.9: **DC PCB named "Shrek".** The pictures of one PCB from the Shrek family (designed by Raimund Kirchschlager) are shown on the left. The corresponding layouts are shown on the right. The top layer is shown in **a** and the bottom layer is shown in **b**. DC lines start with micro-D 25 pin DC connector. They are routed towards the two stage low-pass RC filters and the grounding pads in parallel. The ones passing the RC filters finish at bonding pads numbered from 1 to 24 around the sample area. The grounding PCB with soldered Mini Edge Card connector is shown at the bottom. It shortens all the DC lines to ground, when plugged to the grounding pads of the PCB. Regarding the PCB placement, keyholes allow a slide-in mounting of the PCB to the probe. Holes for mounting the copper plate enable additional height-adjusting copper plate to be fixed on the bottom side of the PCB. Exposed golden area on the bottom side makes the thermal and electrical contact between the copper plate and the PCB.

4.3.2 HF PCB

Why do we need a HF PCB For controlling a spin qubit, microwave electrical signals and control pulses with a nanosecond rise time need to be applied to the DQD gates. Therefore, the lines guiding microwaves and control pulses need to have a bandwidth on the order of GHz. These lines we call fast gate lines, because they guide the HF signal towards the gates. RF lines are needed for the qubit state readout via the reflectometry technique, as well. In both cases, going from RT down to the PCB those are coaxial cables as explained in Section 4.1.1. These coaxial cables finish in a male type SMP (sub-miniature push-on) connector (19K202-271L5). They plug into female type SMP (19S141-40ML5), soldered on the PCB, after which the signal continues through PCB HF traces.

PCB HF traces We use two different types of electrical planar transmission lines for HF traces: micro strips (Figure 4.10) and co-planar wave guides (Figure 4.12). Micro strip consists of a copper strip separated by the dielectric from the ground plane beneath. In a first approximation, the characteristic impedance of the micro strip depends on the dielectric thickness, its permittivity and the strip width. It is easier to implement, but it has more radiation losses meaning more coupling towards other lines on the PCB. On the other hand, co-planar wave guides are more shielded with ground planes. Their characteristic impedance additionally also depends on the separation of the strip and the ground planes alongside it. To compensate the increase of the characteristic capacitance, it requires a thicker dielectric beneath for the same characteristic impedance, which, in combination with other requirements (e.g.: strip width determined by the bias tee capacitor width), sometimes exceeds the standard fabrication parameters of PCB manufacturers, increasing thus the PCB price. For the dielectric, we decided to use FR-4 in all of our PCBs, despite its higher loss tangent in comparison to e.g. Rogers laminates, because it is standard for Beta Layout PCB manufacturer. In the early stage experiments these losses are anyhow expected to be negligible in

comparison to e.g. reflective losses caused by the impedance discontinuity due to Aluminium bonding wires.

Design constraints Moving towards the final version, several intermediate versions of HF PCBs were fabricated. The tendency of such a trial and error route was the optimization in terms of uniformity of the HF lines ($50\,\Omega$ matching), low crosstalk between the HF lines themselves and towards the DC lines, more accessible layout, more sensitive reflectometry readout and the compatibility with a wider range of samples and experiments. The parameters that oppose each other the most are the low crosstalk and the HF line uniformity on one side and the sensitive reflectometry on the other side. The low crosstalk requires more ground planes, especially around HF traces, such that the irradiated electric field goes towards ground. On the contrary, increasing the reflectometry sensitivity requires the reduction of the parasitic capacitance towards the ground, as explained in Section 4.2. The contradiction between those parameters resulted in two ”optimized” HF PCB versions instead of a single one. Chronologically the first one was Iron Man. The focus here was on reducing the parasitic capacitance towards I2 inductor ports (consult Figure 4.10b). Since this was the first version, naturally it had some suboptimal choices which we tried to correct in the next PCB design. The second version, named Iron Kid, is shown at Figure 4.12. its was steered a bit more towards reducing the crosstalk between fast gates and between fast gates and DC lines.

Similarities between Iron Man and Iron Kid Both of them have six layers in order to decouple the HF and the DC part. Layout of all layers for Iron Man can be seen in Figure 4.11 and for Iron Kid in Figure 4.13. The top and the bottom layers are mixed HF and DC layers, while the two middle ones (the third and the fourth) are DC layers. Ground layers, two and five, shield the two middle DC layers from the HF signals and provide an HF ground for HF traces on the top and the bottom layer. The top layer is used mainly for the six HF traces for fast gates. Each fast gate trace starts with an SMP then goes through the bias tee to the corresponding fast gate bonding pad. The

bottom layer carries RF traces for the reflectometry. Regarding the DC part, DC lines connecting the DC connector and single stage RC filters reside on the top and the bottom layers because the filters are on these two layers, avoiding thus more signal vias. Even if those DC lines are on the same layer as the HF traces, they are far enough from them so the crosstalk is negligible. We used only vias which are going through all the layers, avoiding buried vias and reducing thus the PCB price. After the RC filters the DC lines are routed, mainly on the DC layers, towards the sample area and towards the grounding pads.

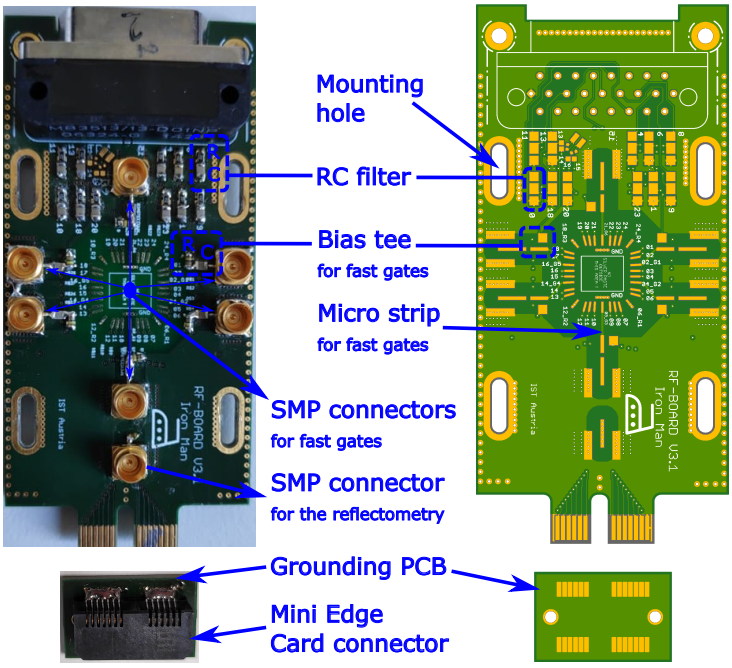
Except a few differences which are described in the corresponding sections, both PCBs have a rather similar **reflectometry** part. The reflectometry RF trace starts with the SMP connector on the top layer. A row of parallel vias, to reduce the parasitic via inductance, guide the reflectometry signal to the bottom layer where it gets splitted into four traces using simple geometrical T splitters. Each trace then connects to the inductor ports I1, while the output ports I2 are with two signal vias connected to the corresponding reflectometry bonding pads on the top layer (consult Figures 4.10b and 4.12b). The inductor forms the matching circuit together with the parasitic capacitance at the port I2 towards the ground. In order to use less coaxial cables and amplifiers in the fridge we exploit the frequency division multiplexing technique by using different inductor values on the same PCB. This allows using one SMP and splitting the RF traces towards each of the four resonant circuits. Since the lumped element reflectometry operates typically below 1 GHz, signal losses due to line bends, width changes and other geometrical line changes are less pronounced. Therefore it is good enough to split the reflectometry RF traces with a simple geometrical T splitter. For the reason of boosting the reflectometry sensitivity, the parasitic capacitance to ground was reduced by removing ground planes around the sample area as can be seen in individual layer layouts in Figures 4.11 and 4.13. Also the inductor SMD footprints, reflectometry bonding pads, DC bonding pads and DC routing have been carefully designed and positioned in order to decrease this parasitic capacitance in both HF PCB designs. So far, similarities between Iron Man and Iron Kid have been explained. In the next paragraphs, the

focus is on their differences.

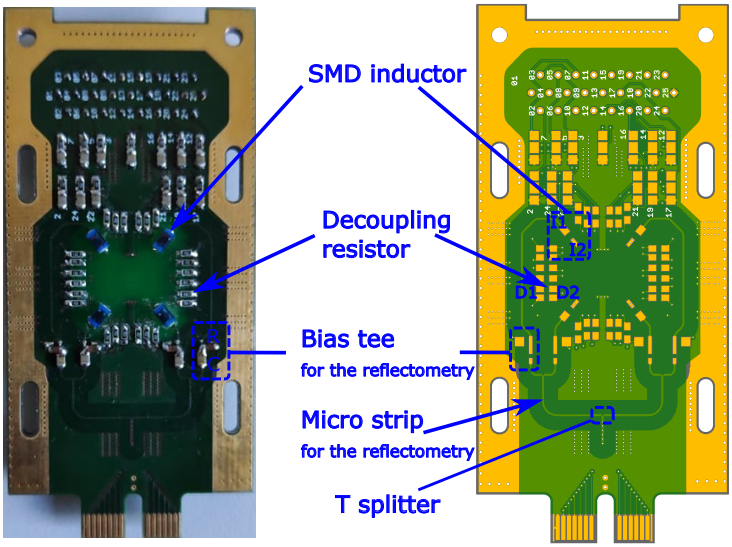
Iron Man

The first optimized HF PCB version was Iron Man, shown in Figure 4.10. It is 77 mm long and 36 mm wide. It is compatible with the Grandpa Rudolph fridge, the Oxford Heliox and the 4 K dipsticks. The layer stackup contains 6 copper layers with FR-4 used as the dielectric in between. The thickness of all the layers follows the standard dimensions of the Beta Layout company and can be seen in Figure 4.11. The obvious difference to Shrek are the seven SMP connectors. Six of them, organized in a hexagon pattern are for fast gates and one for the reflectometry. A micro-strip transmission line type is used here, both for fast gates and the reflectometry traces. The width of all the micro-strips is 0.3 mm which together with the 0.2 mm thickness of the dielectric beneath and the FR-4 dielectric constant $\varepsilon_r = 4.2$ results in the characteristic impedance of $Z_0 \approx 50\,\Omega$.

Decoupling resistors Around the sample area, on the bottom layer, there are SMD footprints for decoupling resistors. Each DC line is connected to a corresponding input port D1 in the ”ground polluted” area and the corresponding DC bonding pad is connected to the output port D2 in the ”ground free” area (consult Figure 4.10b). The resistors decouple D2 from D1 and therefore reduce the capacitance of the corresponding DC bonding pad towards the ground. Because there is a finite capacitance between DC bonding pads and a reflectometry bonding pad, such a measure reduces the parasitic capacitance seen by I2, increasing thus the reflectometry sensitivity. It would have been better to have those resistors on top to avoid vias which couple to nearby ground planes and therefore increase the parasitic capacitance. But, this was not possible due to the SMP connectors and the HF traces whose layout on the top layer is imposed by the fridge sample holder the PCB is mounted to.



(a) Top view



(b) Bottom view

Figure 4.10: **HF PCB named "Iron Man", PCB number 2.** Pictures of the PCB are on the left, while corresponding layouts are shown on the right. The top layer is shown in **a**. The bottom layer is shown in **b**. Every DC line passes through a single stage RC filter with elements R = 1 kΩ and C = 10 nF. Before connecting to the corresponding bonding pad it passes through the decoupling resistor as well, which input and output ports are marked with D1 and D2 respectively. DC bonding pads are numbered from 1 to 24. Fast gate bonding pads are named as XX_GY where XX represents, via the bias tee added DC line, and Y is the fast gate index, going from 1 to 6. Similar nomenclature is used for the reflectometry bonding pads, but G in XX_GY is replaced by R. The bias tees for fast gates have 1.8 MΩ resistor and a capacitor 10 nF capacitor. Bias tees for the reflectometry, on the other hand, have 10 kΩ resistors and the same capacitors. The grounding PCB and the connector are shown at the bottom. The number of grounding pads is reduced to 26.

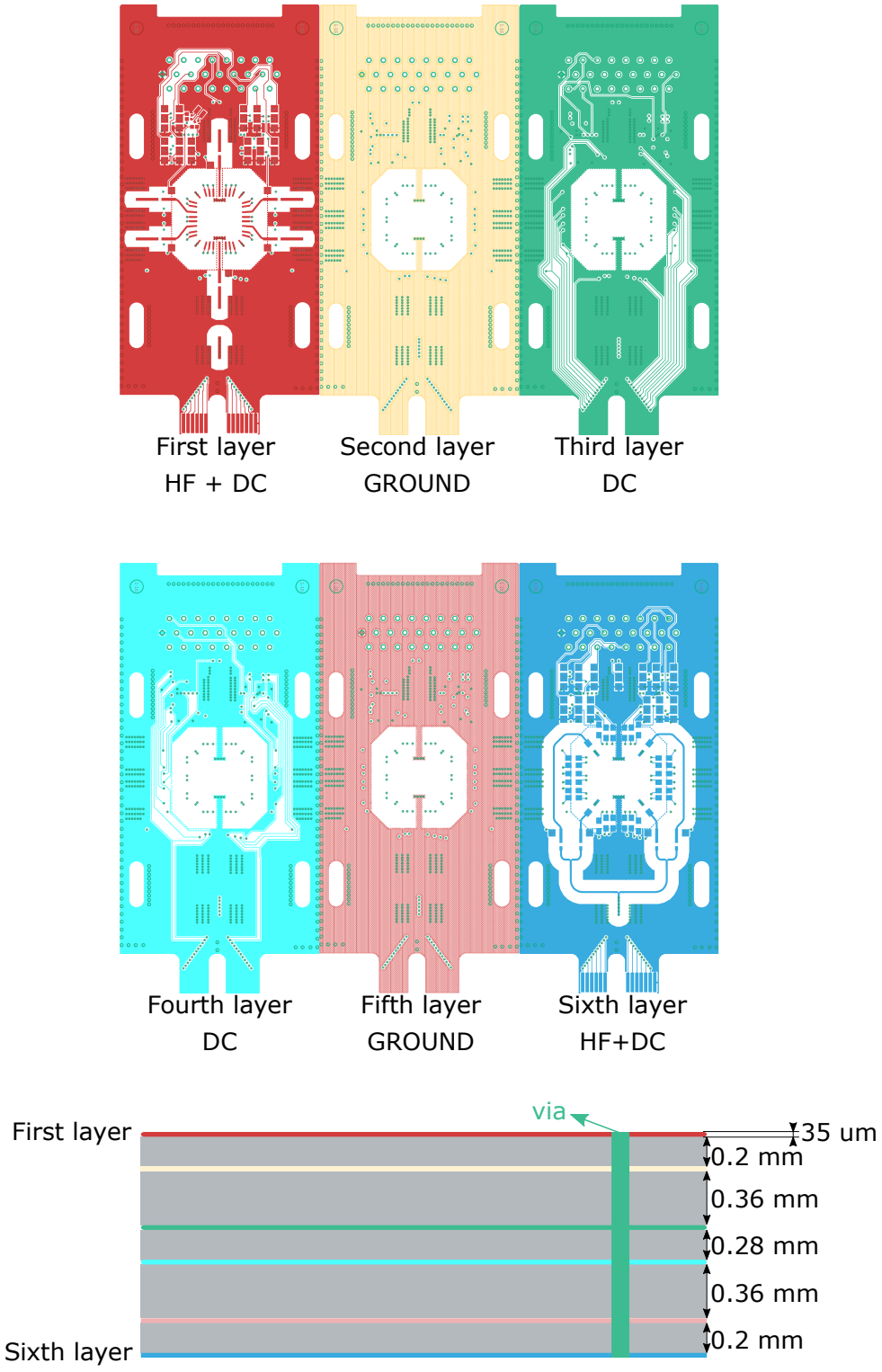


Figure 4.11: **Iron Man PCB layout and layer stackup. Top and middle:** Layout of all Iron Man PCB layers. Each layer is shown in a different color. Green circles represent vias. All filled polygons are ground planes, while the thicker lines represent HF traces and the thinner lines represent DC lines. **Bottom:** Cross-section of the layer stackup. The corresponding layer cross-sections are color matched with the layer layouts shown above. All metal layers are made of $35\,\mu m$ copper, while FR-4 is used for the insulator in between, shown in grey. Signal routing between layers are enabled by vias.

Iron Kid

To create a PCB compatible with the ”Snow White” fridge and for implementing a few changes, which are discussed below, we designed a PCB called Iron Kid, shown in Figure 4.12. It has the same length but a different width of 40 mm and longer, diagonally positioned, mounting holes to be able to install it on the Snow White PCB holder rails. The mounting holes on the opposite diagonal, for mounting the PCB in the Grandpa Rudolph fridge, are changed to keyholes to have the slide-in mount option. Imposed by the Snow White fridge sample holder, everything needed to fit inside a 30 mm wide area on the top layer. Therefore the SMP footprints for the fast gates 02, 04, 14 and 16 are rotated in respect to Iron Kid. In addition, the sample area is widened by approximately 2 mm. Mounting holes for installing a mechanical protecting cap for the sample are added as well. In the light of the crosstalk reduction, the type of all HF traces is **changed to co-planar wave guide** type and each DC bonding pad is connected to the ground in HF terms via the **coupling capacitor**. Other upgrades include **wider HF traces**, **the addition of SMD footprint for varactors**, **and more ground (GND) vias** connecting ground planes on different layers. In the following, reasoning for each of these changes is given.

Co-planar wave guides with a wider signal trace Co-planar wave guides offer better HF shielding against irradiation towards the surrounding space, since the electric field bends mainly towards the ground planes alongside the signal trace. The width of the signal trace itself was increased from 0.3 mm to 0.8 mm to match with the bias tee capacitor width, to achieve a better wave guide transmission. In order to maintain roughly the same characteristic impedance, as in the case of a micro-strip, the dielectric thickness below the top and the bottom layer was increased from 0.2 to 0.4 mm as can be seen in the sketched PCB cross-section in Figure 4.13. Still, the resulting impedance is $40\,\Omega$ instead of $50\,\Omega$ due to the small, 0.2 mm, gap between the signal trace and the ground planes alongside, set like this to increase the shielding effect. This impedance mismatch is expected to be negligible in comparison to the unavoid-

able mismatch due to the bond wires. Considering the crosstalk towards the other lines, for the reflectometry it is probably negligible. its low power $<$-90 dBm does not cause significant shifts in the stability of nearby devices as a high amplitude control pulse does. Also it is a single frequency signal, far away from important energy transitions in our devices. Therefore the gap between the signal trace and the ground planes alongside, on the bottom layer, was kept to 0.5 mm resulting in 50 Ω impedance, matched with coaxial cables. The reported impedances are obtained considering a FR-4 dielectric constant of $\varepsilon_r = 4.2$.

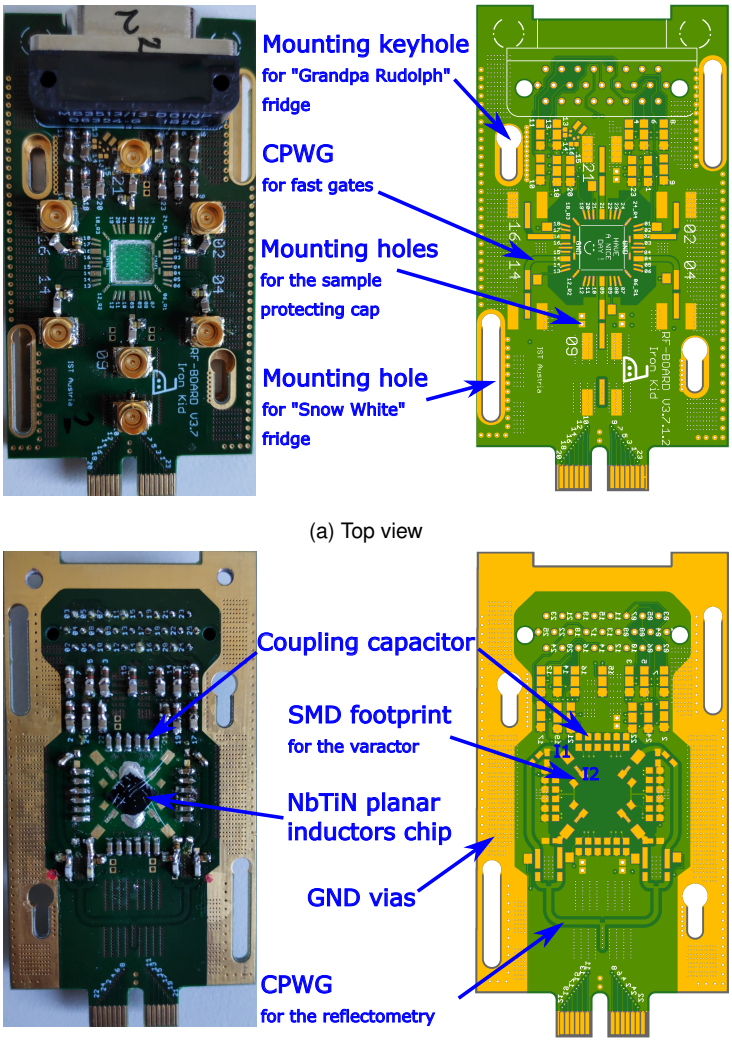
Coupling capacitors Appropriate capacitors decrease the impedance of DC bonding pads towards the ground, flushing thus the parasitically coupled high-frequency signals to the ground and decreasing the crosstalk between fast gates and DC lines. This is exactly opposite to the measure taken on Iron Man PCB, increasing thus slightly the parasitic capacitance seen by the inductor I2 ports (consult Figure 4.12b). Such a crosstalk reduction measure would be good for the experiments involving pulses on several fast gates in parallel.

Varactors Adding varactors between inductor I2 ports and the ground allows to tune the matching condition, which can boost the reflectometry sensitivity. Varactors are diodes whose capacitance, in the reverse biased regime, can be tuned by the voltage applied between its electrodes. A reader might ask the question if a varactor would not increase the total capacitance and therefore decrease the reflectometry sensitivity, as stated above. The answer is yes, but, as can be seen from Equation 4.13, proper R_{eff} value, tuned by the varactor, can result in an even higher sensitivity. However, off-the-shelf varactors have very small tuning range at millikelvin temperature.

More ground vias More ground vias make the ground throughout the PCB more uniform and reduce its impedance.

Sample area As can be seen on the left side in Figure 4.12a, 500 μm were removed below the sample area which corresponds to the typical thickness of our samples.

Having the PCB bonding pads on the same height as the sample bonding pads reduces the bond length. This further reduces the crosstalk amongst fast gates and between the fast gates and the DC lines.



(a) Top view

(b) Bottom view

Figure 4.12: **HF PCB named "Iron Kid", PCB number 2.** Pictures of the PCB are on the left, while corresponding layouts are shown on the right. The top layer is shown in **a**. The bottom layer is shown in **b**. At this particular PCB no SMD inductor was used. We glued the NbTiN planar inductors chip, on the bottom side of the PCB and bonded one planar inductor (or a combination of two) between each of the I1 and I2 port pairs. The bonding pad nomenclature is the same as for Iron Man. The possible varactors at the reflectometry pads R1 and R4 are biased from the DC line 5 and the varactors at the reflectometry pads R2 and R3 are biased from the DC line 15. However, the varactors were not soldered at the PCB shown here. The coupling capacitors for bonding pads 5 and 15 provide the HF ground for the varactors. This PCB has 10 nF coupling capacitors. A better option are 220 pF capacitors as explained in Section A.1. The RC filters consist of R=10 kΩ and C=10 nF, same as on the Shrek PCB shown in Figure 4.9. The bias tees for fast gates are the same as on Iron Man shown in Figure 4.10. The bias tees for the reflectometry consist of a 510 kΩ resistor and a 1.5 nF capacitor. The grounding connector is not shown here since it is identical to the one in Figure 4.10.

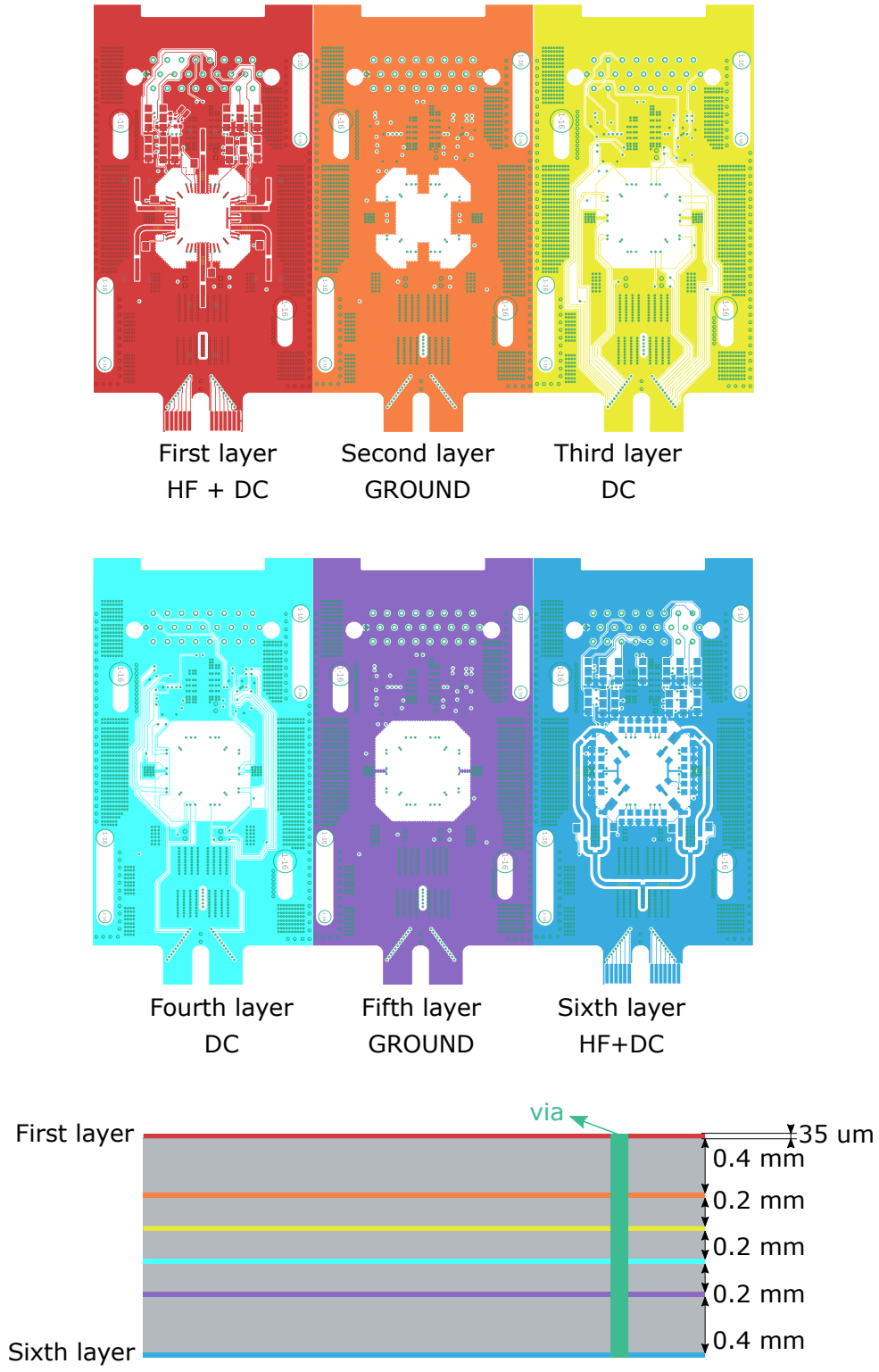


Figure 4.13: **Iron Kid PCB layout and layer stackup. Top and middle:** Layout of all Iron Kid PCB layers. Green circles represent vias. All filled polygons are ground planes, while the thicker lines represent HF traces and the thinner lines represent DC lines. **Bottom:** The cross sectional layer stackup. It is kept symmetric, to avoid possible deformation of the PCB during its fabrication process. The corresponding layer cross sections are color matched with the layer layouts shown above. All metal layers are made of 35 μm copper, while FR-4 is used as insulator in between, shown in grey. Signal routing between layers are enabled by vias.

Conclusion about HF PCBs

As stated above, the goal of Iron Kid was to reduce the crosstalk and to improve some general design aspects of the Iron Man PCB while for Iron Man a smaller parasitic capacitance is expected at inductor I2 ports (the I2 port label is introduced in Figure 4.10b). A measurement of the transmission and the crosstalk can be seen in Figure 4.14. The crosstalk between a fast gate and a DC line is hard to measure, therefore for the general crosstalk benchmark here, the crosstalk between fast gates 2 and 4 on both PCBs is taken. It can be seen that Iron Kid shows a much **lower crosstalk** up to 13 GHz, which is actually the frequency range of interest, proving that the design goal is achieved. Regarding the **transmission**, Iron Kid performs better up to 8 GHz but after this Iron Man has partially higher transmission. It is good to remind that the fast gate characteristic impedance of Iron Kid is 40 Ω and therefore not matched to the 50 Ω coaxial cable impedance which reduces the transmission coefficient. However the lower transmission of fast gates is not a problem as one can increase the power of the HF source and therefore achieve the wanted power on the sample.

Regarding the reflectometry, from the resonant frequencies f_{res} shown in Figure 4.15, parasitic capacitances at inductors I2 ports have been extracted according to the formula $f_{res} = \frac{1}{2\pi\sqrt{LC_p}}$. By comparing their values, written in Table A.1, we see that the parasitic capacitance at 06_R1, 12_R2 and 18_R3 bonding pads are lower for the Iron Man PCB, as expected. On the contrary, the parasitic capacitance at 24_R4 turns out to be slightly lower for the Iron Kid PCB. Since the corresponding inductor has the largest value of the four (1200 nH), by putting down the numbers, it turns out that the observed deviation can be explained by the inductance value, at the two measured PCBs, being at the two opposite maximums allowed by the 5$\%$ tolerance.

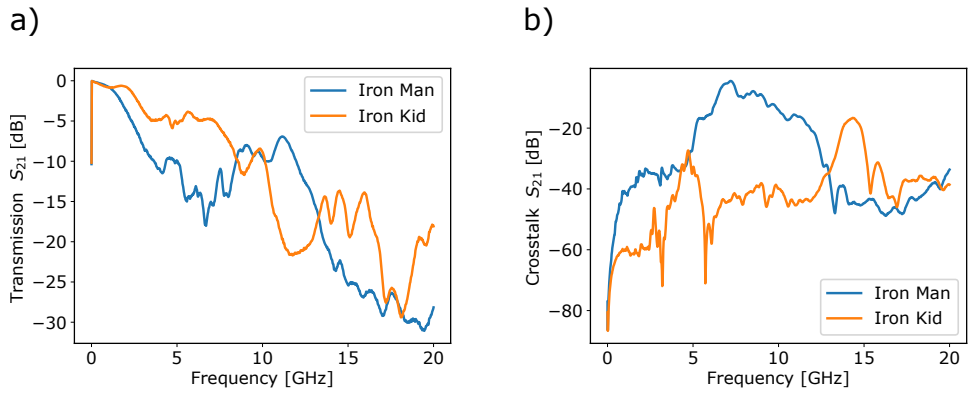


Figure 4.14: **Comparison of the fast gate transmission and the crosstalk between Iron Man and Iron Kid.** Measurement of the transmission **a** and the crosstalk **b** between fast gates on Iron Man PCB, number 2 (blue curves) and Iron Kid PCB, number 4 (orange curves). Important to mention is that Iron Man PCB, number 2 has 1 kΩ decoupling resistors and Iron Kid PCB, number 4 has 220 pF coupling capacitors. The S_{21} between the fast gates, in both cases, was measured using the ZNB20 vector network analyzer without calibration, Huber&Suhner SMA cables CBL-6FT-SMSM+, SMA to SMA feed-throughs and SMA to SMP adaptors. For the transmission measurements, three parallel Aluminium bond wires (3.5 mm long for Iron Kid and 2.5 mm long for Iron Man) were bonded between fast gates 2 and 4. For the crosstalk measurements the bond wires were removed.

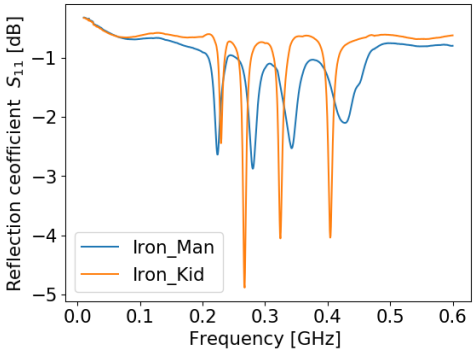


Figure 4.15: **Room temperature measurement of the reflectometry reflection coefficient S_{11} on Iron Kid, number 5 and Iron Man, number 2.** S_{11} was measured with the vector network analyzer ZNB20, without calibration. The connection between the vector network analyzer port 1 and the reflectometry SMP on both PCBs consisted of a R&S ZV-Z193 cable, a SMA to SMA feedthrough and a SMA to SMP adaptor. Nothing was bonded to the reflectometry bonding pads during this measurement, so the resonant circuits consisted only of an inductor and the capacitance to the ground C_p. Therefore, the frequencies for which S_{11} reaches the minimum amplitude are the resonant frequencies of the matching circuits connected to reflectometry bonding pads, 24_R4, 18_R3, 12_R2, 06_R1, going from lower to higher frequencies. Their values can be found in Table A.1.

5 Qubit

This chapter describes the experimental realization of a Loss-DiVincenzo qubit, implemented as a spin state of a hole in a Ge HW DQD (consult Section 3.2).

5.1 The qubit setup

Let's first consider the exact setup, shown in Figure 5.1, which was used for performing the qubit experiments. The voltage pulses generated by the AWG, with the rise time of $\approx 2\,ns$, were used for a fast change between CB and PSB of the DQD (channel 3), for the IQ modulation (channels 1 and 2) and for the pulse modulation (PM) control of the VSG (channel 4). The pulses sent to the IQ input of the VSG, modulate the amplitude of the two orthogonal sinusoidal components of the signal on the VSG output, enabling thus a creation of burst signals with an arbitrary phase and amplitude. The frequency of the VSG signals (bursts) is typically in a GHz range so they are called MW signals (bursts). For example, let's consider a waveform for the two-axis spin rotation experiment, shown in Figure 5.6a. The burst can be imagined as a phasor[1] on a circle with a radius $A_{burst} = \sqrt{I^2 + Q^2}$ having a phase equal to $arctan(\frac{Q}{I})$. I is the in-phase input and Q is the quadrature VSG input. The pulses on AWG channels 1 and 2 (not shown in the figure) change the relative amplitude of I and Q, changing thus the phase of the second burst while keeping the A_{burst} constant during 9 ns duration of both bursts.

[1] https://en.wikipedia.org/wiki/Phasor

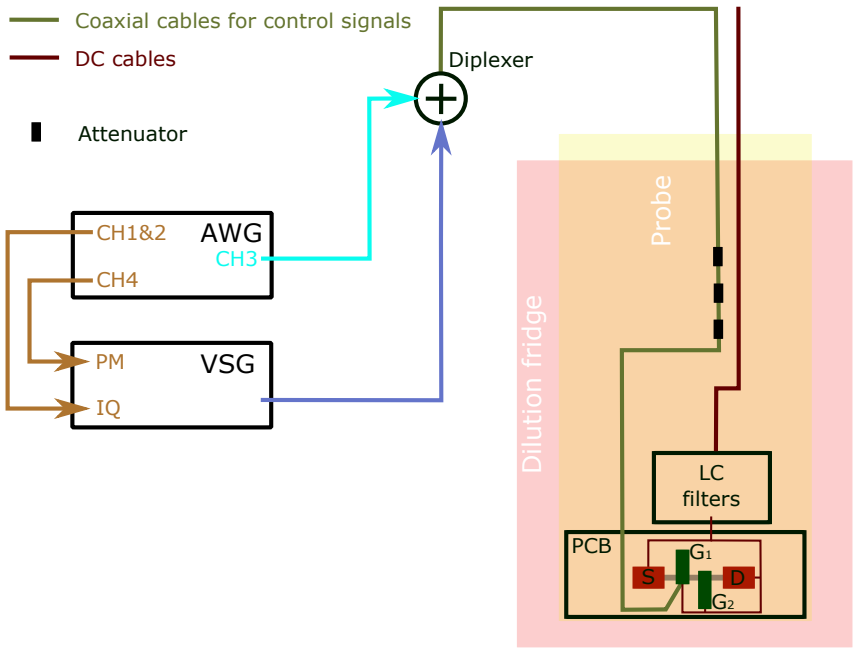


Figure 5.1: **Setup for the qubit experiment.** The qubit hosting DQD, located on a 6x6 mm^2 Si chip, was glued on the Iron Man PCB and mounted to the probe of the Grandpa Rudolph dilution refrigerator. Aluminium wire bonds connected all DQD electrodes to the DC lines while a bias tee allowed addition of HF signals to G1, as well. The HF signals were generated by the AWG (voltage pulses) and the vector signal generator (MW sinusoidal signals).

Outside of the 9 ns interval, the burst amplitude should be ideally zero, not to influence the qubit. In reality there is a finite burst amplitude also outside of the 9 ns intervals, defined by the so called on/off ratio. For the IQ modulation this ratio is $\approx 50\,dB$. Additionally, by applying a rectangular pulse, as a frame around each burst, at the PM input of the VSG, the on/off ratio can be increased to $\approx 80\,dB$. 20 dB is 10 times in terms of voltage and 100 times in terms of power. The waveform of the AWG channel 3 and the MW bursts are merged by the diplexer and sent towards the gate G1 of the DQD. Due to a longer overall electrical path (cable length + signal propagation in the VSG), the bursts delay in respect to the channel 3 pulse, in this particular case for about 20 ns. In order to align them, as in Figure 5.6a, the pulse needed to be intentionally delayed for the same time.

5.2 The qubit hosting DQD stability diagram

The stability diagram of the measured device (consult Figure 3.3c) is shown in Figure 5.2. Figure 5.2a, shows a somewhat larger gate-voltage phase space. The zoom-in into a pair of bias triangles, is shown in Figure 5.2b. The region of suppressed current, i.e. the PSB region (consult Figure 2.9), is clearly observable.

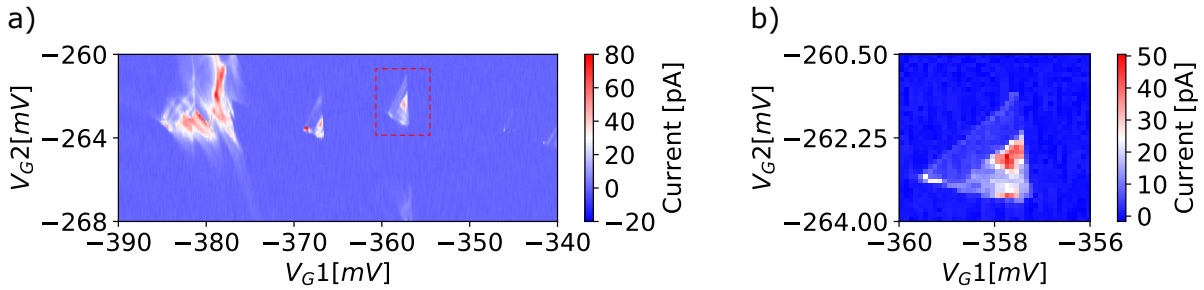


Figure 5.2: **The stability diagram of a qubit hosting DQD. a** V_{G1} versus V_{G2} scans, showing a stability diagram of the DQD. The measurements were performed by setting the gate-voltage point, generated by the IVVI DAC and subsequently measuring the current through the DQD with a dmm, having an integration time of 0.02 power line cycles (PLC). V_{SD} was set to 1.5 mV. Due to a relatively large V_{SD} and a small mutual capacitance C_m (in a few aF range), the two bias triangles overlap. The G1(2) coupling factor is $\alpha_{1(2)} \approx 0.68(0.65)$. **b** Zoom-in into the triangle pair enclosed in the red dashed square in a.

5.3 Spin manipulation experiments

5.3.1 EDSR spectroscopy

In order to verify the spin blockade and the ability to manipulate the spin, the EDSR experiment was performed in a continuous and in a pulsed mode. In the continuous mode the gate-voltage point was set into the region where PSB was assumed to take place, as shown in Figure 5.3a. In the pulsed mode, the spin manipulation and the spin initialization/readout intervals were set into the CB and PSB regions, respectively. This was done via the AWG pulse applied to G1, as can be seen in Figure 5.4a. In both cases, the frequency of the VSG generated MW signal, sent also to G1, was swept versus the out-of-plane magnetic field. The difference between the two experiments was that in the pulse mode, the MW signal was applied only during the CB part. Along the line for which the condition hf_{MW} equals the energy splitting between the respective states, the spin gets excited. This results in the transition from the blocked triplet to the

unblocked singlet state, in the PSB, increasing thus the current through the DQD and making such a line visible in the measurement. Indeed the lines were observed, as can be seen in Figure 5.3b and c for the continuous mode and in Figure 5.4b and c for the pulsed mode. In the continuous mode the amount of the current along the line depends on the spin rotation frequency and the tunneling rates, since, in the PSB region, it is energetically favorable for a hole to tunnel through immediately after the singlet state is formed. On the contrary, in the pulsed mode, a hole cannot tunnel immediately after its spin is rotated and the S(1,1) state is formed, because the DQD is in the CB. Once the pulse brings the DQD back to PSB, up to a few tunneling events can happen, until the triplet state is loaded again. Therefore, in the pulsed mode, the magnitude of the transport current is mainly limited with the pulse period. A longer period causes a lower current. Thus the upper line in Figure 5.3c has approximately 10 times larger current than the upper line in Figure 5.4c. Regrading the lower line, apart from a large g-factor change, between the two modes, it also changes from a peak to a dip in the measured current. The effect of the current reduction, along the EDSR line corresponding to the second harmonic, was observed in a DQD in GaAs heterostructure, as well [Laird *et al.*, 2009]. Also, multiple harmonics (multiple EDSR lines) were observed around zero detuning in an InAs nanowire DQD [Stehlik *et al.*, 2014]. In this study the current was enhanced along the odd harmonics and decreased along the even ones. Soon afterwards, both works were theoretically explained in terms of families of interfering trajectories of a strongly-driven multi-level quantum system [Danon and Rudner, 2014]. However, the lines we observed do not satisfy the criteria $g\mu_B B = nhf_{MW}$, with n being an integer. Therefore, the mentioned explanation is not applicable in our case.

In further experiments we focused on the upper line whose g-factor does not change (within the experimental error) and the current peak nature is preserved. Outside of the shown frequency and magnetic field range, the lines were not clearly observable and therefore only this range is shown.

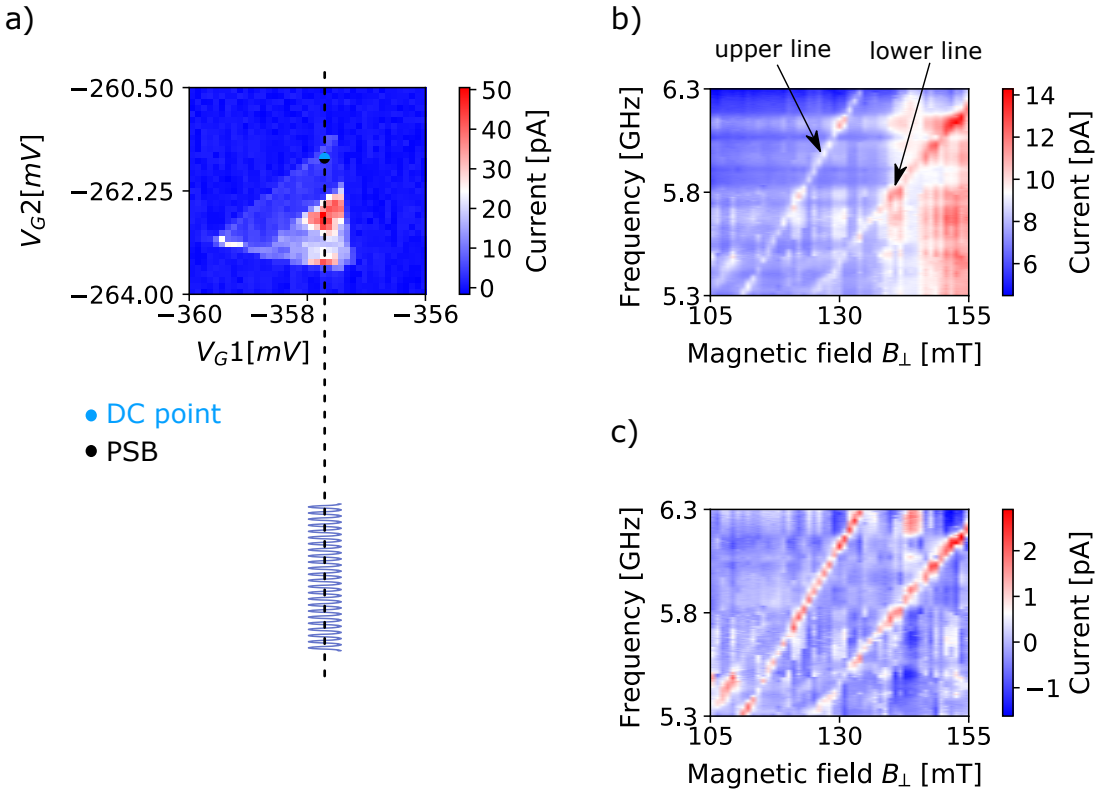


Figure 5.3: **Continuous EDSR spin spectroscopy. a** Zoom-in to the bias triangle, obtained with $V_{SD} = 1.5\,mV$. The static gate-voltage point (DC point) was positioned in the PSB region and the continuous MW signal (darker blue wave) was applied to G1. **b** Transport current signal measured versus the MW signal frequency and $B_\perp$. The power at the VSG output was set to $P_{MW} = -4\,dBm$. It was furthermore attenuated in the fridge to approximately $-64\,dBm$ at the device gate electrode. Every point was integrated for 200 ms (10 PLC) inside the dmm. The lines of the higher current mark the spin excitation to the unblocked singlet state. From the EDSR condition $hf_{MW} = g\mu_B B_\perp$, g-factors of 3 and 2.2 were extracted for the upper and the lower line respectively. **c** Same plot as in b, with the row and column mean values substracted from the corresponding data point.

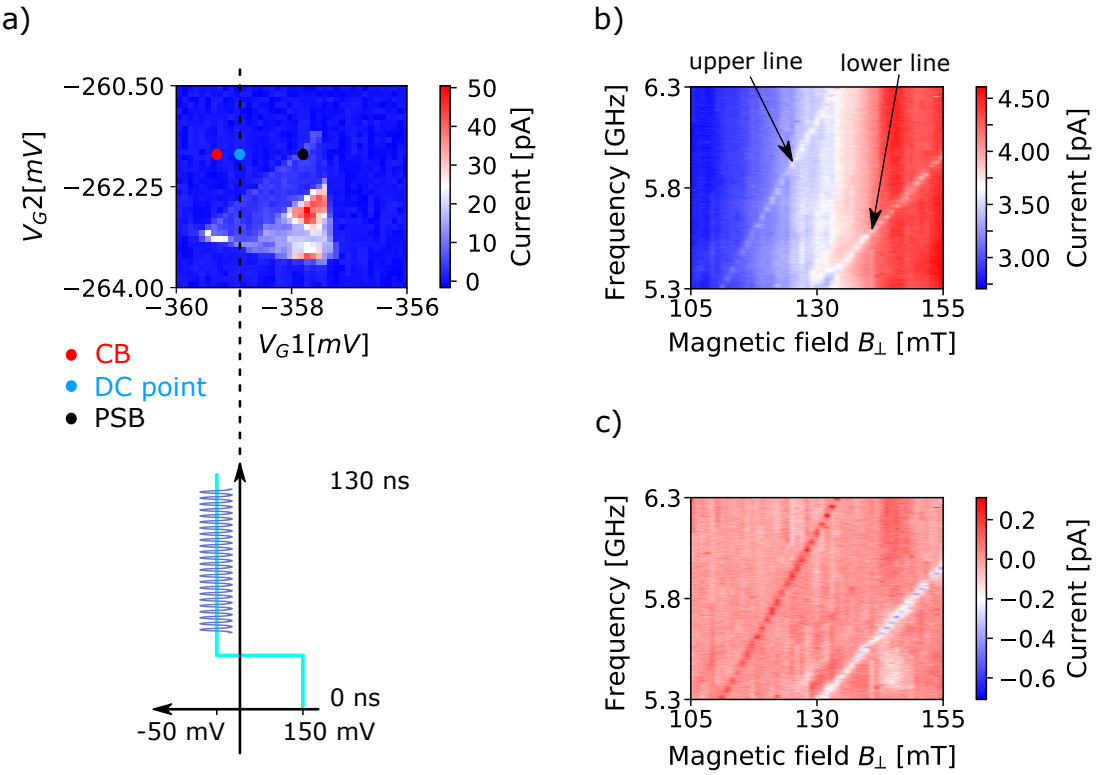


Figure 5.4: **Pulsed EDSR spin spectroscopy. a** Plot showing the same bias triangle as in Figure 5.3a. The AWG pulse, with a zero mean value, superimposed to the DC point, was rapidly changing the G1 voltage point between the CB (100 ns) and the PSB (30 ns) region. The pulse high and low values at the AWG output are stated here, which are then attenuated before reaching G1. During the CB part, 75 ns long MW burst (a bit shorter than the CB part of the pulse to ensure that it acts at G1 only during the CB), defined with 500 mV I and Q pulses, was applied to G1. Similar to before, the carrier power was set to $P_{MW} = -4\,dBm$. Since the VSG operates in the IQ modulation mode, for the actual signal power on its output, the amplitude of I and Q pulses plays a role here, as well. **b** Transport current versus MW burst frequency and $B_\perp$. Every point was integrated for 200 ms (10 PLC) inside the dmm. The g-factor changed significantly for the lower line, in respect to the continuous mode, and now it is ≈ 2.0. For the upper line the g-factor did not change (it is within the experimental error). **c** Same plot as in b, with the row and column mean values substracted from the corresponding data point.

The next experiments were performed with the DC point set at the similar position as in Figure 5.4a.

5.3.2 Rabi experiment

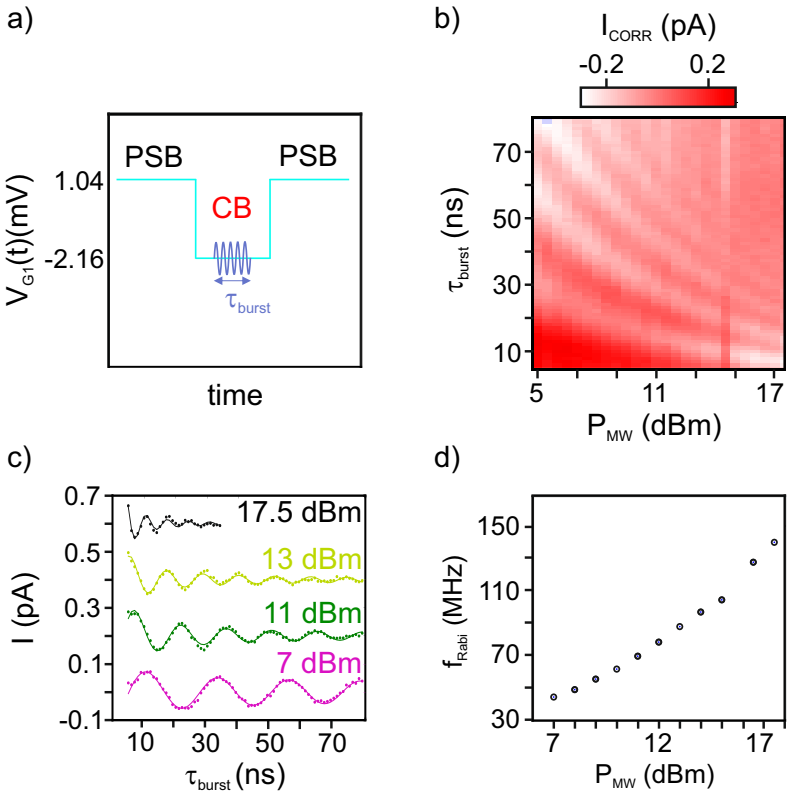


Figure 5.5: **Coherent spin oscillations around a single axis. a** Waveform applied to G1 for performing the Rabi experiment. The AWG pulse was shifting the qubit between PSB and CB, which lasted for 210 and 100 ns, respectively. The applied MW burst rotated the initialized spin-down vector for an angle proportional to its duration τ_{burst} and the square root of power $\sqrt{P_{MW}}$. The I and Q pulses, for the burst control, had a 500 mV amplitude, each. **b** Corrected current I_{CORR} versus τ_{burst} and P_{MW} for $B_{\perp} = 127\,mT$ and $f_{MW} = 5.966\,GHz$, showing Rabi oscillations. For every τ_{burst},P_{MW} point, the waveform shown in **a** was continuously applied during the dmm integration time of 200 ms (10 PLCs) and the averaged current was recorded. This was repeated 100 times. Each single point current value is the result of these two averaging procedures. The signal power on the x-axis is the power on the VSG output. The actual power on the sample was attenuated by approximately 60 dB. The current data has been corrected by removing the average column and row values from the corresponding data points. The trace for P = 14.5 dBm stands out because the DQD stability diagram got shifted during this trace. **c** Current I vs τ_{burst} traces for P_{MW} equal to 7, 11, 13 and 17.5 dBm. For clarity, the traces for 11, 13 and 17.5 dBm are shifted by 200, 400 and 600 fA, respectively. The Rabi frequencies were extracted by fitting the raw data to $\frac{A}{\tau_{burst}^{a}} sin(2\pi f_{Rabi}\tau_{burst} + \phi_R) + offset + d\sqrt{\tau_{burst}}$, where ϕ_R is the initial phase of a single trace. The $offset$ and $d\sqrt{\tau_{burst}}$ have been subtracted from the shown traces. **d** Dependence of the Rabi frequency on the applied MW power.

After performing the pulsed EDSR spectroscopy, one point at the upper line in Figure 5.4b was chosen, such that the respective f_{MW} and $B_{\perp}$ satisfy the resonant condition $hf_{MW} = g\mu_B B_{\perp}$. With that condition satisfied, the waveform shown in Figure 5.5a, applied to G1, coherently rotates the hole spin state around a single axis. During the PSB interval, the system is initialized in the triplet state. When in CB, a MW burst of varying duration is applied. For a π-pulse the hole spin will flip, leading thus to the singlet state when the DQD is brought back to the PSB region. Now, the transport is enabled through the S(0,2) state leading to an enhanced current. By linearly increasing the burst duration τ_{burst}, oscillations of the detected current can be observed (Figure 5.5b). For a more detailed explanation, please refer to the corresponding section in the theory chapter. As expected, the period of the Rabi oscillations decreases with increasing power of the MW burst (see Figure 5.5c). Rabi frequencies approaching 140 MHz were observed (Figure 5.5d). They are faster than the frequencies reported for GaAs system dressed with an artificial spin orbit coupling (i.e. slanted magnetic fields generated by micro magnets) [Yoneda *et al.*, 2014]. Also faster than what has been predicted for Ge nanocrystals [Ares *et al.*, 2013] and than those reported for the InSb electron spin qubit which showed 8 ns dephasing time [van den Berg *et al.*, 2013].

5.3.3 Two-axis qubit manipulation

In order to demonstrate the two-axis qubit rotation, a periodic waveform, whose single period is illustrated in Figure 5.6a, was applied to G1. Two MW bursts, separated by a fixed interval τ_{wait} were applied during the manipulation interval. The first MW burst rotates the initialized spin state for an angle of $\frac{\pi}{2}$ around the x-axis. The phase of the second MW burst ϕ_p determines the angle of the corresponding rotation axis in the x-y plane. ϕ_p was changed by sweeping the relative amplitudes of the VSG I and Q inputs, while A_{burst} was kept constant, as explained above. Sweeping ϕ_p from 0 to 2π causes a sinusoidal oscillation of the measured current through the DQD (consult Figure 5.6b)

which represents the spin up probability $P|\uparrow\rangle$. For more detailed explanation, please refer to the corresponding section in the theory chapter. As an additional note, the DC point needed to be slightly changed since the bias triangle shifted for -0.5 mV in both gates, in respect to the previous experiment.

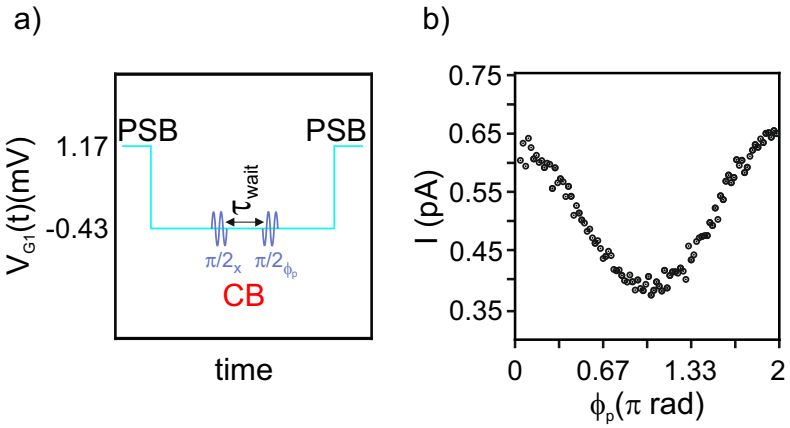


Figure 5.6: **Two-axis qubit manipulation. a** Waveform applied to G1 for performing the two-axis qubit rotation. The manipulation interval (CB) lasted 160 ns while the read-out and the initialization (PSB) lasted for 30 ns. The phase ϕ_p of the second burst was changed by sweeping the relative amplitudes of the burst controlling I and Q pulses, while $A_{burst} = 500\sqrt{2}\,mV$ was kept constant. This phase determines the phase of the spin rotation vector during the second burst. **b** Current through the DQD versus ϕ_p. For every ϕ_p value, the waveform shown in **a** was continuously applied during the dmm integration time of 200 ms (10 PLCs) and the averaged current was recorded. This was repeated 5 times. Each single point current value is the result of these two averaging procedures. The oscillatory behavior of the current demonstrates the qubit rotation around the axis defined by ϕ_p. For this experiment the following parameters were chosen: $P_{MW} = 4\,dBm$, $\tau_{burst} = 9\,ns$, $\tau_{wait} = 10\,ns$, $f_{MW} = 5.887\,GHz$ and $B_\perp = 122\,mT$.

5.3.4 Dephasing T_2^* - Ramsey experiment

To measure the inhomogeneous dephasing time T_2^*, a Ramsey experiment was performed. A periodic waveform, whose single period is illustrated in Figure 5.7a, was applied to G1. Two $\frac{\pi}{2}$ bursts, separated by τ_{wait}, during which the qubit can freely evolve and dephase, were applied during the manipulation interval. The burst frequency f_{MW} is detuned from the Larmor frequency by $\Delta f = f_z - f_{MW}$, which sets the rotation vector in the x-z plane during both bursts and along the z-axis during the τ_{wait}. Because of the z-rotation, with the speed proportional to Δf, the measured current oscillates as a function of τ_{wait}, as can be seen in Figure 5.7b and c. From the decay time of these oscillations, average dephasing times exceeding 130 ns were measured (consult Figure 5.7d).

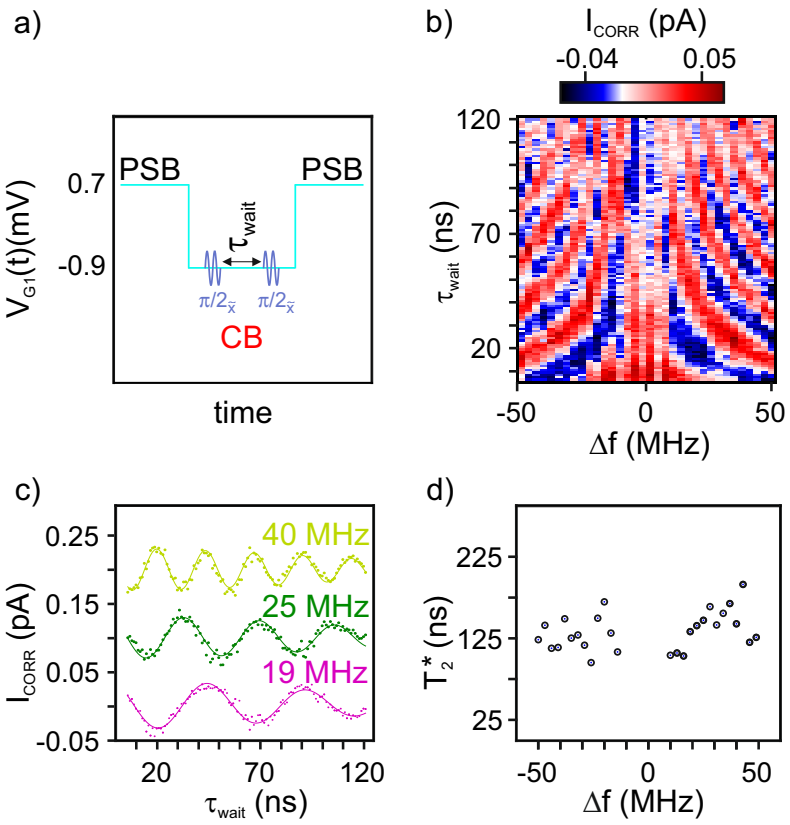


Figure 5.7: **Ramsey experiment. a** Waveform applied to G1 for inducing Ramsey oscillations caused by the frequency detuning Δf between the Larmor and the MW burst frequency. The square pulse shifted the qubit between PSB (210 ns) and CB (160 ns). The two MW bursts, separated by the waiting time τ_{wait}, had the same phase with P_{MW} and τ_{burst} calibrated for a $\frac{\pi}{2}$ spin rotation around the x-axis. The I and Q pulses, for the bursts control, had a 500 mV amplitude, each. **b** I_{CORR} versus τ_{wait} and Δf for $P_{MW} = 11\,dBm$ and $\tau_{burst} = 3.5\,ns$ in the presence of $B_{\perp} = 127\,mT$ and a center frequency of $f_{MWcenter} = f_z = 5.966\,GHz$. For every τ_{wait}, Δf point, the waveform shown in **a** was continuously applied during the dmm integration time of 200 ms (10 PLCs) and the averaged current was recorded. This was repeated for 35 times. Each single point current value is the result of these two averaging procedures. **c** Line traces from b for Δf equal to 19, 25 and 40 MHz. The traces for 25 and 40 MHz are shifted by 100 and 200 fA, respectively. **d** Plot showing the extracted dephasing times for various values of Δf. The times were extracted by fitting the data to $Ae^{-(\frac{\tau_{wait}}{T_2^*})^2} sin(2\pi\Delta f\tau_{wait}+\phi_{Ram})+offset$, where ϕ_{Ram} is the initial phase of a single Ramsey trace, example of which is shown in c. The average dephasing time exceeds 130 ns.

5.3.5 Conclusion

The ratio of T_2^* to a π-burst duration for a MW power of 11 dBm is about 18 which is 35 times smaller than the highest value reported for electron spins in isotopically purified Si [Yoneda *et al.*, 2017] but just a factor of two compared to electron spins in natural Si [Takeda *et al.*, 2016]. We have also observed that for increasing MW power and consequently decreasing the π-burst duration, T_2^* stays approximately constant, therefore increasing the mentioned ratio. Additional Rabi and Ramsey experiments were performed, a couple of months later, on the same triangle, in a similar DC point, with different T_{CB} and T_{PSB} and a different $\frac{\pi}{2}$-burst duration (in the Ramsey experiment case). The major difference to the previous experiment was a 30^0 angle that the applied static magnetic field had in respect to the perpendicular direction. The average dephasing time was $34\,ns$, in that case, with the MW power of $3\,dBm$ and a $\frac{\pi}{2}$-burst of 10 ns. In conclusion, since this is a first qubit realization in such a material system, a lot is left to be investigated. For example, the exact rotation mechanism, the sources of noise limiting the coherence times and how to mitigate them. Also, the assumption of the basis states being $T_-(1,1)$ and the singlet, needs to be confirmed. In order to investigate the dephasing noise, spin echo and Carl-Purcell-Meiboom-Gill experiments need to be performed. But since the measured current reduces for longer pulse periods, as explained above, it was not possible to extend the period of the waveform, shown in Figure 5.7a, more than 400 ns. Thus, for performing such experiments, a readout method that allows longer manipulation periods is needed.

6 Gate based charge and spin sensing

An important requirement from DiVincezo's qubit criteria is a qubit state readout capability. Apart from the initialization and manipulation, a high readout fidelity, obtained in a short integration time, is required as well. In the first place in order to satisfy the quantum error correction threshold and furthermore to reduce the number of required physical qubits entering the error correction algorithm that yields a single logical qubit [Fowler *et al.*, 2012]. In semiconductor DQD spin qubits, the spin can be read-out indirectly, by mapping it to the charge state, using the PSB [Ono *et al.*, 2002]. The charge state can be then measured by i.e. measuring the tunneling current through a DQD, but this method returns very weak signals (therefore prohibiting longer manipulation periods, as stated above), requiring thus a lot of averaging (slow). Therefore, it can be used only for initial characterizations. Alternatively, the charge state of a DQD can be measured using proximal charge sensors, like quantum point contacts [van Wees *et al.*, 1988] and single electron transistors [Kastner, 1992]. Due to the electrostatic coupling, the qubit charge state maps to their conductance. Later on, such sensors were integrated into resonant circuits for the reflectometry readout, where their conductance change modifies the amount of the wave reflected from the resonant circuit, as introduced above. This resulted in an increased sensitivity for the so called RF quantum point contacts [Reilly *et al.*, 2007; Cassidy *et al.*, 2007], and even more for the RF single electron transistor [Schoelkopf *et al.*, 1998; Henrik *et al.*, 2006]. But, implementing charge sensors requires more nanofabrication steps, opposing thus to the scalability requirement. Another negative side of a

charge sensor is the necessity for additional tuning. Since DQD based spin qubits are typically read-out in the PSB regime, where singlet and triplet states have different curvatures when changing the detuning, the qubit can be alternatively read-out by sensing their consequently different quantum capacitances [Persson *et al.*, 2010; Ashoori *et al.*, 1992; Duty *et al.*, 2005]. This can be achieved by connecting the resonant circuit to either the source or drain contact [Petersson *et al.*, 2010; Petersson *et al.*, 2012; Pakkiam *et al.*, 2018] or to a gate electrode (gate reflectometry) [Colless *et al.*, 2013; West *et al.*, 2019; Urdampilleta *et al.*, 2019], especially in the case of high gate to dot coupling factors [Zalba *et al.*, 2015; Crippa *et al.*, 2019]. Since gates already exist, for the DQD creation and its electrostatic control, by using the gate based readout, the fabrication gets simpler, avoiding also an additional tuning of the charge sensor. Furthermore, such a gate based sensor does not suffer from shot noise [Ahmed *et al.*, 2018], the charge sensors are suffering from, paving the way towards even higher sensitivities and consequently higher readout fidelities [Zheng *et al.*, 2019; Schaal *et al.*, 2020]. Due to high gate to dot coupling factors in Ge HW DQDs, typically $\alpha > 0.5$, it was natural to use gate reflectometry for their readout.

6.1 Gate reflectometry working principle

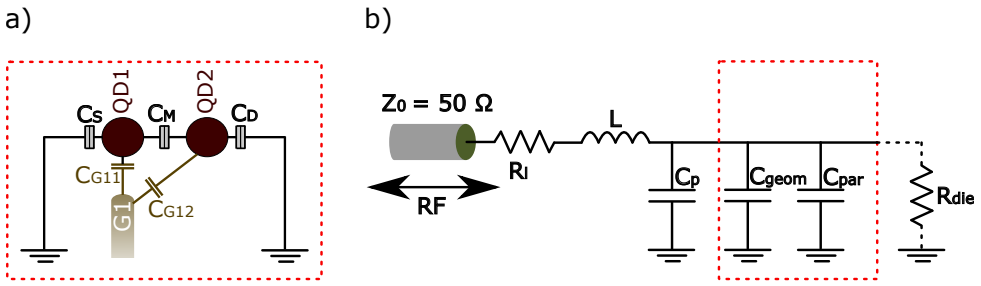


Figure 6.1: **Adapted schematic of a DQD with the reflectometry circuit connected to G1. a** Schematic of DQD shown in Figure 2.6, as seen from G1, in the zero bias case. **b** Schematic of the reflectometry circuit from Figure 4.6, with the inductor (L) connected to G1. The DQD is represented with an equivalent circuit at finite frequencies, consisting of a parallel combination of C_{geom} and C_{par}. Losses in the dielectric R_{die} represent the sum of losses in the PCB and in C_{geom}.

All considerations and derivations here are taken mostly from [Mizuta *et al.*, 2017] and [Crippa *et al.*, 2019]. In gate reflectometry, the inductor is connected to a gate and therefore the device part of the reflectometry circuit schematic, shown in Figure 4.6, needs modification. There is also a difference in the circuit loss representation. Apart from the already introduced R_l, the dielectric losses R_{die} are taken into account here, as well. They predominantly originate from losses in the PCB and the device geometric capacitance dielectric and their value can be in tens of $k\Omega$ [Zalba *et al.*, 2015]. Figure 6.1a shows a DQD schematic, with the elements that play a role from the G1 standpoint, in the zero bias case. In the DQD devices described here, the mutual capacitance C_M is on the order of $10^{-18}\,F$ and the total capacitance $C_{\Sigma 1(2)} = C_{G11(12)} + C_{S(D)} + C_M$ is on the order of $10^{-17}\,F$ [Watzinger, 2018]. Therefore, by following the derivations in [Mizuta *et al.*, 2017], in the limit $C_M << C_\Sigma$ and for finite frequencies, the DQD can be represented as a parallel combination of the geometrical capacitance C_{geom} and the parametric capacitance C_{par}, as shown in Figure 6.1b. The voltage independent capacitance part $C_{geom} = \frac{\alpha_{11}}{|e|}C_S + \frac{\alpha_{12}}{|e|}C_D$ is given by the DQD geometry. Here, $\alpha_{11(12)} = |e|\frac{C_{G11(12)}}{C_{\Sigma 1(2)}}$ is the G1 to QD1(2) coupling factor and e is the electron

charge. The parametric capacitance

$$C_{par} = \alpha^{'} \frac{\delta \langle n_1 \rangle}{\delta V_{G1}} \tag{6.1}$$

is an additional capacitive contribution that arises from a functional dependence of the DQD charge state upon the voltage applied to G1 (V_{G1}). Here, $\alpha^{'} = \alpha_{11} - \alpha_{12}$, and $\langle n_1 \rangle$ is the average electron number in QD1. Furthermore, C_{par} can be expressed in terms of the detuning parameter ϵ, i.e. the energy difference between the two respective DQD charge states, as:

$$C_{par} = \alpha^{'2} \frac{\delta \langle n_1 \rangle}{\delta \epsilon} \tag{6.2}$$

When sending a reflectometry signal to the resonator, the detuning oscillates around ϵ_0 with the signal frequency ω, as $\epsilon(t) = \epsilon_0 + d\epsilon sin(\omega t)$. The amplitude of those oscillations is $d\epsilon = \alpha^{'} dV_{G1}$. Here dV_{G1} is the amplitude of the voltage oscillations, seen by the G1, produced by the resonator as a response to the excitation signal and $\alpha^{'}$ the corresponding V_{G1} to ϵ conversion factor.

Now, let's dig a bit deeper into the physical origin of C_{par}, starting with a simple charge qubit example. A charge qubit, hosted in a singly occupied DQD, can be described with the following Hamiltonian:

$$H = t_c \sigma_x + \frac{\epsilon}{2} \sigma_z \tag{6.3}$$

having the corresponding energies:

$$E_{\pm} = \pm \frac{1}{2} \sqrt{\epsilon^2 + (2t_c)^2}. \tag{6.4}$$

Following the derivation in [Mizuta *et al.*, 2017], Equation 6.2 evolves to:

$$C_{par} = \frac{\alpha'^2}{2}[\frac{(2t_c)^2}{\Delta E^3}\Delta P + \frac{\epsilon}{\Delta E}\frac{\delta \Delta P}{\delta \epsilon}] \tag{6.5}$$

where $\Delta E = E_+ - E_- = \sqrt{\epsilon^2 + (2t_c)^2}$ is the energy difference and $\Delta P = P_+ - P_-$ is the difference between occupation probabilities of the ground and excited state. The first term in Equation 6.5 accounts for adiabatic transitions in systems with a finite curvature of the energy bands and it is called quantum capacitance (C_Q). The second term, called tunneling capacitance (C_t) arises due to non adiabatic transitions caused by the excitation and relaxation processes with timescales comparable or faster than the reflectometry excitation frequency ω. In the scope of this work, non-adiabatic processes can be neglected, as can be seen in the experimental data shown below, making thus $C_{par} \approx C_Q$:

$$C_{par} \approx \frac{\alpha'^2}{2}\frac{(2t_c)^2}{\Delta E^3}\Delta P = C_Q \tag{6.6}$$

Regarding the spin qubit, near zero detuning, a doubly occupied DQD can be mapped onto five states $S(0,2)$, $S(1,1)$, $T_-(1,1)$, $T_0(1,1)$, $T_+(1,1)$, as already explained above. Due to the similarity with the system described in [Crippa *et al.*, 2019], the following Hamiltonian for small detunings

$$H = \begin{bmatrix} -\frac{1}{2}\epsilon + \frac{1}{2}(g_1+g_2)\mu_B B & 0 & 0 & 0 & 0 \\ 0 & -\frac{1}{2}\epsilon & 0 & \frac{1}{2}(g_1-g_2)\mu_B B & 0 \\ 0 & 0 & -\frac{1}{2}\epsilon - \frac{1}{2}(g_1+g_2)\mu_B B & 0 & 0 \\ 0 & \frac{1}{2}(g_1-g_2)\mu_B B & 0 & \frac{1}{2}\epsilon & t_c \\ 0 & 0 & 0 & t_c & -\frac{1}{2}\epsilon \end{bmatrix} \tag{6.7}$$

can be applied here as well. g_1 is the g-factor in QD1 and g_2 is the g-factor in QD2. The state energies versus detuning are shown in Figure 2.9, at the bottom. For $\epsilon_0 = 0$ and $B = 0$ all the elements in Equation 6.7 are approximately zero, apart from the off

diagonal elements in the lower right 2x2 submatrix, which is then equal to the charge qubit Hamiltonian in Equation 6.3. Therefore, the only non zero quantum capacitance, which is the one coming from the energy curvature of the singlet states (due to t_c), can be expressed using Equation 6.6, for the charge qubit, as:

$$C_Q = \frac{\alpha^{'2}}{2}\frac{(2t_c)^2}{\Delta E^3}\Delta P_S. \tag{6.8}$$

The difference is in the state occupation probabilities, which is now expressed as ΔP_S, taking into account all five states (two S and three T). The expression for ΔP_S can be found in [Mizuta *et al.*, 2017] and for the 0 K limit it is equal to 1, meaning that only the singlet state can be occupied in this case

$$C_Q = \frac{\alpha^{'2}}{2}\frac{(2t_c)^2}{\Delta E^3}. \tag{6.9}$$

For $B > 0$, the non zero $\frac{1}{2}(g_1 - g_2)\mu_B B$ term (Equation 6.7), assuming a g-factor difference in the two dots, couples $S(1,1)$ and $T_0(1,1)$. This causes a curvature and a non-zero quantum capacitance also for the $T_0(1,1)$ state, as can be seen in Figure 2.9b, at the bottom [Crippa *et al.*, 2019].

The C_Q and the parametric capacitance in general, can be probed by measuring the reflected portion of the reflectometry excitation signal sent towards the resonator in Figure 6.1. The detuning oscillations cause an increased DQD charge oscillation, for larger C_{par}, loading thus the resonator and changing the reflection coefficient phase $\Delta\Gamma_\phi$ and amplitude $\Delta|\Gamma|$. By sweeping ϵ_0, across a DQD inter-dot charge transition, the corresponding C_{par} can be mapped out.

Let's now look into the gate reflectometry sensitivities, in respect to C_{par}. Using Equation 4.14, the gate reflectometry phase sensitivity $\frac{\delta\Gamma_\phi}{\delta C_{par}}$ reads as:

$$\frac{\delta\Gamma_\phi}{\delta C_{par}}|_{\omega=\omega_0} = \frac{2QZ_0}{C_{tot}(R_{eff} - Z_0)} \tag{6.10}$$

where $C_{tot} = C_p + C_{geom}$ and $R_{eff} = R_l + \frac{L}{C_{tot}R_{die}}$. If R_{die} is large enough, such that $R_{eff} << Z_0 = 50\,\Omega$ then:

$$\frac{\delta\Gamma_\phi}{\delta C_{par}}|_{\omega=\omega_0} \approx -\frac{2QZ_0}{C_{tot}Z_0} = -\frac{2Q}{C_{tot}} \tag{6.11}$$

and the reflected signal phase change $\Delta\Gamma_\phi$ at the resonant frequency ω_0 is:

$$\Delta\Gamma_\phi|_{\omega=\omega_0} \approx \frac{\delta\Gamma_\phi}{\delta C_{par}}|_{\omega=\omega_0}\Delta C_{par} = -\frac{2Q\Delta C_{par}}{C_{tot}} \tag{6.12}$$

Regarding the gate reflectometry amplitude sensitivity in respect to C_{par}, by substituting R_{die} instead of R_D in Equation 4.16, $\frac{\delta|\Gamma|}{\delta C_{par}}$ can be written as:

$$\frac{\delta|\Gamma|}{\delta C_{par}}|_{\omega=\omega_0} = \frac{-2Z_0Q^2}{C_{tot}R_{die}} \tag{6.13}$$

Having R_{die} in tens or even hundreds of $k\Omega$, can still result in a non negligible gate reflectometry amplitude response. Depending on the driving regime, C_{par}, in the above equations, can be replaced with C_Q for adiabatic and with C_t for the non adiabatic regime.

Now, by combining Equations 6.9 and 6.12, the gate reflectometry phase signal, near the DQD inter-dot transition, can be evaluated in the 0K limit as:

$$\Delta\Gamma_\phi^{T=0} = -\frac{2Q\frac{\alpha'^2}{2}\frac{(2t_c)^2}{\Delta E^3}}{C_{tot}} \tag{6.14}$$

stemming from the quantum capacitance of the singlet state. For a complete description of $\Delta\Gamma_\phi$, at elevated temperatures, averaged phase signal contributions of each state $\langle\Delta\Gamma_\phi\rangle_i$, should be summed up: $\Delta\Gamma_\phi = \Sigma\langle\Delta\Gamma_\phi\rangle_i$. The single state phase signal can be described as:

$$\langle\Delta\Gamma_\phi\rangle_i = \Delta\Gamma_{\phi i}^{T=0}e^{-E_i\beta}/Z \tag{6.15}$$

where $\Delta\Gamma_{\phi i}^{T=0}$ is proportional to the quantum capacitance of the state with energy E_i in the 0 K limit, $\beta = \frac{1}{k_B T_{eff}}$ with k_B as Boltzmann constant, T_{eff} the effective electron temperature and Z the partition function over the five states.

Tunnel coupling estimation procedure By using the above presented model [Crippa *et al.*, 2019] one can obtain the evolution of the full width at half maximum (FWHM) of the inter-dot transition line cut (an example can be seen in Figure 6.3c) versus T_{eff}, measured as $\Delta\Gamma_\phi$ (consult Figure S3 [Crippa *et al.*, 2019]). The FWHM value changes from $3t_c$ to $4t_c$, allowing to estimate t_c in limits from FWHM/4 to FWHM/3, whatever the actual effective electron temperature is.

6.2 Experimental results

Experimental flow Initially we were trying to perform the gate reflectometry measurements on our typical two gate DQD devices, similar to the one used for the qubit (consult Figure 3.3c). Since the gate reflectometry signal was not reproducible and too weak, we tried to increase the signal by increasing the already high α. This was done by removing the native Si oxide before depositing the intentional layer of oxide, with a decreased thickness (Section 3.3.1). All the other fabrication parameters did not considerably change, except for the wafer. Three identical samples were fabricated and measured. Indeed, a better gate reflectometry signal was observed, but still there was no clear inter-dot charge transition signal which could lead to the qubit implementation. Tuning towards the qubit regime was prohibited by a limited gate-voltage range caused by current leakage through the gate oxide for gate voltages in the range of tens or hundreds of mV. Also there were a lot of background lines, not corresponding to DQD charge transitions and a lot of noise in the gate reflectometry signal. In order to reduce the amount of random charges below gate electrodes, which were presumably the reason for the additional lines and the noise, the etching step was introduced at the beginning of the DQD fabrication (Section 3.3.1). The idea was to etch away the

Si cap, together with the HWs and leave only a small non-etched area around the target HW. The etching recipe was inherited from other group members, without testing, with the assumption that ”it cannot harm”. With the combination of etching and oxide reduction, nicely observable DQD inter-dot charge transitions were obtained, with the best data (sample ”S228_111”) presented below. However, the still very small leak free gate-voltage range, prohibited the tuning towards the qubit regime. To get a better insight into this problem, samples excluding the etching or the HFA dip (native Si oxide removal) step or both, were fabricated. Also, different HfO_2 oxide ALD recipes were tried out and the overall findings pointed out the HFA dip as detrimental for the gate-voltage range. On the other hand, both the etching and the HFA dip proved to increase the gate reflectometry signal quality.

All in all, the lack of tunability in DQD devices, that showed usable reflectometry signals, highlighted the necessity of sweeping through a number of fabrication parameters. Different gate oxides and the implementation of more gate electrodes for tuning the tunnel barriers were tested first. In this direction, several samples with a different middle gate design and native Al oxide below the main gates were fabricated (Section 3.3.1). A version with the middle gate on top (the representative sample is ”MJ_5_S33”), showed inter-dot tunnel barrier tunability (consult Figure 3.6), but it was too unstable, presumably due to the absence of the etching and the HFA dip steps. In parallel to the sample optimization, superconducting planar coils (inductors), etched out of a 100 nm thick NbTiN film, were fabricated on the separate chip and bonded instead of the SMD copper inductors. This increased the quality factor of the reflectometry circuit.

The gate reflectometry data, from the two representative samples, is presented below.

6.2.1 Sample "S228_111"

As explained above, in addition to the standard two gate DQD fabrication, the native Si oxide removal and the etching step were added.

A SEM image of the measured device is shown in Figure 6.2a. The gates are shifted towards the source S lead due to a slight misalignment during the e-beam fabrication step. The sample was mounted on the Iron Man, number 2 PCB. G2 was bonded to the 12_R2 bonding pad, with a 680 nH copper inductor (the inductor configuration at Iron Man, number 2, at that time, was different then the one listed in Table A.1). From the resonant frequency of $f_{res} = 275.19\,MHz$, a parasitic capacitance of $C_p \approx 0.5\,pF$ was extracted. The corresponding resonant circuit quality factor was $Q \approx 33$. The gate reflectometry data, shown in Figure 6.2b and d, was measured by the lockin technique, using the UHFLI, with the reflectometry excitation signal frequency $f = f_{res} = 275.19\,MHz$. The excitation power was set to -30 dBm which translates into $\sim -92\,dBm$ on the resonant circuit. The UHFLI demodulator low-pass filter was set to a fourth order and the time constant to 30 ms. After setting the gate-voltage point and waiting for 75 ms, for the low-pass filter to settle down, 2000 samples were recorded and averaged with a sampling rate of 880 kSa/s, yielding the reflected amplitude and phase value for each point.

Here the focus is on the origin of the inter-dot transition signal, since this is important for the qubit readout. Around $\epsilon_0 = 0$, C_Q (assuming the adiabatic regime) increases due to a band curvature of the ground state (either the singlet or a charge state in a singly occupied DQD), loading thus the resonator and shifting the phase (Equation 6.12, red stripe in Figure 6.2d) and the amplitude (Equation 6.13, blue stripe in the middle of Figure 6.2b). From the measurements presented above it is not possible to say if the DQD was singly or doubly occupied. This is so, because, in the case of B=0 T and for the adiabatic regime the doubly occupied DQD has a singlet ground state and consequently a similar inter-dot charge transition signal as a singly occupied

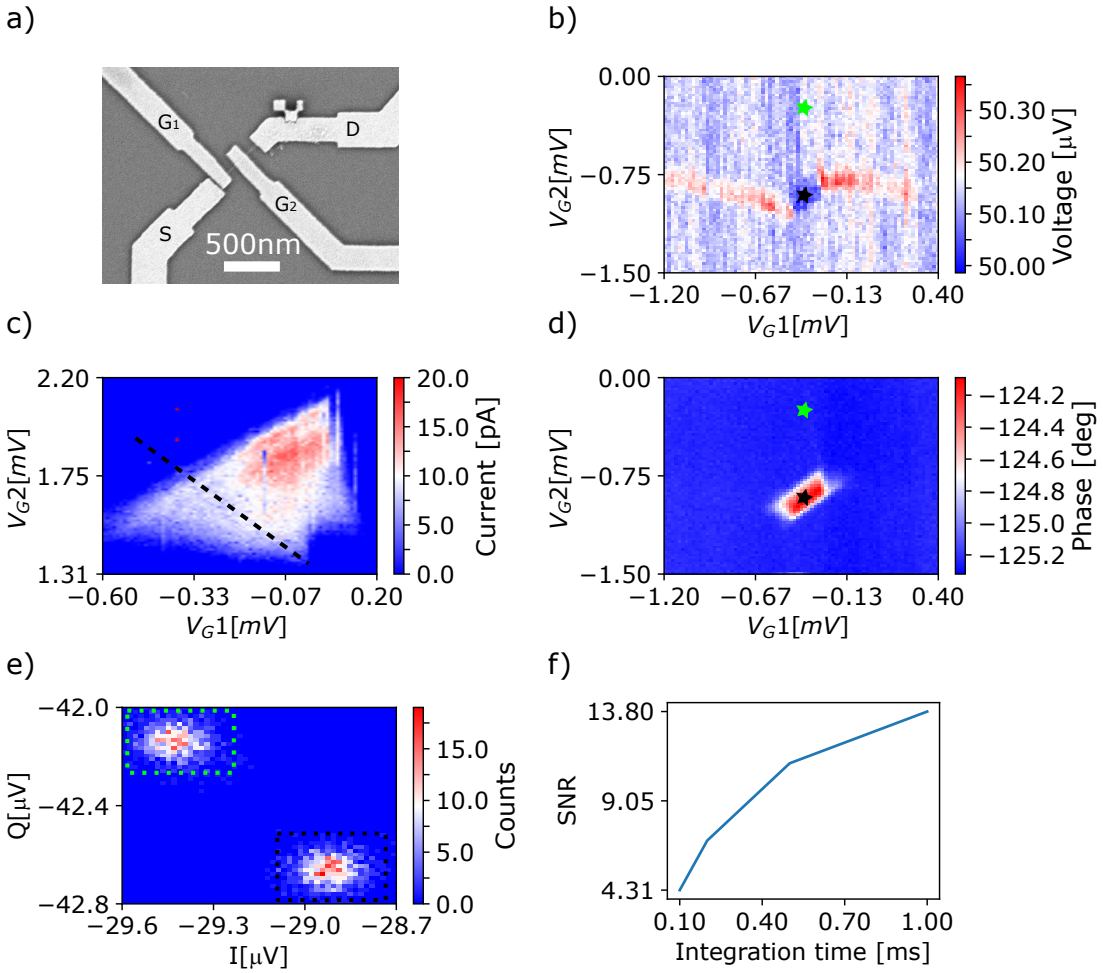


Figure 6.2: **SEM image and gate reflectometry data from the sample "S228_111".** The data presented here is recorded with $B = 0\,T$ at the Grandpa Rudolph fridge base temperature of $\sim 30\,mK$. **a** SEM image of the DQD device from the "S228_111" sample, on which all the data presented below is measured. **b** and **d** V_{G2} versus V_{G1} stability diagram showing the inter-dot charge transition measured as the reflected voltage amplitude **b** and the phase **d**, with $V_{SD} \approx -50\,\mu V$. **c** An adjacent pair of bias triangles, measured with $V_{SD} \approx 500\,\mu V$ and a dmm integration time of 60 ms. The corresponding bias triangle pair is much uglier and no gate to dot coupling factors could be extracted, so this one is used instead, since it is very similar in size. The black dashed line marks the DQD energy detuning direction. Since the line is perpendicular to the triangle base (does not appear perpendicular because the aspect ratio of x and y axes is not 1), the corresponding gate to dot coupling factor α_{det} can be extracted as $\alpha_{det} = \frac{|eV_{SD}|}{\Delta V_{Gdet}} \approx 0.9\,\frac{eV}{V}$, where ΔV_{Gdet} is the length of the line. **e** Plot showing a 2D histogram of the demodulated reflected signal I and Q components, for the integration time of 10 ms. The lower right blob corresponds to I and Q distributions for V_{G1} and V_{G2} set to the values marked by the black star in **b** and **d**, while the upper left blob corresponds to the green star in **b** and **d**. Plot showing the SNR measured for different integration times.

DQD.

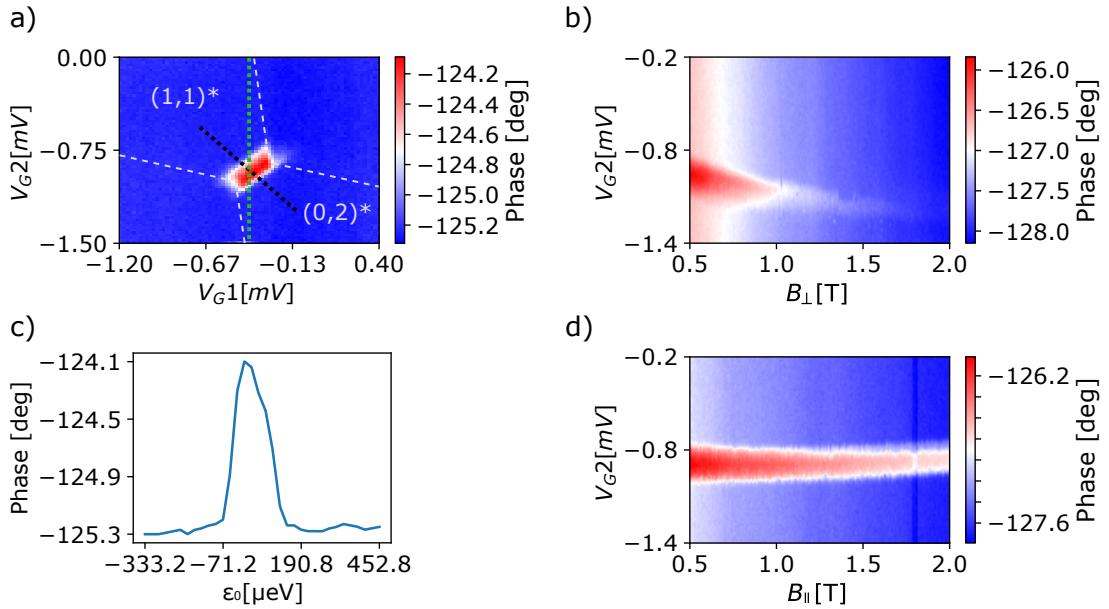


Figure 6.3: **Magnetic field dependence of the inter-dot phase response a** Same charge stability diagram plot shown in Figure 6.2d, with dashed white lines indicating the approximate dot to lead charge transitions. $(N_1, N_2)^*$ marks an equivalent DQD charge configuration. **b** Phase vs V_{G2} and magnetic field applied perpendicular to the sample plane ($B_\perp$), for V_{G1} fixed at the dashed green line in **a**. The inter-dot phase response vanishes in-between 1 and 1.5 T, probably due to a zero C_Q of the $T_-(1,1)$ state, which became the ground state for this B range. For each (V_{G2}, B) point, 2000 samples were taken with 880 kSa/s and averaged. The excitation signal power was set to $\sim -92\,dBm$ on the resonant circuit (-30 dBm at the UHFLI output), $f = f_{res} = 275.19\,MHz$, and the 4-th order low-pass filter time constant was set to 20 ms. **c** Phase vs detuning taken at the black dashed line in **a** for B=0 T. The line has the same direction coefficient as the black dashed line in Figure 6.2c, so the extracted α_{det} applies here. The points on the detuning line are calculated as $\epsilon_0 = \alpha_{det}(V_{Gdet} - V_{Gdet0})$, where V_{Gdet} is the gate voltage along the line. V_{Gdet0} marks the position of the maximum phase signal and substracting it from V_{Gdet} makes $\epsilon_0 = 0$ when the DQD charge levels align. The FWHM of the shown trace is $132.3\,\mu eV$. **d** Same as **b**, but with the magnetic field applied in the parallel direction.

To examine this, the magnetic field was swept while continuously taking the line scan, along the green dashed line in Figure 6.3a. The corresponding phase response versus V_{G2} and B scans are shown in Figure 6.3b and d, for the magnetic field direction applied perpendicular and parallel to the sample plane, respectively. In case the DQD is

doubly occupied, the increasing magnetic field should push the $T_{-}(1,1)$ state below the singlet states, as can be seen in Figure 2.9b, at the bottom. Since the measurement time, for every V_{G2} point (50 ms) was much longer than the relaxation time, the DQD was predominantly in the ground state during the measurement. Increasing magnetic field increases thus the probability of $T_{-}(1,1)$ state occupation, therefore lowering the quantum capacitance. Consequently the inter-dot signal vanished when $g\mu_B B$ became sizeably larger than t_c. Due to the similarity between the inter-dot evolution in Figure 6.3b and the one reported in [Mizuta *et al.*, 2017] (Figure 4.c.), it can be concluded that the system is in the slow relaxation regime (the excitation frequency f is much higher than relaxation rates) here and that $0.1 < \frac{k_B T}{2t_c} < 1$. Therefore, the procedure for t_c extraction, introduced above, can be applied here. From the FWHM of the line cut shown in Figure 6.3c, the tunnel coupling can be extracted to be $33\,\mu eV < t_c < 44\,\mu eV$ or $8\,GHz < t_c < 10.6\,GHz$. This means that the excitation signal frequency, which is in the hundreds of MHz, is indeed much lower than t_c **confirming thus the above already assumed adiabatic regime**. To confirm the origin of the vanishing inter-dot signal, the measurement was repeated, but now with the magnetic field applied in parallel to the sample. Due to the large g-factor anisotropy in Ge HWs [Watzinger *et al.*, 2016], a much smaller in-plane g-factor should result in a proportionally higher value of the magnetic field for which the inter-dot signal vanishes. This was confirmed by the data shown in Figure 6.3d, giving thus an additional evidence for the assumed mechanism.

A commonly used figure of merit of the measurement system is a SNR. Here, it is extracted according to the procedure reported in [West *et al.*, 2019]. For this the DQD gate voltages are set to the point at the inter-dot transition, marked with the black star in Figures 6.2b and d. Each of the 1000 samples of I and Q components of the reflected signal was averaged during the averaging time. This was repeated for the gate voltages set to the point away from the inter-dot (green star in Figures 6.2b and d). All other UHFLI parameters are same as above, apart from the low-pass filter bandwidth, which was set to 100 kHz here. The histogram of recorded I and Q samples, for the on and

off the inter-dot cases and for an integration time of 10 ms, is shown in Figure 6.2e. The difference between the mean value of the blobs in the green and black rectangles represents the signal while the blob radius correlates with the noise amplitude. The larger the radius, the higher the noise. The exact formula for the SNR calculation is:

$$SNR = \frac{Signal\ power}{Noise\ power} = \frac{\langle I_{ON} - I_{OFF} \rangle^2 + \langle Q_{ON} - Q_{OFF} \rangle^2}{SD[(I_{ON} - I_{OFF})^2 + (Q_{ON} - Q_{OFF})^2]} \tag{6.16}$$

where subscripts ON and OFF stand for IQ components recorded on and off the inter-dot transition respectively, $\langle \cdot \rangle$ symbolizes the average value and SD the standard deviation. The same measurement was performed for an integration time of 10, 20, 50 and 100 ms and the calculated SNRs are plotted in Figure 6.2f.

The same device was remeasured with a NbTiN superconducting planar inductor, instead of the copper one. The Q factor increased to ~ 230. The excitation signal amplitude needed to be decreased 10 times in order to avoid power broadening. Despite the lower excitation signal amplitude, the amplitude of the reflected signal change increased, due to the increased sensitivity. The noise slightly increased as well, keeping the SNR approximately the same as in the case with the copper coils. However, it should be also mentioned that the sample was thermally cycled and rebonded in order to replace the coil. This changed the sample characteristics, as concluded from the stability diagrams. Thus it is difficult to compare between the two cool-downs.

Conclusion

To have a sizeable difference between the occupation probabilities of the singlet and the $T_-(1,1)$ state, and therefore a high enough readout sensitivity (fidelity), the $T_-(1,1)$ state should be sizeably lower than the singlet state (consult Figure 2.9b, at the bottom), at the qubit readout point (around $\epsilon_0 = 0$). In other words, $g\mu_B B - t_c$ should be sizeably larger than $k_B T$. This occurs for a B field for which the inter-dot signal vanishes (consult Figure 6.3b). With an expected, out-of-plane, g-factor value of 2-3 in Ge HWs,

this further implies frequencies of the spin manipulation bursts f_{MW} in tens of GHz, which is too high. This issue could be addressed with a t_c reduction. An independent tunnel coupling control and thus its reduction, could be achieved with the middle gate electrode.

6.2.2 Sample ”MJ_5_S33”

To be able to tune the tunnel coupling and therefore reduce the necessary f_{MW} a middle gate was implemented in the next batch of samples. Apart from this, several fabrication steps were changed (as described in Section 3.3.1) to try to solve the small gate range problem occurring in samples like ”S228_111”.

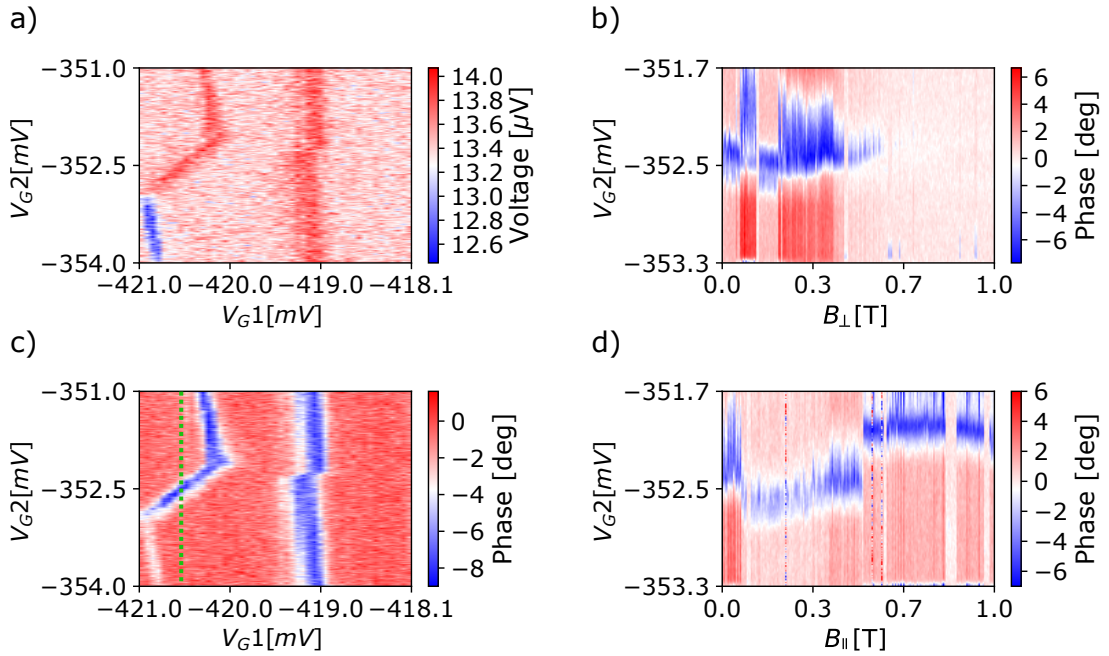


Figure 6.4: **Gate reflectometry data from the sample "MJ_5_S33"** The data presented here is recorded at the Grandpa Rudolph fridge with a base temperature of $\sim 30\,mK$. **a** Reflected signal amplitude versus V_{G1} and V_{G2} for an inter-dot transition at $B = 0\,T$. The middle gate voltage V_{Gm} was $3.2\,V$ and $V_{SD} \approx 0$. The excitation signal frequency was set to f=122.455 MHz and the power to -107 dBm (-45 dBm at the UHFLI output). The 4-th order UHFLI demodulator low-pass filter time constant was 1 μs. The ramp amplitude and duration were 3 mV and 1 ms respectively, while one vertical trace consists of 256 averaged scope shots, yielding a single vertical trace duration of 256 ms. The inter-dot in focus is on the left, while the right feature stems probably from some non-intentional nearby QD, capacitively coupled to the sensed gate G1. **c** The same scan as in **a**, measured as a phase of the reflected signal. **b** Phase vs V_{G2} and $B_\perp$ for the inter-dot line marked with the green dashed line in **c**. $V_{G1} = -420.58\,mV$, $V_{Gm} = 3.2\,V$ and $V_{SD} \approx 0$. The other measurement parameters are the same as for **a** apart from the ramp amplitude of 1.6 mV, the time constant of 5 μs and the 512 averaged scope shots (a single vertical trace recording time was 512 ms). The inter-dot phase response vanishes for $B \approx 0.7\,T$, presumably due to $T_-(1,1)$ becoming the ground state of the system, as explained above. **d** Same as in **b** but for the magnetic field applied in the parallel direction.

An example of a middle top gate sample is "MJ_5_S33". its layout can be seen in Figure 3.6a, while the stability diagram, showing a clear pattern of bias triangles can be seen in Figure 3.6b. Fabrication details can be found in Section 3. The particular fabrication steps that distinguish the top middle gate samples is described in Section 3.3.1.

The gate G1 was bonded to the resonant circuit consisting of two square NbTiN coils connected in series and C_p. One coil was made out of 20 and another out of 40 turns having a turn width and a turn separation both equal to 1 μm. They had a 460 and 570 μm outer diameter, with the inductances equal to $\sim$ 400 nH and $\sim$1600 nH respectively[1]. From the calculated total inductance of L$\approx$2000 nH and the measured resonant frequency of $f_{res} = 121.5\,MHz$, the parasitic capacitance is estimated to be $C_p \approx 0.86\,pF$. The Q factor is $\sim$240. The measurements shown in Figure 6.4 are performed in a so called ramping mode, explained in the following. A static V_{G2} was generated with the IVVI DAC. The AWG generated voltage ramp, with a 1 ms period, was superimposed to the DC V_{G2} value via the PCB bias tee. A consequential reflected wave response was acquired by sampling the UHFLI demodulated phase and amplitude with the UHFLI scope. The acquisition started with the high level of the trigger generated by the AWG at the begining of every ramp and lasted for the ramp duration time (1 ms). The acquired gate reflectometry response, corresponding to a single ramp is called a scope shot. A few hundred of scope shots were sequentially measured and averaged. After this, V_{G1} was set to a new value and the process was repeated yielding thus the next vertical trace. The UHFLI demodulator low-pass filter time constant (bandwidth) was set to a much smaller (higher) value than the ramp period (frequency), to avoid distortions in the measured signal. Meanwhile, the scope sampling rate was set to a value several times higher than the low-pass filter bandwidth to avoid aliasing. For the measurements shown in Figure 6.4, the sampling rate was set to 7.03 MHz yielding 7030 samples per 1 ms long scope shot. Additionally, every 20 adjacent points were averaged, resulting in 351 points in the vertical line traces in the above shown graphs.

A zero magnetic field gate reflectometry measurement of a representative inter-dot transition is shown in Figure 6.4a and c, measured in amplitude and phase, respectively. In both graphs, on the left, apart from the inter-dot transition, a lead to QD1 transition is visible as well. Also, another vertical feature appears around $V_{G2} = -419.0\,mV$.

[1] http://www.circuits.dk/calculator_planar_coil_inductor.htm

This is probably due to an unwanted QD formed nearby and capacitively coupled to G2. The applied signal power is lower compared to the experiment shown in Figure 6.2, but still the change between the signal minimum and maximum levels is larger here. This is mainly due to the superconducting inductors, even if $\alpha_1 \approx \alpha_2 \approx 0.4\,\frac{eV}{V}$ (measured from the bias triangle in a gate voltage area nearby) is smaller here. One can notice that the inter-dot phase response, in Figure 6.4b, vanishes at smaller magnetic field values than in Figure 6.3b. Assuming similar g-factors, this implies that a smaller tunnel coupling was achieved when applying a large positive middle gate voltage here. The smaller FWHM of the inter-dot phase response ($\sim 90\,\mu eV$) yields indeed a smaller t_c ($23\,\mu eV < t_c < 30\,\mu eV$ or $5.6\,GHz < t_c < 7.2\,GHz$) then extracted for "S228_111". The non vanishing inter-dot response in the control measurement in Figure 6.4d, supports the interpretation of a doubly occupied DQD in magnetic field.

In general this sample was very unstable, probably due to a random charge movements in the volume next to the DQD. The charge dynamics can be split into a faster one and a slower one. The faster one moves on a timescale which is faster than the duration of a single vertical trace in Figure 6.4b and d, causing a bluring effect. The slower one is characterized by a sudden charge movement followed by a steady state during several vertical line traces, causing a shifting effect. This instability prohibited tuning this device towards the qubit regime, despite the fact that smaller tunnel couplings were reached.

7 Conclusions

In order to perform low temperature transport measurements, reported in this thesis, we needed to develop a few parts of the used cryogenic setup. In addition to pre-installed DC lines, we equipped the probe (Section 4.1.1) with attenuated HF lines to control the dynamic properties of the measured samples. The DC lines were low-pass filtered and the HF lines attenuated, at different temperature stages, reducing thus the electron temperature to as low as 100 mK, at the sample stage. The measured samples (Si chips) were glued on the developed PCB sample holder and mounted at the bottom of the probe. The PCB served as a mechanical and electrical connection platform, precisely guiding the signals brought down by DC and HF lines, allowing thus to pin point each sample electrode by wire bonding. its design constraints were the uniformity of the HF lines (50 Ω matching), low crosstalk between the HF lines themselves and towards the DC lines, sensitive reflectometry readout and the compatibility with a wide range of samples and experiments. Since a sensitive reflectometry favours lower stray capacitance while lower cross talk prefers the opposite, the optimization route finished in two different PCB versions. The first one called ”Iron Man” has a smaller stray capacitance while the other one called ”Iron Kid” has a lower cross-talk and generally it is a bit better since it was designed as a second one.

Both of them consist of six copper layers, guiding 24 DC, 6 fast gate and 4 reflectometry HF lines. DC lines are additionally low-pass filtered to the kHz range with a single stage RC low-pass filters soldered on the top and bottom layers.

The PCB, together with the whole setup, was then used to perform transport and spin manipulation experiments on Ge HW DQDs, located on 6x6 mm^2 Si chips. Prior to the measurement, the chip surface was imaged with the SEM. This allowed to target and contact single HWs by means of e-beam writing and metal evaporation techniques. By applying the waveforms showed in Section 5, guided through the PCB HF lines, we demonstrated the two axis control of a single hole spin qubit, confined in a two gate Ge HW DQD. Very short manipulation times, reaching 3.5 ns for the π rotation, were observed. Fully electrical and very high manipulation frequencies were enabled by the intrinsically strong spin orbit coupling in Ge. In spite of the hole state character being predominantly heavy hole like, a relatively short average dephasing time of 130 ns was measured. Since this is the first qubit demonstration in Ge HWs, more experiments are needed in order to build the general knowledge about this, so far, non investigated system. In the first place to determine the exact spin rotation mechanism, to understand better the electric dipole spin resonance lines in Figures 5.3 and 5.4 and to investigate the mechanisms that limit the coherence. These experiments (e.g. Carl-Purcell-Meiboom-Gill experiment) require manipulation periods by far longer than 400 ns, which was the maximum duration for which a current signal could be still observed during the qubit experiment. Thus, a more sensitive readout mechanism is needed.

Due to high gate to dot coupling factors in Ge HWs, we decided to integrate a DQD gate into the resonant circuit for a gate reflectometry readout. From the inter-dot scans with increasing magnetic field, singlet and triplet states were distinguished, demonstrating spin sensing. The extracted integration time of $t_{int} \approx 2\,ms$, for $SNR = 1$, is only slightly higher then the one reported in [West *et al.*, 2019] in spite of having a 10 times higher signal, in the performed experiment. By implementing higher Q factor superconducting inductors, the measured signal increased even more, but the SNR stayed approximately the same, suggesting thus the sample as the main noise source. A few fabrication strategies have been tested with the goal of measuring the qubit with gate reflectometry. The output of the first one, including the native Si oxide removal

and etching steps, was a better sample stability, but a lower tuning range. The other one, with the addition of the middle gate, resulted in a larger tuning range but suffered from increased noise and instability, prohibiting thus to reach the qubit regime. In the future, the combination of a new wafer and etching techniques might allow to achieve both good stability and a large tuning range. Apart from the sample optimization, there is still room for improvement in terms of matching between R_{eff} and $Z_0 = 50\,\Omega$ and therefore boosting the sensitivity in Equation 6.10. Such a matching could be achieved with millikelvin compatible varactors or precisely designed fixed capacitors. Also, circulators, in order to reduce the cryogenic amplifier back-action and an amplifier with a better noise figure (like JPA or SQUID) could be installed to increase the signal even further.

In addition to supporting a sensitive and scalability friendly gate reflectometry readout, the combination of large α factors and the strong spin-orbit coupling, in Ge HWs, should allow good coupling to superconducting resonators, enabling thus a long distance spin to spin coupling. Furthermore, the possibility of pre-patterned growth of HW arrays [Gao *et al.*, 2020], could bring a two-qubit gate implementation based on nearest neighbour coupling and scale-up schemes, closer to reality.

All in all, by demonstrating the possibility to host a single qubit and offering promising ways towards two-qubit gates and coupling to superconductors, holes confined in Ge HWs might be a good candidate for scalable spin qubits.

Bibliography

[Ahmed *et al.*, 2018] I. Ahmed, J.A. Haigh, S. Schaal, S. Barraud, Y. Zhu, C. Lee, M. Amado, J.W.A Robinson, A. Rossi, J.J.L Morton, and M.F.G. Zalba, "Radio-Frequency Capacitive Gate-Based Sensing," *Phys. Rev. A*, 10:014018, 2018.

[Ares *et al.*, 2013] N. Ares, G. Katsaros, V. N. Golovach, J. J. Zhang, A. Prager, L. I. Glazman, O. G. Schmidt, and S. De Franceschi, "SiGe quantum dots for fast hole spin Rabi oscillations," *Appl. Phys. Lett.*, 103:263113, 2013.

[Arute *et al.*, 2019] F. Arute, K. Arya, R. Babbush, D. Bacon, J. C. Bardin, R. Barends, R. Biswas, S. Boixo, F. G. S. L. Brandao, D. A. Buell, B. Burkett, Y. Chen, Z. Chen, B. Chiaro, R. Collins, W. Courtney, A. Dunsworth, E. Farhi, B. Foxen, A. Fowler, C. Gidney, M. Giustina, R. Graff, K. Guerin, S. Habegger, M. P. Harrigan, M. J. Hartmann, A. Ho, M. Hoffmann, T. Huang, T. S. Humble, S. V. Isakov, E. Jeffrey, Z. Jiang, D. Kafri, K. Kechedzhi, J. Kelly, P. V. Klimov, S. Knysh, A. Korotkov, F. Kostritsa, D. Landhuis, M. Lindmark, E. Lucero, D. Lyakh, S. Mandrà, J. R. McClean, M. McEwen, A. Megrant, X. Mi, K. Michielsen, M. Mohseni, J. Mutus, O. Naaman, M. Neeley, C. Neill, M. Y. Niu, E. Ostby, A. Petukhov, J. C. Platt, C. Quintana, E. G. Rieffel, P. Roushan, N. C. Rubin, D. Sank, K. J. Satzinger, V. Smelyanskiy, K. J. Sung, M. D. Trevithick, A. Vainsencher, B. Villalonga, T. White, Z. J. Yao, P. Yeh, A. Zalcman, H. Neven, and J. M. Martinis, "Quantum supremacy using a programmable superconducting processor," *Nature*, 574(7779):505–510, 2019.

[Ashoori *et al.*, 1992] R. C. Ashoori, H. L. Stormer, J. S. Weiner, L. N. Pfeiffer, S. J. Pearton, K. W. Baldwin, and K. W. West, "Single-electron capacitance spectroscopy

of discrete quantum levels," *Phys. Rev. Lett.*, 68:3088, 1992.

[Barends *et al.*, 2014] R. Barends, J. Kelly, A. Megrant, A. Veitia, D. Sank, E. Jeffrey, T. C. White, J. Mutus, A. G. Fowler, B. Campbell, Y. Chen, Z. Chen, B. Chiaro, A. Dunsworth, C. Neill, P. O′Malley, P. Roushan, A. Vainsencher, J. Wenner, A. N. Korotkov, A. N. Cleland, and John M. Martinis, "Superconducting quantum circuits at the surface code threshold for fault tolerance," *Nature*, 508(7497):500–503, 2014.

[Bluhm *et al.*, 2010] H. Bluhm, S. Foletti, D. Mahalu, V. Umansky, and A. Yacoby, "Enhancing the Coherence of a Spin Qubit by Operating it as a Feedback Loop That Controls its Nuclear Spin Bath," *Phys. Rev. Lett.*, 105(21):216803, 2010.

[Borjans *et al.*, 2020] F. Borjans, X. G. Croot, X. Mi, M. J. Gullans, and J. R. Petta, "Resonant microwave-mediated interactions between distant electron spins," *Nature*, 577(7789):195–198, 2020.

[Brauns *et al.*, 2016] M. Brauns, J. Ridderbos, A. Li, E. P. A. M. Bakkers, and F. A. Zwanenburg, "Electric-field dependent g-factor anisotropy in Ge-Si core-shell nanowire quantum dots," *Phys. Rev. B*, 93:121408(R), 2016.

[Brown *et al.*, 2011] K. R. Brown, A. C. Wilson, Y. Colombe, C. Ospelkaus, A. M. Meier, E. Knill, D. Leibfried, and D. J. Wineland, "Single-qubit-gate error below 10^{-4} in a trapped ion," *Phys. Rev. A*, 84(3):030303, 2011.

[Cassidy *et al.*, 2007] M. C. Cassidy, A. S. Dzurak, R. G. Clark, K. D. Petersson, I. Farrer, D. A. Ritchie, and C. G. Smith, "Single shot charge detection using a radio-frequency quantum point contact," *Appl. Phys. Lett.*, 91:222104, 2007.

[Colless *et al.*, 2013] J. I. Colless, A.C. Mahoney, J.M. Hornibrook, A.C. Doherty, H. Lu, A.C. Gossard, and D.J. Reilly, "Dispersive Readout of a Few-Electron Double Quantum Dot with Fast rf Gate Sensors," *Phys. Rev. Lett.*, 110:046805, 2013.

[Crippa *et al.*, 2019] A. Crippa, R. Ezzouch, A. Aprá, A. Amisse, R. Laviéville, L. Hutin, B. Bertrand, M. Vinet, M. Urdampilleta, T. Meunier, M. Sanquer, X. Jehl, R. Maurand,

and S. De Franceschi, "Gate-reflectometry dispersive readout and coherent control of a spin qubit in silicon," *Nature Communications*, 10:2776, 2019.

[Danon and Rudner, 2014] J. Danon and M. S. Rudner, "Multilevel Interference Resonances in Strongly Driven Three-Level Systems," *Phys. Rev. Lett.*, 113:247002, 2014.

[DiVincenzo, 2000] David P. DiVincenzo, "The Physical Implementation of Quantum Computation," *Progress of Physics*, 48:771–783, 2000.

[Dobrowolska *et al.*, 1982] M. Dobrowolska, H.D. Drew, J.K. Furdyna, T. Ichiguchi, A. Witowski, and P.A. Wolff, "Electric-Dipole Spin Resonance of Bound Electronic States in $Cd_{1-x}Mn_xSe$," *Phys. Rev. Lett.*, 49:845, 1982.

[Duty *et al.*, 2005] T. Duty, G. Johansson, K. Bladh, D. Gunnarsson, C. Wilson, and P. Delsing, "Observation of Quantum Capacitance in the Cooper-Pair Transistor," *Phys. Rev. Lett.*, 95:206807, 2005.

[Engel *et al.*, 2004] H.-A. Engel, V. N. Golovach, D. Loss, L. M. K. Vandersypen, J. M. Elzerman, R. Hanson, and L. P. Kouwenhoven, "Measurement Efficiency and n-Shot Readout of Spin Qubits," *Phys. Rev. Lett.*, 93(10):106804, 2004.

[Fischer *et al.*, 2008] J. Fischer, W. A. Coish, D. V. Bulaev, and D. Loss, "Spin decoherence of a heavy hole coupled to nuclear spins in a quantum dot," *Phys. Rev. B*, 78:155329, 2008.

[Fowler *et al.*, 2012] A.G. Fowler, M. Mariantoni, J.M. Martinis, and A.N. Cleland, "Surface codes: Towards practical large-scale quantum computation," *Phys. Rev. A*, 86:032324, 2012.

[Frake *et al.*, 2015] J.C. Frake, S. Kano, C. Ciccarelli, J. Griffiths, M. Sakamoto, T. Teranishi, Y. Majima, C.G. Smith, and M.R. Buitelaar, "Radio-frequency capacitance spectroscopy of metallic nanoparticles," *Scientific Reports*, 5:10858, 2015.

[Gao *et al.*, 2020] F. Gao, J.H. Wang, H. Watzinger, H. Hu, M.J. Rančić, J.Y. Zhang,

T. Wang, Y. Yao, G.L. Wang, J. Kukučka, L. Vukušić, C. Klöffel, D. Loss, F. Liu, G. Katsaros, and J.J. Zhang, "Site-Controlled Uniform Ge/Si Hut Wires with Electrically Tunable Spin-Orbit Coupling," *Advanced Materials*, 32:1906523, 2020.

[Golovach *et al.*, 2006] V. N. Golovach, M. Borhani, and D. Loss, "Electric-dipole-induced spin resonance in quantum dots," *Phys. Rev. B*, 74:165319, 2006.

[Hanson *et al.*, 2007] R. Hanson, L. P. Kouwenhoven, J. R. Petta, S. Tarucha, and L. M. K. Vandersypen, "Spins in few-electron quantum dots," *Rev. Mod. Phys.*, 79(0):1217–1265, 2007.

[Hao *et al.*, 2010] X.-J. Hao, T. Tu, G. Cao, C. Zhou, H.-O. Li, G.-C. Guo, W. Y. Fung, Z. Ji, G.-P. Guo, and W. Lu, "Strong and Tunable Spin-Orbit Coupling of One-Dimensional Holes in Ge/Si Core/Shell Nanowires," *Nano Lett.*, 10:2956–2960, 2010.

[Hayashi *et al.*, 2003] T. Hayashi, T. Fujisawa, H. D. Cheong, Y. H. Jeong, and Y. Hirayama, "Coherent Manipulation of Electronic States in a Double Quantum Dot," *Phys. Rev. Lett.*, 91(22):226804, 2003.

[Hendrickx *et al.*, 2020] N.W. Hendrickx, D.P. Franke, A. Sammak, G. Scappucci, and M. Veldhorst, "Fast two-qubit logic with holes in germanium," *Nature*, 577:487–491, 2020.

[Henrik *et al.*, 2006] B. Henrik, S. Kafanov, T. Duty, S. Kubatkin, and P. Delsing, "An ultrasensitive radio-frequency single-electron transistor working up to 4.2K," *J. Appl. Phys.*, 100:114321, 2006.

[Higginbotham *et al.*, 2014] A. P. Higginbotham, T. W. Larsen, J. Yao, H. Yan, C. M. Lieber, C. M. Marcus, and F. Kuemmeth, "Hole Spin Coherence in a Ge/Si Heterostructure Nanowire," *Nano Lett.*, 14:3582–3586, 2014.

[Hu *et al.*, 2012] Y. J. Hu, F. Kuemmeth, C. M. Lieber, and C. M. Marcus, "Hole spin

relaxation in Ge-Si core-shell nanowire qubits," *Nature Nanotechnology*, 7:47–50, 2012.

[Hutin *et al.*, 2018] L. Hutin, B. Bertrand, R. Maurand, A. Crippa, M. Urdampilleta, Y.J. Kim, A. Amisse, H. Bohuslavskyi, L. Bourdet, S. Barraud, X. Jeh, Y.-M. Niquet, M. Sanquer, C. Bäuerle, T. Meunier, S. De Franceschi, and M. Vinet, "Si MOS technology for spin-based quantum computing," In *48th European Solid-State Device Research Conference (ESSDERC)*, pages 12–17, Dresden, 2018.

[Kane, 1998] B. E. Kane, "A silicon-based nuclear spin quantum computer," *Nature*, 393(6681):133–137, 1998.

[Kastner, 1992] M. A. Kastner, "The single-electron transistor," *Rev. of Modern Phys.*, 64:849, 1992.

[Kato *et al.*, 2003] Y. Kato, R.C. Myers, D.C. Driscoll, A.C. Gossard, J. Levy, and Awschalom D.D., "Gigahertz electron spin manipulation using voltage-controlled g-tensor modulation," *Science*, 299:1201–1204, 2003.

[Katsaros *et al.*, 2011] G. Katsaros, V. N. Golovach, P. Spathis, N. Ares, M. Stoffel, F. Fournel, O. G. Schmidt, L. I. Glazman, and S. De Franceschi, "Observation of Spin-Selective Tunneling in SiGe Nanocrystals," *Phys. Rev. Lett.*, 107:246601, 2011.

[Keith *et al.*, 2019] D. Keith, M. G. House, M. B. Donnelly, T. F. Watson, B. Weber, and M. Y. Simmons, "Single-Shot Spin Readout in Semiconductors Near the Shot-Noise Sensitivity Limit," *Phys. Rev. X*, 9(4):041003, 2019.

[Kloeffel *et al.*, 2017] C. Kloeffel, M. J. Rančić, and D. Loss, "Direct Rashba spin-orbit interaction in Si and Ge nanowires with different growth directions," *arXiv:1712.03476*, 2017.

[Koppens *et al.*, 2007] F. H. L. Koppens, D. Klauser, W. A. Coish, K. C. Nowack, L. P. Kouwenhoven, D. Loss, and L. M. K. Vandersypen, "Universal Phase Shift

and Nonexponential Decay of Driven Single-Spin Oscillations," *Phys. Rev. Lett.*, 99(10):106803, 2007.

[Koppens *et al.*, 2006] F.H.L. Koppens, C. Buizert, K.J. Tielrooij, I.T. Vink, K.C. Nowack, T. Meunier, L.P. Kouwenhoven, and L.M.K. Vandersypen, "Driven coherent oscillations of a single electron spin in a quantum dot," *Nature*, 442:766–771, 2006.

[Laird *et al.*, 2009] E. A. Laird, C. Barthel, E. I. Rashba, C. M. Marcus, M. P. Hanson, and A. C. Gossard, "A new mechanism of electric dipole spin resonance: hyperfine coupling in quantum dots," *Semiconductor Science and Technology*, 24(6):064004, 2009.

[Lamb *et al.*, 2016] C. I.D. Lamb, J.I. Colless, J.M. Hornibrook, S. J. Pauka, S. J. Waddy, M. K. Frechtling, and D. J. Reilly, "An FPGA-based instrumentation platform for use at deep cryogenic temperatures," *Review of Scientific Instruments*, 87:014701, 2016.

[Levitt, 2001] Malcolm H. Levitt, *Basics of Nuclear Magnetic Resonance*, Wiley, 2001.

[Loss and DiVincenzo, 1998] D. Loss and D. P. DiVincenzo, "Quantum computation with quantum dots," *Phys. Rev. A*, 57:120, 1998.

[Lu *et al.*, 2005] W. Lu, J. Xiang, B. P. Timko, Y. Wu, and C. M. Lieber, "One-dimensional hole gas in germanium/silicon nanowire heterostructures," *PNAS*, 102:10046–10051, 2005.

[Malinowski *et al.*, 2017] F. K. Malinowski, F. Martins, P. D. Nissen, E. Barnes, L. Cywiński, M. S. Rudner, S. Fallahi, G. C. Gardner, M. J. Manfra, C. M. Marcus, and F. Kuemmeth, "Notch filtering the nuclear environment of a spin qubit," *Nature Nanotechnology*, 12(1):16–20, 2017.

[Maurand *et al.*, 2016] R. Maurand, X. Jehl, D. Kotekar-Patil, A. Corna, H. Bohuslavskyi, R. Laviéville, L. Hutin, S. Barraud, M. Vinet, M. Sanquer, and

S. De Franceschi, "A CMOS silicon spin qubit," *Nature Communications*, 7:13575, 2016.

[Mizuta *et al.*, 2017] R. Mizuta, R.M. Otxoa, A.C. Betz, and M.F. Gonzalez-Zalba, "Quantum and tunneling capacitance in charge and spin qubits," *Phys. Rev. B*, 95:045414, 2017.

[Mo *et al.*, 1990] Y.-W. Mo, D. E. Savage, B. S. Swartzentruber, and M. G. Lagally, "Kinetic pathway in Stranski-Krastanov growth of Ge on Si(001)," *Phys. Rev. Lett.*, 65:1020, 1990.

[Muhonen *et al.*, 2014] J. T. Muhonen, J. P. Dehollain, A. Laucht, F. E. Hudson, R. Kalra, T. Sekiguchi, K. M. Itoh, D. N. Jamieson, J. C. McCallum, A. S. Dzurak, and A. Morello, "Storing quantum information for 30 seconds in a nanoelectronic device," *Nature Nanotechnology*, 9:986–991, 2014.

[Nowack *et al.*, 2011] K. C. Nowack, M. Shafiei, M. Laforest, G. E. D. K. Prawiroatmodjo, L. R. Schreiber, C. Reichl, W. Wegscheider, and L. M. K. Vandersypen, "Single-Shot Correlations and Two-Qubit Gate of Solid-State Spins," *Science*, 333(6047):1269, 2011.

[O'Brien *et al.*, 2009] J.L. O'Brien, A. Furusawa, and J. Vučković, "Photonic quantum technologies," *Nature Photonics*, 3:687–695, 2009.

[Ono *et al.*, 2002] K. Ono, D. G Austing, Y Tokura, and S. Tarucha, "Current Rectification by Pauli Exclusion in a Weakly Coupled Double Quantum Dot System," *Science*, 297:1313–1317, 2002.

[Pakkiam *et al.*, 2018] P. Pakkiam, A. V. Timofeev, M. G. House, M. R. Hogg, T. Kobayashi, M. Koch, S. Rogge, and M. Y. Simmons, "Single-Shot Single-Gate rf Spin Readout in Silicon," *Phys. Rev. X*, 8(4):041032, 2018.

[Park *et al.*, 2016] J. Park, Y. Ahn, J. A. Tilka, K. C. Sampson, D. E. Savage, J. R. Prance, C. B. Simmons, M. G. Lagally, S. N. Coppersmith, M. A. Eriksson, M. V.

Holt, and P. G. Evans, "Electrode-stress-induced nanoscale disorder in Si quantum electronic devices," *APL Mater.*, 4:066102, 2016.

[Persson *et al.*, 2010] F. Persson, C. M. Wilson, M. Sandberg, and P. Delsing, "Fast readout of a single Cooper-pair box using its quantum capacitance," *Phys. Rev. B*, 82:134533, 2010.

[Petersson *et al.*, 2012] K.D. Petersson, L.W. McFaul, M.D. Schroer, M. Jung, J.M. Taylor, A.A Houck, and J.R. Petta, "Circuit quantum electrodynamics with a spin qubit," *Nature*, 490:380–383, 2012.

[Petersson *et al.*, 2010] K.D. Petersson, C. G. Smith, D. Anderson, P. Atkinson, G. A. C. Jones, and D. A. Ritchie, "Charge and Spin State Readout of a Double Quantum Dot Coupled to a Resonator," *Nano Lett.*, 10(8):2789–2793, 2010.

[Petta *et al.*, 2005] J. R. Petta, A. C. Johnson, J. M. Taylor, E. A. Laird, A. Yacoby, M. D. Lukin, C. M. Marcus, M. P. Hanson, and A. C. Gossard, "Coherent manipulation of coupled electron spins in semiconductor quantum dots," *Science*, 309:2180–2184, 2005.

[Pioro-Ladrière *et al.*, 2008] M. Pioro-Ladrière, T. Obata, Y. Tokura, Y.-S. Shin, T. Kubo, K. Yoshida, T. Taniyama, and S. Tarucha, "Electrically driven single-electron spin resonance in a slanting Zeeman field," *Nature Physics*, 4:776–779, 2008.

[Pla *et al.*, 2012] J. J. Pla, K. Y. Tan, J. P. Dehollain, W. H. Lim, J. J. L. Morton, D. N. Jamieson, Dzurak A. S., and A. Morello, "A single-atom electron spin qubit in silicon," *Nature*, 489:541–545, 2012.

[Reilly *et al.*, 2007] D. J. Reilly, C. M. Marcus, M. P. Hanson, and A. C. Gossard, "Fast single-charge sensing with a rf quantum point contact," *Appl. Phys. Lett.*, 91:162101, 2007.

[Schaal *et al.*, 2020] S. Schaal, I. Ahmed, J. A. Haigh, L. Hutin, B. Bertrand, S. Barraud, M. Vinet, C. M. Lee, N. Stelmashenko, J. W. A. Robinson, J. Y. Qiu, H. S.

Gourgy, I. Siddiqi, M. F. G. Zalba, and J. J. L. Morton, “Fast Gate-Based Readout of Silicon Quantum Dots Using Josephson Parametric Amplification,” *Phys. Rev. Lett.*, 124:067701, 2020.

[Schoelkopf *et al.*, 1998] R. J. Schoelkopf, P. Wahlgren, A. A. Kozhevnikov, P. Delsing, and Prober D. E., “The Radio-Frequency Single-Electron Transistor (RF-SET): A Fast and Ultrasensitive Electrometer,” *Science*, 280(5367):1238–1242, 1998.

[Shor, 1994] P.W. Shor, “Algorithms for quantum computation: discrete logarithms and factoring,” In *Proceedings 35th Annual Symposium on Foundations of Computer Science*, 1994.

[Stehlik *et al.*, 2014] J. Stehlik, M. D. Schroer, M. Z. Maialle, M. H. Degani, and J. R. Petta, “Extreme Harmonic Generation in Electrically Driven Spin Resonance,” *Phys. Rev. Lett.*, 112:227601, 2014.

[Takeda *et al.*, 2016] K. Takeda, J. Kamioka, T. Otsuka, J. Yoneda, T. Nakajima, M.R. Delbecq, S. Amaha, G. Allison, T. Kodera, S. Oda, and S. Tarucha, “A fault-tolerant addressable spin qubit in a natural silicon quantum dot,” *Sci. Adv.*, 2(8):e1600694, 2016.

[Urdampilleta *et al.*, 2019] M. Urdampilleta, D. J. Niegemann, E. Chanrion, B. Jadot, C. Spence, P.-A. Mortemousque, C. Bäuerle, L. Hutin, B. Bertrand, S. Barraud, R. Maurand, M. Sanquer, X. Jehl, S. De Franceschi, M. Vinet, and T. Meunier, “Gate-based high fidelity spin readout in a CMOS device,” *Nature Nanotechnology*, 14(8):737–741, 2019.

[van den Berg *et al.*, 2013] J. W. G. van den Berg, S. Nadj-Perge, V. S. Pribiag, S. R. Plissard, E. P. A. M. Bakkers, S. M. Frolov, and L. P. Kouwenhoven, “Fast spin-orbit qubit in an Indium Antimonide nanowire,” *Phys. Rev. Lett.*, 1110:066806, 2013.

[van der Wiel *et al.*, 2002] W. G. van der Wiel, S. De Franceschi, J. M. Elzerman, T. Fujisawa, S. Tarucha, and L. P. Kouwenhoven, “Electron transport through double quantum dots,” *Rev. Mod. Phys.*, 75(1):1–22, 2002.

[van Wees *et al.*, 1988] B. J. van Wees, H. van Houten, C. W. J. Beenakker, J. G. Williamson, L. P. Kouwenhoven, D. van der Marel, and C. T. Foxon, "Quantized conductance of point contacts in a two-dimensional electron gas," *Phys. Rev. Lett.*, 60:848, 1988.

[Veldhorst *et al.*, 2015] M. Veldhorst, C. H. Yang, J. C. C. Hwang, W. Huang, J. P. Dehollain, J. T. Muhonen, S. Simmons, A. Laucht, F. E. Hudson, K. M. Itoh, A. Morello, and A. S. Dzurak, "A two-qubit logic gate in silicon," *Nature*, 526:410–414, 2015.

[Vukušić, 2018] L. Vukušić, *Charge sensing and spin relaxation times of holes in Ge hut wires*, PhD thesis, IST Austria, Klosterneuburg, Austria, 2018.

[Vukušić *et al.*, 2018] L. Vukušić, J. Kukučka, H. Watzinger, J.M. Milem, F. Schäffler, and G. Katsaros, "Single-Shot Readout of Hole Spins in Ge," *Nano Lett.*, 18(11):7141–7145, 2018.

[Waldherr *et al.*, 2014] G. Waldherr, Y. Wang, S. Zaiser, M. Jamali, T. Schulte-Herbrüggen, H. Abe, T. Ohshima, J. Isoya, J. F. Du, P. Neumann, and J. Wrachtrup, "Quantum error correction in a solid-state hybrid spin register," *Nature*, 506(7487):204–207, 2014.

[Wang *et al.*, 2019] Z. Wang, E. Marcellina, A.R. Hamilton, S. Rogge, J. Salfi, and D. Culcer, "Suppressing charge-noise sensitivity in high-speed Ge hole spin-orbit qubits," *arXiv:1911.11143*, 2019.

[Watson *et al.*, 2018] T. F. Watson, S. G. J. Philips, E. Kawakami, D. R. Ward, P. Scarlino, M. Veldhorst, D. E. Savage, M. G. Lagally, Mark Friesen, S. N. Coppersmith, M. A. Eriksson, and L. M. K. Vandersypen, "A programmable two-qubit quantum processor in silicon," *Nature*, 555(7698):633–637, 2018.

[Watzinger, 2018] H. Watzinger, *Ge hut wires - from growth to hole spin resonance*, PhD thesis, IST Austria, Klosterneuburg, Austria, 2018.

[Watzinger *et al.*, 2014] H. Watzinger, M. Glaser, J. J. Zhang, I. Daruka, and

F. Schäffler, "Influence of composition and substrate miscut on the evolution of 105-terminated in-plane SiGe quantum wires on Si(001)," *APL Mater.*, 2:076102, 2014.

[Watzinger *et al.*, 2016] H. Watzinger, C. Kloeffel, L. Vukušić, M. D. Rossell, V. Sessi, J. Kukučka, R. Kirchschlager, E. Lausecker, A. Truhlar, M. Glaser, A. Rastelli, A. Fuhrer, D. Loss, and G. Katsaros, "Heavy-Hole States in Germanium Hut Wires," *Nano Lett.*, 16:6879–6885, 2016.

[Watzinger *et al.*, 2018] H. Watzinger, J. Kukučka, L. Vukušić, F. Gao, T. Wang, F. Schäffler, J.J. Zhang, and G. Katsaros, "A germanium hole spin qubit," *Nature Communications*, 9(1):3902, 2018.

[West *et al.*, 2019] A. West, B. Hensen, A. Jouan, T. Tanttu, C.H. Yang, A. Rossi, M.F.G. Zalba, F. Hudson, A. Morello, D.J. Reilly, and A.S. Dzurak, "Gate-based single-shot readout of spins in silicon," *Nature Nanotechnology*, 14:437–441, 2019.

[Yakimov *et al.*, 2006] A. I. Yakimov, A. V. Dvurechenskii, Nikiforov A. I., A. A. Bloshkin, A. V. Nenashev, and Volodin V. A., "Electronic states in Ge/Si quantum dots with type-II band alignment initiated by space-charge spectroscopy," *Phys. Rev. B*, 73:115333, 2006.

[Yoneda *et al.*, 2014] J. Yoneda, T. Otsuka, T. Nakajima, T. Takakura, T. Obata, M. Pioro-Ladrière, H. Lu, C.J. Palmstrøm, A.C. Gossard, and S. Tarucha, "Fast Electrical Control of Single Electron Spins in Quantum Dots with Vanishing Influence from Nuclear Spins," *Phys. Rev. Lett.*, 113:267601, 2014.

[Yoneda *et al.*, 2017] J. Yoneda, K. Takeda, T. Otsuka, T. Nakajima, M. R. Delbecq, G. Allison, T. Honda, T. Kodera, S. Oda, Y. Hoshi, N. Usami, K. M. Itoh, and S. Tarucha, "A quantum-dot spin qubit with coherence limited by charge noise and fidelity higher than 99.9%," *Nature Nanotechnology*, 13:102–106, 2017.

[Zajac *et al.*, 2018] D. M. Zajac, A. J. Sigillito, M. Russ, F. Borjans, J. M. Taylor,

G. Burkard, and J. R. Petta, “Resonantly driven CNOT gate for electron spins,” *Science*, 359(6374):439–442, 2018.

[Zalba *et al.*, 2015] M.F.G Zalba, S. Barraud, A.J. Ferguson, and A.C. Betz, “Probing the limits of gate-based charge sensing,” *Nature Communications*, 6:6084, 2015.

[Zhang *et al.*, 2012] J. J. Zhang, G. Katsaros, F. Montalenti, D. Scopece, R. O. Rezaev, C. Mickel, B. Rellinghaus, L. Miglio, S. De Franceschi, A. Rastelli, and O. G. Schmidt, “Monolithic Growth of Ultrathin Ge Nanowires on Si(001),” *Phys. Rev. Lett.*, 109:085502, 2012.

[Zheng *et al.*, 2019] G. Zheng, N. Samkharadze, M.L. Noordam, N. Kalhor, D. Brousse, A. Sammak, G. Scappucci, and Vandersypen L.M.K, “Rapid gate-based spin read-out in silicon using an on-chip resonator,” *Nature Nanotechnology*, 14:742–746, 2019.

A Appendix 1

A.1 PCB elements

A.1.1 PCB components

Resistors By comparing their characteristics at room temperature and at the fridge base temperature (approximately 30 mK) we found out that the resistance of this resistors do not change, so they are fine to use:

- 1 kΩ RR0816P-102-B-T5
- 10 kΩ MMU01020C1002FB300
- 1.8 MΩ MMU01020C1804FB300

It turned out that checking PCB components at 4 K is not good enough, they really need to be checked at the fridge base temperature. For example, 10 kΩ RG1005P-103-B-T5 resistors were turning superconductive below 1 K. This caused us quite some problems and it took a while until we figured it out. The resistors we use the most are the 10 kΩ and the 1.8 MΩ from Vishay. They are of MELF (Metal Electrode Leadless Face) type and therefore have better long term stability, reliability and resistance to temperature cycling, in comparison to the standard SMD resistors. Apart from the checked ones we also use other components without checking them, but they come from the same

family, for example:

- R=510 kΩ(MMU01020C5100FB300)
- R=2 MΩ (MMU01020C2004FB300) from Vishay.

Capacitors The same test we performed also for a few different capacitors and found out that 10 nF C0805X103J5GACAUTO from Kemet does not change behavior between room and base temperature. its dielectric is of C0G (NP0) type and therefore has a very small temperature coefficient. The negative side of the C0G ceramic is its low capacitance density, thus higher values than 10 nF in the 0805 casing could not be found. Therefore, for higher capacitance we have chosen 220 nF VJ0805Y224KCXAJ with X7R dielectric. Such a dielectric allows a much higher capacitance for the same dimensions, but according to [Lamb *et al.*, 2016] the capacitance drops by around 50$\%$ at liqiud nitrogen temperature, while the equivalent series resistance stays approximately the same. Consequently for a 220 nF room temperature capacitance, we can still expect a value considerably higher than 10 nF at low temperature. Similarly like for resistors, we use the following non tested capacitors:

- C=1.5 nF from Kemet (C0805X152J5GACAUTO)
- C=220 pF from Kemet (C0805X221J1GACAUTO)

An important parameter of a capacitor is also its self resonant frequency (SRF), especially in the case of decoupling capacitors for high-frequency signals, used on Iron Kid PCB. The decoupling capacitors should maintain a low impedance from MHz (control pulses) up to GHz (spin manipulation bursts). Since the capacitive reactance is $Xc = \frac{1}{j2\pi fC}$, where f is the frequency, for achieving a low impedance at low frequencies the capacitance value needs to be high enough. For maintaing a low impedance at GHz frequencies the self-resonant frequency should be high as well, because above the self-resonant frequency the capacitor behaves as an inductor. Since high value capacitors typically have low SRF[1], a compromise was made and 220 pF capacitors

[1] http://ksim.kemet.com/Ceramic/CeramicCapSelection.aspx

are chosen for typical decoupling capacitors.

Inductors Choosing a proper inductor is important for the reflectometry sensitivity. An inductor should have as high as possible SRF (as further away as possible from the operating frequency) and a high quality factor (Q factor). There are two types of inductors used regularly in the community. Those are, already mentioned, copper SMD inductors and planar superconducting inductors. Regarding the SMD version, the inductors with an inductance value in between 100 and 1200 nH satisfy best the criteria amongst the ones offered on the market. The common parameter of all used SMD inductors is a non-ferrite ceramic core because of high magnetic fields required in spin qubit experiments. In addition losses in ferrites reduce the Q factor. So, here we typically used SMD inductors from the Coilcraft 1206CS series, with values ranging from 180 to 1200 nH. The 1206CS series seem to have a good balance between a high enough inductance value while having still a high Q factor and SRF in comparison to other inductors from Coilcraft. It is worth noting that still better inductors might exist, like those in the Coilcraft 0805HP series which have up to 10% higher Q factors and SRFs, according to the datasheet. In general, off-the-shelf SMD inductors in such an inductance range have Q factors limited to below 100, so to go towards higher Q factors we needed to switch to superconducting inductors anyhow.

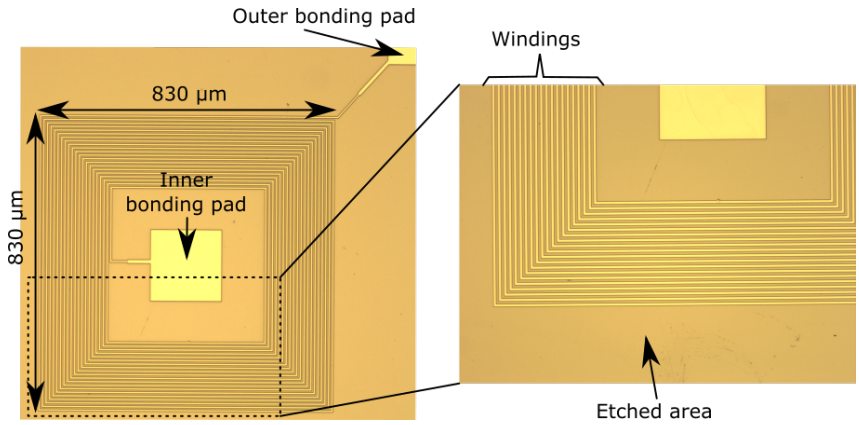


Figure A.1: **Optical microscope image of a square coil.** It consists of 20 windings, each of them 5 μm in width and separated by 5 μm from each other. This is one out of eight coils on the chip glued at the bottom of the Iron Kid PCB shown in Figure 4.12b.

Since their resistance vanishes below the critical temperature, superconducting inductors offer better quality factors. Because they are not off-the-shelf components we fabricated them as planar chip coils. Fabrication is done by etching the electron beam lithography defined space in between the coil windings, out of the 100 nm thick NbTiN film deposited on the Si chip. The example of a fabricated inductor can be seen in Figure A.1. The reason of using the NbTiN, for the coil material, is its high magnetic field resiliance required for spin experiments. We measured a higher than 2 T magnetic field resiliance for out-of-plane fields, at the fridge base temperature, for such a coil.

We also measured the loaded Q factor of a reflectometry circuit with the NbTiN and SMD inductors and found that the Q factor increases 2 to 10 times with the NbTiN ones. As this was one of the first fabricated chips, there is still a room for improvement regarding the optimization of the NbTiN coil fabrication recipe. The parameters that could be altered are the coil shapes (e.g a circle instead of a square), line width and the separation between windings. Also, etching Si in between the windings or suspending the whole coil in the air in order to reduce the amount of electric field in Si, which is more lossy than the vacuum, might be considered.

SMP connectors Those are ”thread free”, $>$20 GHz connectors, which even allow a slight radial misalignment to the female counterparts mounted on the PCB. In combination with a smaller footprint size they are much better for limited space then bulky SMA connectors. The SMD version of such a connector saves PCB space on layers beneath it in comparison to its trough hole pin version. But the maximum amount of the disengagement force is then limited by the integrity of the copper PCB layer the connector is mounted on. We have chosen the SMD version with the minimum disengagement force of 2.2 N (19S141-40ML5).

A.1.2 RC filters

To decrease the noise bandwidth to the minimum, as the final filter in a series of low-pass filters from Figure 4.5 we use single or double stage RC filters implemented on the PCB (Figures 4.9 4.10 4.12). Their schematics can be seen at A.2. Important filter parameters are the cutoff (single stage) or the corner (double stage) frequency f_c and the time constant τ. f_c determines the equivalent noise bandwidth while the time constant determines the settling time as 3τ. Regrading the experiment, this amount of time is necessary to wait between the voltage set point and the measurement point. At the single stage RC cutoff frequency $f_c = \frac{1}{2\pi RC}$ the output gets attenuated by 3 dB or $\sqrt{2}$ times. The double stage filter attenuation at $f_c = \frac{1}{2\pi\sqrt{R_1C_1R_2C_2}}$ is larger and for the identical filter stages as in Figure A.2 it is -6 dB or 2 times. To extract the 3 dB cutoff frequency of the two stage RC filter, one can use an online calculator [2]. The time constant of the single stage filter is $\tau = RC$ while for the two stage one it is $\tau = R_1C_1 + R_2C_2 + R_2C_1$. At Figure A.3a the normalized amplitude versus the frequency response of both filters can be seen. For the same R and C values the two stage filter has two times steeper slope after the cutoff resulting in the narrower noise equivalent bandwidth, reducing thus the noise on its output. But, its transient response is also slower and in the example in Figure A.3b its τ is three times larger than the τ of the single stage one.

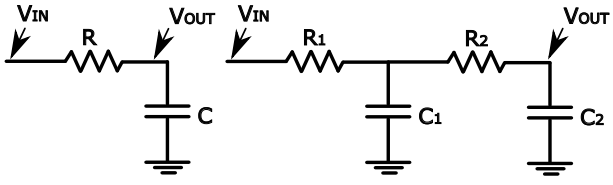


Figure A.2: **RC filter schematic.** The schematic of a single stage RC filter is shown on the left, while the schematic of a double stage one is shown on the right.

[2] http://sim.okawa-denshi.jp/en/CRCRkeisan.htm

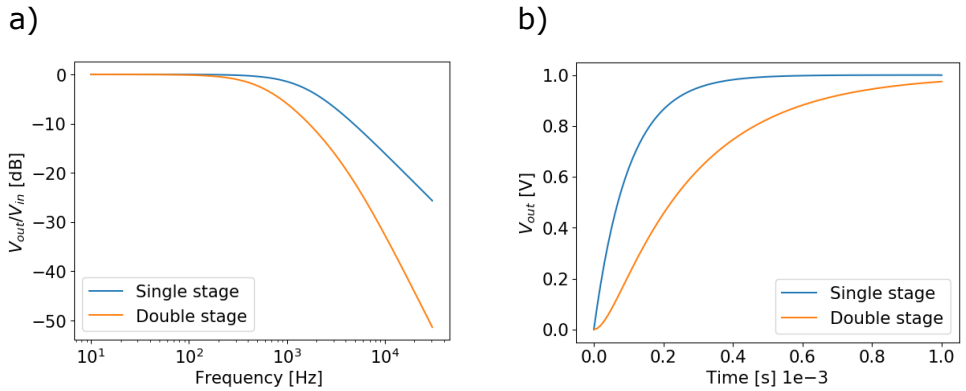


Figure A.3: **Simulation of the single (blue) and the double stage (orange) RC filters.** Such a filter is used on Iron Kid shown at Figure 4.12 and on Shrek shown at Figure 4.9, respectively. For both filters R=10 kΩ and C=10 nF is set. The normalized amplitude vs the frequency response, with 3 dB cutoff at 1.6 kHz for the single stage filter and 580 Hz for the double stage filter is shown in **a**. Transient response of the filter output to the 1 V step on the filter input is shown in **b**. The characteristic time needed for the V_{out} to reach 63% of the V_{in} is called time constant and it is 100 μs for the single stage and 300 μs for the double stage filter.

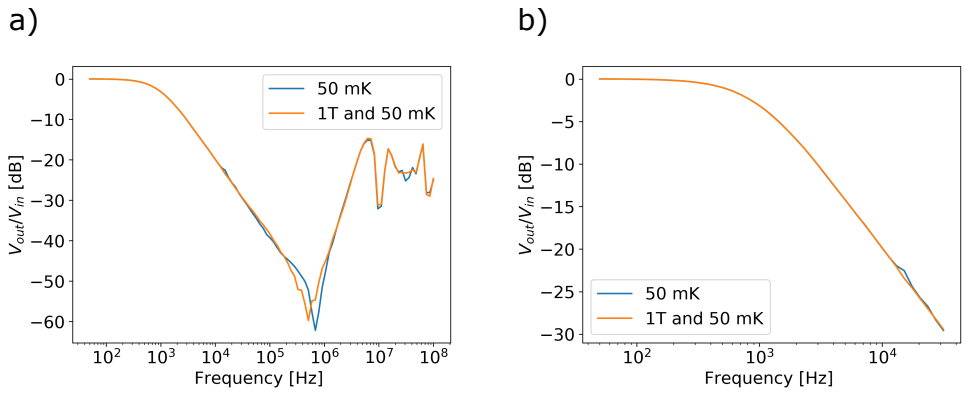


Figure A.4: **Plot showing the measured normalized amplitude versus the frequency response of the single stage RC filter.** Filter components are R=10 kΩ (MMU01020C1002FB300) and C=10 nF (C0805X103J5GACAUTO) as used on the Iron Kid PCB shown in Figure 4.12. The full amplitude vs frequency response, until 100 MHz, is shown in **a**, while **b** shows the zoom in until 30 kHz. The filter was mounted on another PCB. It was measured at the fridge base temperature with and without a magnetic field, using the UHFLI. The magnetic field was applied perpendicular to the PCB plane.

We also measured a few different RC filter configurations at the fridge base temperature. Figure A.4 shows the measured normalized amplitude versus the frequency

response of the commonly used filter. The good message is that the filter performs as expected also at 50 mK and under 1 T of magnetic field, at least until 1 MHz. At Figure A.4a it can be seen that the RC filter losses its filtering behaviour already at $f_t \approx 1\,MHz$. Since the lowest f_c of other filters in the probe filter chain, is 80 MHz, this results in an elevated noise transmission in the band from 1 to 80 MHz. A possible solution of this problem is to insert an additional RC filters, with $f_c < 1\,MHz$ below the LC filters in the probe. In Figure A.4b can be seen that f_c is slightly lower in comparison to the simulated case shown in Figure A.3a, but this is negligible.

A.1.3 Bias tee

A bias tee merges a DC voltage with a HF signal by behaving as a low-pass filter from the DC side and as a high pass filter from the HF side. Both a basic bias tee schematic and the real one used on our PCBs can be seen in Figure A.5. An important bias tee parameter is its RC constant τ, which for the basic case equals to $\tau = RC$. From the HF input we want it to be as long as possible, to minimize the voltage pulse distortion. For example, in order to pass a square voltage pulse with 1 ms duration, without distortion, an RC constant of at least 10 ms is required. To achieve a large τ, as can be seen in Table A.1, for fast gate bias tee we used large resistances. In spite of the large bias tee resistance, the applied DC voltage is still fully present at the gate electrode due to an infinite DC resistance of the gate electrode. Another requirement for bias tee, regarding the fast gates, is a good transmission for the spin control GHz frequencies, as well. Regarding the reflectometry, it does not require long pulses therefore the corresponding τ can be shorter. From the DC input, shorter τ increases the measurement speed, similar as in the RC filter case. An example of both the reflectometry and the fast gate bias tee can be seen in Figure 4.10.

Due to an unknown electrical representation of the filters and the value Z_p in Figure A.5 the real bias tee schematic gets complicated. The experiments in Figure A.6, however, indicate the proper functionality of the used bias tee. The fact that the upper scans

contain two identical, not distorted triangles, indicates that the bias tee passes the 2 μs long pulse, without distortion. Additionally, measurements on another sample indicated that a pulse with a 100 μs duration was not distorted as well. The smeared left triangle, on the lower measurement, indicates that the GHz wave is passing as well through the bias tee.

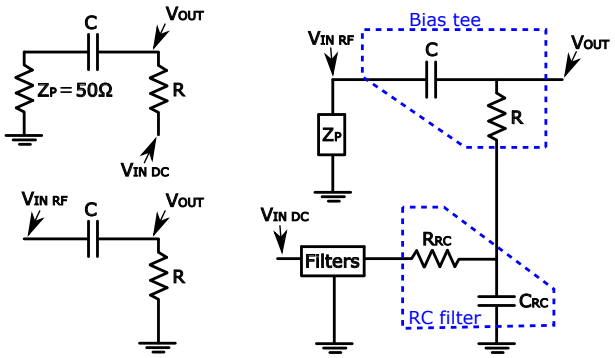


Figure A.5: **Bias tee schematic.** A simple bias tee schematic is shown on the **left**. The **top left** schematic shows that it behaves as a low-pass filter for the DC input and the **bottom left** schematic that it represents a high pass for the HF input. Schematic of the real bias tee circuit on the PCB is shown on the **right**. The output of the RC filter is connected to the bias tee DC input, altering thus the circuit topology and the bias tee parameters. Also, the electrical representation of the low-pass filters is not exactly known which complicates the real bias tee schematic even more. Z_p is the impedance of the instrument port the fast gate is connected to. It is typically 50 Ω, but other values are possible as well.

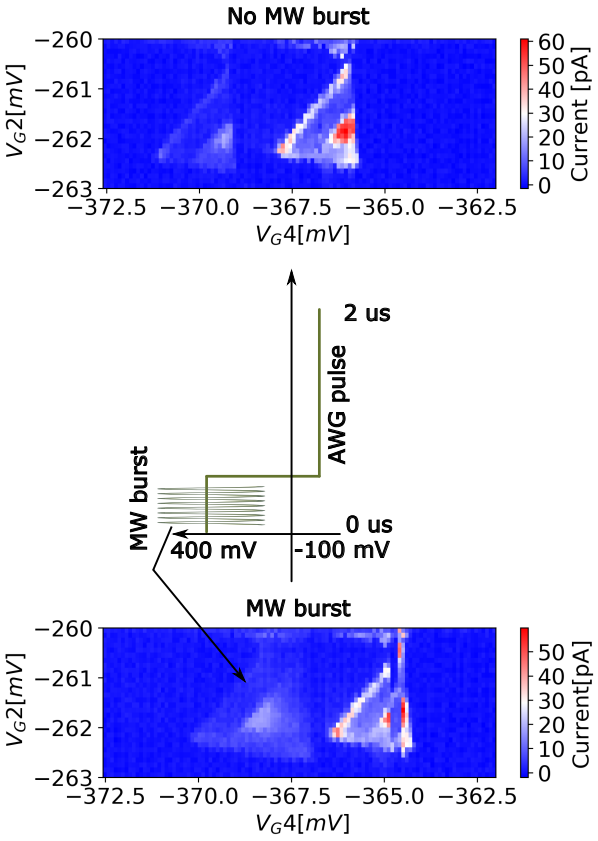


Figure A.6: **Confirmation of the proper bias tee functionality.** Zoom-in to the stability diagram of a DQD device. The measurements are performed in the Grandpa Rudolph fridge, at base temperature, with the DQD device bonded to an Iron Man PCB with the fast gate bias tee elements R=1.8 MΩ and C=10 nF. An AWG pulse, with the amplitude, on the AWG output, stated in the figure, was applied continuously during the measurement, but only one period is shown here. Since the bias tee, due to the capacitor connected in series, blocks the DC component of the signal at the HF input, heating up of the fridge takes place, in case of a non-zero DC component of the signal. Thus, the mean value was set to zero here, not to warm up the fridge. Due to the applied pulse at the gate 4, the triangle split in both (up and down) scans. The left triangle is fainter because the corresponding part of the pulse was shorter. On the lower scan, the left triangle also smears, due to applied MW burst of 5 GHz, with a power of 2 dBm at the VSG output.

PCB name	PCB number	RC filter	Fast gate bias tee	Reflectometry bias tee	Decoupling resistors or coupling capacitors	Matching circuit
Shrek	not marked	R=10 kΩ (MMU01020C1002FB300), C=10 nF (C0805X103J5GACAUTO) $f_c \approx 1.6\,kHz$, $\tau = 100\,\mu s$				
Iron Man	PCB 2	R=1 kΩ (RR0816P-102-B-T5), C=10 nF $f_c \approx 16\,kHz$, τ = 10 μs	R=1.8 MΩ (MMU01020C1804FB300), C=10 nF τ = 18 μs	R=10 kΩ, C=10 nF τ = 100 μs	R=1 kΩ	06_R1: 390 nH, f_{res}=427 MHz, C_p=356 fF 12_R2: 560 nH, f_{res}=342 MHz, C_p=387 fF 18_R3: 820 nH, f_{res}=280 MHz, C_p=394 fF 24_R4: 1200 nH, f_{res}=224 MHz, C_p=421 fF
Iron Kid	PCB 2	R=10 kΩ, C=10 nF $f_c \approx 1.6\,kHz$, τ = 100 μs	R=1.8 MΩ, C=10 nF τ = 18 ms	R=510 kΩ (MMU01020C5103FB300), C=1.5 nF (C0805X152J5GACAUTO) τ =765 μs	C=10 nF	NbTiN planar inductors
Iron Kid	PCB 4	R=10 kΩ, C=220 nF (VJ0805Y224KCXAJ) $f_c \approx 70\,Hz$, τ = 2.2 μs	R=2 MΩ (MMU01020C2004FB300), C=10 nF τ = 20 ms	R=10 kΩ, C=10 nF τ = 100 μs	C=220 pF (C0805X221J1GACAUTO)	No inductors mounted
Iron Kid	PCB 5	R=10 kΩ, C=220 nF $f_c \approx 70\,Hz$, τ = 2.2 μs	R=2 MΩ, C=10 nF τ = 20 ms	R=10 kΩ, C=10 nF τ = 100 μs	C=220 fF	06_R1: 390 nH, f_{res}=404 MHz, C_p=398 fF 12_R2: 560 nH, f_{res}=324 MHz, C_p=431 fF 18_R3: 820 nH, f_{res}=267 MHz, C_p=433 fF 24_R4: 1200 nH, f_{res}=229 MHz, C_p=403 fF

Table A.1: **Values of PCB components mounted on PCBs discussed in this thesis.** The component values, f_c and τ given here are the room temperature values. The inductors are taken from the Coilcraft designer kit 994-C320.

A.2 Python code

A.2.1 Spin dynamics experiment simulation

The code below uses the QuTiP (Quantum Toolbox in Python) package in Python for simulating spin dynamics experiments and for the generation of Bloch sphere illustrations and state probability evolutions in the corresponding figures. The initial version, written by Daniel Jirovec, is adapted for the requirements of this thesis. How to install the QuTiP package in Python and the documentation of all of its functions, used below, can be found in the package documentation[3].

Rabi

```
1  from qutip import *
2  from scipy import *
3  import numpy as np
4  import matplotlib.pyplot as plt
5
6
7  # State evolution during the Rabi experiment
8  # Assumed is the case in which spin can be rotated around any vector, which direction and amplitude are set
9  # by the rotation frequencies in x,y and z directions
10
11 down = basis(2,1) # Initial state is the spin down state
12
13 # Creating the Bloch sphere and setting it's features to the wanted ones
14 b = Bloch()
15 b.figsize = [2,2]
16 b.view = [-40,30]
17
18 # A list of colors to cycle through for points and vectors such that rotation vector colors
19 # match the corresponding trajectory color
20 b.point_color = ['#647464ff','g','k','c']
21 b.vector_color = ['#647464ff','b','r','m']
22
23 b.point_marker = ['o']
24 b.frame_width = 0.5
25 b.frame_alpha = 0.12
26 b.sphere_alpha = 0.07
27 b.font_size = 15
28 b.vector_width = 2
29 b.point_size = [5,5,5,5]
30 b.clear()
31
```

[3] http://qutip.org/docs/latest/installation.html

```
# Setting the rotation frequency
f1x = 50e6 # Rotation frequency around x-axis, in Hz
f1y = 0  # Rotation frequency around y-axis, in Hz
f_det = 50e6 # Rotation frequency around z-axis due to detuing between Larmor and the reference frequency, in Hz
f_normal = 50e6 # Normalization frequency, in Hz
                # The rotation vector of such a frequency will appear as a unit vector on the Blochh sphere

time_xz = 5 # in ns, only integer values
tau_burst = np.arange(2,25,1) # A list of waiting times in nanoseconds


Z_comp_points = list()
for j,tb in enumerate(tau_burst):
    returned_stuff = Rab(f1x, f1y, f_det, b, down, tb, f_normal)
    z = returned_stuff[2]
    b.add_states(down) # Add the initial state to the Blochsphere
    b.save(name = 'Rab\ bloch_tburst%d.svg'%j, dirc='Rab')
    Z_comp_points.append(z) # Z-component values of the final state trajectory, for plotting later on



# Rab experiment (in RWA)
def Rab(f1x, f1y, f_det, blochsphere, state, tau_burst, f_normal= 50e6):
    '''
    Function for calculating the state evolution during the Rabi experiment and representing it on the Bloch sphere.
    The details of used functions can be find in the manual of the QuTiP package, available online.

    Inputs:
        f1x: float type
            The rotation frequency around x-axis
        f1y: float type
            The rotation frequency around y-axis
        f_det: float type
            The rotation frequency around z-axis due to detuning between Larmor and the reference frequency, in Hz
        blochsphere: qutip.bloch.Bloch type
            The Bloch sphere instance
        state: qutip.qobj.Qobj type
            The initial state
        tau_burst: int type
            Duration of the burst in nanoseconds
        f_normal: float type
            Normalization frequency
            Vector of this frequency will appear as the unit vector in the Bloch sphere
    '''

    t = np.linspace(0,1, tau_burst) # Full time array in nanoseconds

    # Switching to the radial frequency
    # Factor 1e-9 is because of nanoseconds
    w1x = 2*np.pi*f1x*1e-9
    w1y = 2*np.pi*f1y*1e-9
    w_det = 2*np.pi*f_det*1e-9
    w_normal = f_normal*2*np.pi*1e-9

    points = []
    blochsphere.clear()
    # Going through the time array and calculating the new state for every nanosecond
    for i in range(1,(len(t)+2)):
        # Getting the x, y and z components of a state
        ex = expect(sigmax(), state)
```

```
92          ey = expect(sigmay(), state)
93          ez = expect(sigmaz(), state)
94          points.append([ex,ey,ez]) # Storing this components as the state point coordinates
95
96          wx = w1x
97          wy = w1y
98          wz = w_det
99
100         if i == len(t)+1: # At the end of the burst
101             blochsphere.add_vectors([wx/w_normal,wy/w_normal,wz/w_normal]) # Adding the rotation vector
102             blochsphere.add_points(np.array(points).T) # Adding the points of the corresponding trajectory
103             blochsphere.add_states(state) # Add the final state to the BLoch sphere at the last passage through the loop
104
105
106         # The next state (after one nanosecod) is calculated as a multiplication of the corresponding rotation operator
107         # and the previous state
108         state = ((np.cos(wx/2)*np.eye(2)-1.0j*np.sin(wx/2)*sigmax())
109                     *(np.cos(wy/2)*np.eye(2)-1.0j*np.sin(wy/2)*sigmay())
110                     *(np.cos(wz/2)*np.eye(2)-1.0j*np.sin(wz/2)*sigmaz()))*state
111
112
113     return state, blochsphere, points[-1][2]
```

Two axis qubit manipulation

```
1   from qutip import *
2   from scipy import *
3   import numpy as np
4   import matplotlib.pyplot as plt
5   cd somwhere # This line will raise an error not to forget to position to a wanted output folder
6
7
8   # State evolution during the Two-axes experiment
9   # Assumed is the resonant case where the burst frequency matches the Larmor frequency, so the frame is static in RWA
10
11  down = basis(2,1) # Initial state is the spin down state
12
13  # Creating the Bloch sphere and setting it's features to the wanted ones
14  b = Bloch()
15  b.figsize = [2,2]
16  b.view = [-40,30]
17
18  # A list of colors to cycle through for points and vectors such that rotation vector colors
19  # match the corresponding trajectory color
20  b.point_color = ['y','r']
21  b.vector_color = ['y','r','g','b']
22
23  b.point_marker = ['o']
24  b.frame_width = 0.5
25  b.frame_alpha = 0.12
26  b.sphere_alpha = 0.07
27  b.font_size = 15
28  b.vector_width = 2
29  b.point_size = [5,5,5,5]
30  b.clear()
31  # Setting the rotation frequency
32  f1 = 50e6 # in Hz
33  f_normal = 50e6 # Normalization frequency
```

```
34                  # The rotation vector of such a frequency will appear as a unit vector on the Bloch hsphere
35
36  time_xy = 5 # in ns, only integer values
37  tau_wait = 10 # in ns, only integer values
38
39
40  phi_array = np.linspace(0,2*np.pi,17)
41  Z_comp_points = list()
42  for j,p in enumerate(phi_array):
43      returned_stuff = Two_axes(f1, b, down, time_xy, tau_wait, phi = p, f_normal = f_normal)
44      z = returned_stuff[2]
45      b.add_states(down) # Add the initial state to the Blochsphere
46      b.save(name = 'Two_axes2\ bloch_phi_%d.png'%j, dirc='Two_axes') # Save the bloch spehre illustration
47                                                                      # It can be saved in a different format by adding
48                                                                      # different extension. E.g. .svg would save it
49                                                                      # in the svg format
50      Z_comp_points.append(z) # Z-component values of the final state trajectory, for plotting later on
51
52
53
54
55  # Two axes qubit rotation experiment (in RWA)
56  def Two_axes(f1, blochsphere, state, time_xy, tau_wait, phi = 0, f_normal = 50e6):
57      '''
58      Function for calculating the state evolution during the Two axes qubit experiment and representing it on the Bloch sphere.
59      The details of used functions can be find in the manual of the QuTiP package, available online.
60
61      Inputs:
62          f1: float type
63              The roation frequency
64          blochsphere: qutip.bloch.Bloch type
65              The Bloch sphere instance
66          state: qutip.qobj.Qobj type
67              The initial state
68          time_xy: int type
69              Duration of both bursts in nanoseconds
70          tau_wait: int type
71              Duration of the waiting time in nanoseconds
72          phi: float type
73              Phase of the second burst in radians
74          f_normal: float type
75              Normalization frequency
76              Vector of this frequency will appear as the unit vector in the Bloch sphere
77      '''
78
79      t = np.linspace(0,1, (int(time_xy)+int(tau_wait)+int(time_xy))) # Full time array in nanoseconds
80      # Switching to the radial frequency
81      # Factor 1e-9 is because of nanoseconds
82      w1 = 2*np.pi*f1*1e-9
83      w_normal = f_normal*2*np.pi*1e-9
84
85      points = []
86      blochsphere.clear()
87      # Going through the time array and calculating the new state for every nanosecond
88      for i in range(1,(len(t)+2)):
89
90          # Getting the x, y and z components of a state
91          ex = expect(sigmax(), state)
92          ey = expect(sigmay(), state)
93          ez = expect(sigmaz(), state)
```

```
94          points.append([ex,ey,ez]) # Storing this components as the state point coordinates
95
96
97          # During the first burst the rotation is only along the x-axis
98          if i<=time_xy:
99              wx = w1
100             wy = 0
101             wz = 0
102             if i == time_xy: # At the end of the burst
103                 blochsphere.add_vectors([wx/w_normal,wy/w_normal,wz/w_normal]) # Adding the rotation vector
104                 blochsphere.add_points(np.array(points).T) # Adding the points of the corresponding trajectory
105
106         # During the waiting time there is no rotation
107         elif (i>time_xy and i<=(time_xy+tau_wait)):
108             wx = 0
109             wy = 0
110             wz = 0
111
112         # During the second burst the rotation axis is determined by the angle phi
113         elif i>(time_xy+tau_wait):
114             wx = np.cos(phi)*w1
115             wy = np.sin(phi)*w1
116             wz = 0
117             if i == len(t)+1:
118                 blochsphere.add_vectors([wx/w_normal,wy/w_normal,wz/w_normal]) # Adding the rotation vector
119                 # Adding the points of the corresponding trajectory
120                 blochsphere.add_points(np.array(points[((time_xy+tau_wait)+1):]).T)
121
122         if i == len(t)+1:
123             blochsphere.add_states(state) # Add the final state to the BLoch sphere at the last passage through the loop
124
125         # The next state (after one nanosecod) is calculated as the multiplication of the corresponding rotation operator
126         # and the previous state
127         state = ((np.cos(wx/2)*np.eye(2)-1.0j*np.sin(wx/2)*sigmax())
128                     *(np.cos(wy/2)*np.eye(2)-1.0j*np.sin(wy/2)*sigmay())
129                     *(np.cos(wz/2)*np.eye(2)-1.0j*np.sin(wz/2)*sigmaz()))*state
130
131
132
133
134
135     return state, blochsphere, points[-1][2]
```

Ramsey

```
1   from qutip import *
2   from scipy import *
3   import numpy as np
4   import matplotlib.pyplot as plt
5   cd somwhere # This line will raise an error not to forget to position to a wanted output folder
6
7
8   # State evolution during the Ramsey experiment
9   # Assumed is the case in which both bursts rotate the spin around the same axis in the x-z plane
10
11  down = basis(2,1) # Initial state is the spin down state
12
13  # Creating the Bloch sphere and setting it's features to the wanted ones
```

```
14  b = Bloch()
15  b.figsize = [2,2]
16  b.view = [-40,30]
17
18  # A list of colors to cycle through for points and vectors such that rotation vector colors
19  # match the corresponding trajectory color
20  b.point_color = ['y','r','y']
21  b.vector_color = ['y','r','y','g','b']
22
23  b.point_marker = ['o']
24  b.frame_width = 0.5
25  b.frame_alpha = 0.12
26  b.sphere_alpha = 0.07
27  b.font_size = 15
28  b.vector_width = 2
29  b.point_size = [5,5,5,5]
30  b.clear()
31
32  # Setting the rotation frequency
33  f1 = 50e6 # Rotation frequency around x-axis, in Hz
34  f_det = 50e6 # Rotation frequency around z-axis due to detuing between Larmor and the reference frequency, in Hz
35  f_normal = 50e6 # Normalization frequency, in Hz
36                  # The rotation vector of such a frequency will appear as a unit vector on the Blochh sphere
37
38  time_xz = 5 # in ns, only integer values
39  tau_wait = np.arange(6,30,2) # A list of waiting times in nanoseconds
40
41
42  Z_comp_points = list()
43  for j,tw in enumerate(tau_wait):
44      returned_stuff = Ramsey(f1, f_det, b, down, time_xz, tw, f_normal)
45      z = returned_stuff[2]
46      b.add_states(down) # Add the initial state to the Blochsphere
47      b.save(name = 'Ramsey2\ bloch_twait%d.png'%j, dirc='Ramsey')
48      Z_comp_points.append(z) # Z-component values of the final state trajectory, for plotting later on
49
50
51
52  # Ramsey experiment (in RWA)
53  def Ramsey(f1, f_det, blochsphere, state, time_xz, tau_wait, f_normal = 50e6):
54      '''
55      Function for calculating the state evolution during the Ramsey experiment and representing it on the Bloch sphere.
56      The details of used functions can be find in the manual of the QuTiP package, available online.
57
58      Inputs:
59          f1: float type
60              The rotation frequency around x-axis
61          f_det: float type
62              The rotation frequency around z-axis due to detuning between Larmor and the reference frequency, in Hz
63          blochsphere: qutip.bloch.Bloch type
64              The Bloch sphere instance
65          state: qutip.qobj.Qobj type
66              The initial state
67          time_xz: int type
68              Duration of both bursts in nanoseconds
69          tau_wait: int type
70              Duration of the waiting time in nanoseconds
71          f_normal: float type
72              Normalization frequency
73              Vector of this frequency will appear as the unit vector in the Bloch sphere
```

```
    '''

    t = np.linspace(0,1, (int(time_xz)+int(tau_wait)+int(time_xz))) # Full time array in nanoseconds

    # Switching to the radial frequency
    # Factor 1e-9 is because of nanoseconds
    w1 = 2*np.pi*f1*1e-9
    w_det = 2*np.pi*f_det*1e-9
    w_normal = f_normal*2*np.pi*1e-9

    points = []
    blochsphere.clear()
    # Going through the time array and calculating the new state for every nanosecond
    for i in range(1,(len(t)+2)):
        # Getting the x, y and z components of a state
        ex = expect(sigmax(), state)
        ey = expect(sigmay(), state)
        ez = expect(sigmaz(), state)
        points.append([ex,ey,ez]) # Storing this components as the state point coordinates

        # During the first burst the rotation vector is in the x-z plane
        if i<=time_xz:
            wx = w1
            wy = 0
            wz = w_det
            if i == time_xz: # At the end of the burst
                blochsphere.add_vectors([wx/w_normal,wy/w_normal,wz/w_normal]) # Adding the rotation vector
                blochsphere.add_points(np.array(points).T) # Adding the points of the corresponding trajectory


        # During the waiting time the rotation vector is along the z-axis
        elif (i>time_xz and i<=(time_xz+tau_wait)):
            wx = 0
            wy = 0
            wz = w_det
            if i == (time_xz+tau_wait):
                blochsphere.add_vectors([wx/w_normal,wy/w_normal,wz/w_normal]) # Adding the rotation vector
                blochsphere.add_points(np.array(points[(time_xz+1):]).T) # Adding the points of the corresponding trajectory

        # During the second burst the rotation vector is in the x-z plane
        elif i>(time_xz+tau_wait):
            wx = w1
            wy = 0
            wz = w_det
            if i == len(t)+1:
                blochsphere.add_vectors([wx/w_normal,wy/w_normal,wz/w_normal]) # Adding the rotation vector
                # Adding the points of the corresponding trajectory
                blochsphere.add_points(np.array(points[((time_xz+tau_wait)+1):]).T)

        if i == len(t)+1:
            blochsphere.add_states(state) # Add the final state to the BLoch sphere at the last passage through the loop


        # The next state (after one nanosecod) is calculated as a multiplication of the corresponding rotation operator
        # and the previous state
        state = ((np.cos(wx/2)*np.eye(2)-1.0j*np.sin(wx/2)*sigmax())
                    *(np.cos(wy/2)*np.eye(2)-1.0j*np.sin(wy/2)*sigmay())
                    *(np.cos(wz/2)*np.eye(2)-1.0j*np.sin(wz/2)*sigmaz()))*state


```

```
134
135         return state, blochsphere, points[-1][2]
```